MATERIALS BY DESIGN AND DETOUR: THE SEARCH FOR AN INTRINSIC AXION INSULATOR

by
Veronica Jane Stewart

A dissertation submitted to The Johns Hopkins University in conformity with the requirements for the degree of Doctor of Philosophy

Baltimore, Maryland
July, 2021

Abstract

Axion insulators are a new class of material, theoretically proposed but not yet physically realized. They have a topologically non-trivial electronic structure similar to that of a $\mathbb{Z}_2$ topological insulator (TI), but include magnetic ions and thus have broken time-reversal symmetry (TRS). Breaking TRS opens a gap in the conductive surface states, but permits observation of a large quantized magnetoelectric effect. This thesis describes efforts to discover an intrinsic axion insulator using a materials by design process.

The physical properties of an axion insulator place constraints on its structure and composition (for example, requiring magnetic ions and a $\mathbb{Z}_2$ symmetry). A database search was conducted to identify materials that satisfy these constraints. Candidate materials were evaluated by electronic structure calculations and for chemical suitability, and the most promising were synthesized and characterized. Although no axion insulator was ultimately found, several of the candidates displayed other exciting properties and were investigated in detail.

Chapter one introduces several of the concepts used in this work, including crystal structures, topological materials, and methods for synthesis and characterization. Chapter two discusses the overall search process and describes work on $MnBi_2Te_4$, $Y_2Ru_2O_7$, $EuMn_2P_2$, and other candidate materials. Chapter three covers Nd_2S_5Sn and Pr_2S_5Sn, two isostructural distorted honeycomb lattice materials with dramatically different magnetic properties. The Nd compound orders antiferromagnetically at $T_N \approx$ 2.5 K, and undergoes a series of quantum phase transitions under an applied magnetic

field, which a magnetic phase diagram was constructed to describe. The Pr analog has no magnetic order down to $T = 0.41$ K, inviting comparison to magnetically frustrated quantum spin liquid candidates. Chapter four presents work on $Nb_4Se_4I_4$. This breathing pyrochlore was found to possess a hidden order transition, clearly visible in heat capacity but absent in magnetic and structural characterization. On the basis of thermodynamic, magnetic, structural, computational, and spectroscopic characterization, it is proposed that the observed heat capacity anomaly is due to local distortions of the Nb_4 tetrahedra.

Dissertation Committee

Dr. Tyrel M. McQueen (Primary Advisor)
Professor
Department of Chemistry
Department of Physics and Astronomy
Department of Materials Science and Engineering
Krieger School of Arts and Sciences
The Johns Hopkins University

Dr. Thomas J. Kempa
Assistant Professor
Department of Chemistry
Krieger School of Arts and Sciences
The Johns Hopkins University

Dr. V. Sara Thoi
Assistant Professor
Department of Chemistry
Krieger School of Arts and Sciences
The Johns Hopkins University

To Maggie

Acknowledgements

This thesis depended on the help of many people, most of all on the guidance of my advisor Prof. Tyrel McQueen. I am grateful for his unwavering patience, depth of knowledge, and enthusiasm, and for how much I have learned from him about materials chemistry and the scientific process. I thank him also for his support and advocacy for students during difficult times. I also thank my committee, Profs. Thomas Kempa and Sara Thoi, for their support, and Prof. Thoi additionally for her warm welcome to JHU and her mentorship during my first years here.

The current and former members of the McQueen lab have been a fantastic group of people to work and spend the days with. Kathryn Arpino, Lennox Morey, Zachary Kelly, Jessica Panella, Thao Tran, Cheng Wan, Hongcheng Lu, Michał Winiarski, and Adam Phelan answered endless questions during my first years in lab. I have learned so much from them, and I'm grateful for their kindness and patience. Lisa Pogue, Chris Pasco, Mekhola Sinha, Juan Chamorro, Hector Vivanco, Lucas Pressley, Tanya Berry, Nicholas Ng, Shannon Bernier, Evan Crites, Johndavid Sabedra, Austin Ferrenti, Peter Orban, and Zubia Hasan have shared their time and knowledge in countless ways, and have made the day-to-day efforts of research that much better. I especially want to thank Lennox, whose mentorship and friendship has had a tremendous influence on my life, and Mekhola, who has been an officemate, collaborator, and co-conspirator for the past five years.

Too many other members of the chemistry and physics communities at JHU to list have helped in many ways, including Avery Baumann, Rishi Bhandia, Alireza

Ghazemi, Tom Halloran, Chana Honick, Yufan Li, Chris Lygoras, Fahad Mahmood, Vincent Morano, Tim Reeder, and Yuanyuan Xu; Profs. Peter Armitage, Collin Brohom, and Natalia Drichko; and the department staff who keep everything running, including Marianne Fahmy, Jasmine Harris, Smaa Koryam, Brian Schriver, Maxime Siegler, Nicolette Stachowiak, and Boris Steinberg. I would also like to thank Ethan Cottrill and Prof. Susanna Thon.

Friends, housemates, and even some family in Baltimore who have kept me grounded and sane during my time here include Christopher Kauffman, Ian Moltrup, Lauren Fanney, Nate Palmer, Ada Link, Charles Whittington, Krys Peles, Jennifer Bissell, and Ethan Greenblatt. (And of course Milli, Kaiju, Chigger, Zhushka, Cashew, Piper, and Tiny). I also owe a great deal of happiness to Michaela Voorhees, Hannah Schaupp, Tom Chung, and Patience Dodgeson for years for friendship lasting across thousands of miles, and of course to Erin Sheffels, the eternal roommate of my heart.

I don't know how to express my gratitude to my parents and family for everything they've done. Thank you for your unwavering support, even when my choices took me far away. Finally, thank you to Daniel, who has been an incredible source of love and stability these past five years. I'm grateful every day for his kindness, generosity, intelligence, and humor.

Contents

List of Tables

List of Figures

Chapter 1

Introduction

With nearly the whole periodic table available to work with, the scope of potential inorganic materials can seem overwhelming. Identifying and synthesizing new useful materials requires choosing from thousands of possible chemical compositions and crystal structures to investigate. Although this complexity makes materials discovery challenging, by navigating it we can find fascinating and technologically revolutionary materials properties.

One approach to bring order to this chaos is the concept of “materials by design" (Figure 1-1). In this strategy, the starting point is not a particular group of elements or crystal structure, but some need that must be met. The properties that a material must have to meet this need are identified, and candidates that may have these properties are synthesized. Once these candidates are characterized, we can better understand the underlying behavior, refine our model for what can cause the desired properties, and select new materials candidates to repeat the cycle with. Equally important are the outcomes that may occur during this process: the discovery of unusual phenomena, the improvement of synthetic methods, and the construction of useful devices.

This approach is particularly useful for quantum materials - a broad category that includes any material whose properties cannot be fully explained by classical physics,

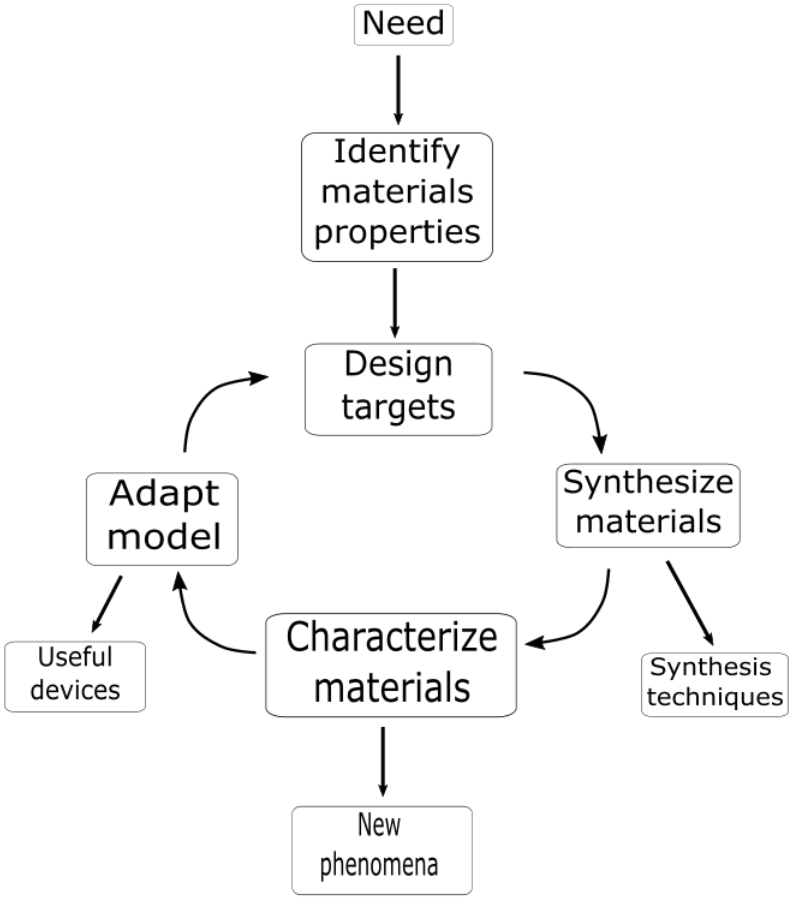

Figure 1-1. A schematic of the "materials by design" strategy for the discovery of new materials [1].

but must be described using a quantum model. Under this umbrella are materials such as superconductors, topological materials, and quantum spin liquids, all of which are exciting for their potential technological applications as well as their exotic physics. As our understanding of these materials is still being developed, the materials by design model for identifying and studying them is particularly useful.

This work centers around applying a materials by design process to a sought after category of topological materials called axion insulators. Materials candidates were identified based on the principles of these theoretical materials. Although no axion insulator was ultimately discovered, several of the materials investigated during this search proved to have other interesting properties. Chapter two describes the search processes employed and the full set of candidates studied, while chapters three and four report in-depth analysis of two materials of interest. Chapter three covers niobium selenium iodide, which displays an unusual and subtle phase transition. Chapter four reports work on Nd_2S_5Sn and Pr_2S_5Sn, two materials containing an approximate honeycomb lattice which have extremely different magnetic properties despite being isostructural.

The remainder of this chapter will give a brief introduction to several important background topics: 1) the physical and electronic structure of crystals, 2) the physics of topological insulators, which axion insulators are a subclass of, 3) magnetism in crystalline materials, and 4) the synthetic and characterization techniques used in this research.

1.1 Materials structure and symmetry

The materials discussed here will all be crystalline, meaning they have a periodically repeating structure. In crystalline materials, some set of atoms is tessellated through space, resulting in a material where the same basic unit is repeated over and over. If

we think of that unit as a point, ignoring its contents for now, the crystal as a whole can be described as a lattice of repeating points, separated by the dimensions of the basic unit and arranged according to some symmetry [2]. This concept is known as a Bravais lattice, and it can be defined as a set of such points

$$\mathbf{R} = n_1\mathbf{a}_1 + n_2\mathbf{a}_2 + n_3\mathbf{a}_3 \tag{1.1}$$

$\mathbf{a}_1$, $\mathbf{a}_2$, and $\mathbf{a}_3$ are known as the primitive lattice vectors, and n_1, n_2, n_3 are integers. The vectors $\mathbf{a}_1$, $\mathbf{a}_2$, and $\mathbf{a}_3$ are chosen so that any point in the lattice can be reached by some linear combination of the three, i.e. by moving some integer number of steps along the three vectors. In three dimensions, this requires that they not all lie in the same plane. These primitive vectors define the translational symmetry of the lattice. Two points that can be connected by primitive vectors must be equivalent, and we can place the origin of the primitive vectors at any point and still be able to generate the entire lattice.

There are many possible choices of primitive vectors for any particular lattice, all of which are symmetrically equivalent. In two dimensions, there are five unique Bravais lattices: oblique, rectangular, centered rectangular, square, or hexagonal (Figure 1-2). These can be grouped into lattice systems. In 2D, rectangular and centered rectangular belong to the same system, while the other three lattices each have their own. In three dimensions, there are fourteen Bravais lattices, which are grouped into seven lattice systems; each system has 1 - 4 distinct lattices. As in 2D, each 3D Bravais lattice is defined by the relative distances and angles between points and by its centering. The seven 3D lattice systems are triclinic, monoclinic, orthorhombic, tetragonal, rhombohedral, hexagonal, and cubic.

Along with its Bravais lattice, the symmetry of a crystal is described by its point group. This is a set of symmetry operations where at least one point is

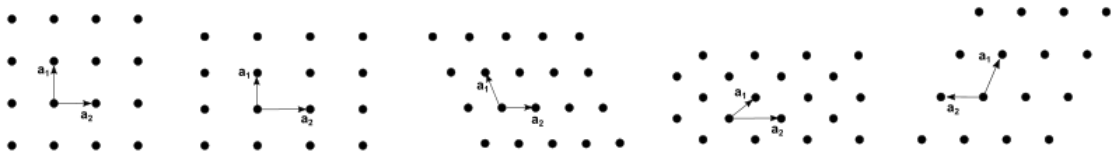

Figure 1-2. The five two-dimension Bravais lattices. From left to right: square, rectangular, oblique, centered rectangular, hexagonal.

fixed in place, which includes rotations, reflections, and inversions, but excludes translational symmetries. There are 32 point groups in 3D, which are sorted into seven crystal systems. In five of these crystal systems - triclinic, monoclinic, orthorhombic, tetragonal, and cubic - there is a one-to-one correspondence between crystal system and lattice system, and each point group is associated with only one lattice. However, the other two crystal systems, trigonal and hexagonal, do not line up one-to-one with the rhombohedral and hexagonal lattice systems, and care should be taken when discussing them. For convenience, all the combinations in these systems can be described as one hexagonal crystal family.

Finally, each crystal can be assigned one of 230 space groups. A space group contains the symmetry elements of a particular point group / Bravais lattice combination and potentially two additional symmetry elements involving both point and translational symmetry operations: glide planes and screw axes [3].

The repeating section of the crystal, represented by a lattice point, is known as the unit cell. Any section of a crystal that repeats according to a Bravais lattice can be used as a unit cell, but it is often useful to choose one that possesses the full symmetry (all point group operations) of the lattice. One option is a conventional cell, which is simply the smallest cell possible with its edges along the symmetry directions of the lattice. Conventional cells are a relatively intuitive way to visualize the structure of

a crystal, and their dimensions are often reported as the crystal's lattice constants. Another choice is the Wigner-Seitz primitive cell. To form a Wigner-Seitz cell, we can choose one point in the lattice, and then take the region of space closer to that point than to any other. The resulting cell, like the conventional cell, will have the full symmetry of the lattice and will completely fill space when translated along the lattice vectors. Wigner-Seitz cells are used to compute the electronic energy levels of a crystal, known as its band structure.

Understanding extended solids requires an extension of the concepts of molecular chemistry. In a single atom, the quantized energy levels available to the electrons are described in terms of orbitals. When bonding occurs, we can talk about molecular orbitals, where the wavefunctions of the contributing orbitals are combined into a new set of energy levels shared by all atoms involved. This is mathematically accomplished by a linear combination of the atomic wavefunctions, and requires that the number of molecular orbitals be equal to the number of atomic orbitals in the basis. In extended solids, this number is extremely large, so the gap between energy levels becomes negligibly small, resulting in a continuous band of energies. The electronic properties of the material can then be discussed in terms of these bands.

There are two major approaches to understanding the formation of bands. One is to consider them as a combination of many atomic orbitals, as stated above (the tight-binding model). Alternatively, we can start with the wavefunction of a free electron and then modify it by confining it to a periodic lattice. In reality, the behavior of electrons in a solid is somewhere in between these two approaches, neither fully localized in atomic orbitals nor fully delocalized as waves minimally affected by the atoms. However, most materials are more easily described by one model or the other, with the electronic levels in insulators more atomic-orbital-like and those in metals more free-electron-like. For simplicity, we will begin with the latter approach, known as the nearly free electron model, and then return to the tight-binding model using

atomic orbitals.

To adapt the wavefunction of a free electron to a periodic lattice, we need to ensure that it has the same translational symmetry as the lattice. Because each unit cell has the same arrangement of atoms, it must also have the same band structure, so the wavefunction of each state must be the same in every cell. Bloch's theorem establishes that this translational symmetry can be applied by writing the wavefunction $\psi_{\mathbf{k}}(\mathbf{r})$ as a free electron plane wave combined with a function having the periodicity of the lattice[1]:

$$\psi_{\mathbf{k}}(\mathbf{r}) = e^{i\mathbf{k}\cdot\mathbf{r}} u_{\mathbf{k}}(\mathbf{r}) \tag{1.2}$$

$e^{i\mathbf{k}\cdot\mathbf{r}}$ is the wavefunction of a free electron at position $\mathbf{r}$ with wavevector $\mathbf{k}$.i is the unit imaginary number. $u_{\mathbf{k}}(\mathbf{r})$ is a periodic function which must fulfill $u(\mathbf{r}+\mathbf{R}) = u(\mathbf{r})$, where $\mathbf{R}$ is a lattice point. Although not exactly a quantum number, $\mathbf{k}$ behaves as one in many ways, indexing the wavefunction and affecting electronic properties. The magnitude of $\mathbf{k}$ is the angular wavenumber, $\frac{2\pi}{\lambda}$, and the direction of the vector $\mathbf{k}$ is the direction of propagation. So, $\hbar\mathbf{k}$ is analogous to the momentum of the electron (although it is not conserved in all cases that a true momentum is). Because it is a vector, we can write $\mathbf{k}$ as a linear combination of three other vectors $\mathbf{b}_i$ (i = 1, 2, 3):

$$\mathbf{k} = k_1\mathbf{b}_1 + k_2\mathbf{b}_2 + k_3\mathbf{b}_3 \tag{1.3}$$

Bloch's theorem 1.2 can also be written as

$$\psi_{\mathbf{k}}(\mathbf{r}+\mathbf{R}) = e^{i\mathbf{k}\cdot\mathbf{R}}\psi_{\mathbf{k}}(\mathbf{r}) \tag{1.4}$$

In order for the wavefunction to be periodic $(\psi_{\mathbf{k}}(\mathbf{r}+\mathbf{R})) = \psi_{\mathbf{k}}(\mathbf{r})$, we must have

[1]Proofs and further discussion of Bloch's theorem are available in sources [2, 4–6].

$$e^{i\mathbf{k}\cdot\mathbf{R}} = 1 \tag{1.5}$$

Then by using the definition of the Bravais lattice (1.1),

$$e^{in_i\mathbf{k}_i\cdot\mathbf{a}_i}\psi_{n\mathbf{k}}(\mathbf{r}) = 1 \tag{1.6}$$

Now we need to find the values of $\mathbf{k}$ that satisfy this condition. We previously wrote out $\mathbf{k}$ in terms of three (so far unknown) component vectors $\mathbf{b}_i$ (1.3). Substituting this in to 1.8,

$$e^{i(k_1\mathbf{b}_1+k_2\mathbf{b}_2+k_3\mathbf{b}_3)\cdot(n_1\mathbf{a}_1+n_2\mathbf{a}_2+n_3\mathbf{a}_3)}\psi_{\mathbf{k}}(\mathbf{r}) = 1 \tag{1.7}$$

The exponential can be multiplied out into nine terms, each with the form $e^{ik_i\mathbf{b}_i\cdot n_j\mathbf{a}_j}$. In each term, the exponent must be zero or some other multiple of 2π for the term to equal one. To satisfy this condition, we can choose the vectors $\mathbf{b}_i$ so that $\mathbf{b}_i\cdot\mathbf{a}_j = 2\pi\delta_{ij}$, meaning that $\mathbf{b}_i\cdot\mathbf{a}_j = 2\pi$ when $i = j$, and 0 when $i \neq j$. Additionally, the k_i must be integers to keep the terms equal to 1.

We can now see that the set of wavevectors $\mathbf{k}$ form a Bravais lattice, with basis vectors $\mathbf{b}_i$. Because they are three different directional components of $\mathbf{k}$, and because they are each orthogonal to a different pair of $\mathbf{a}_i$ vectors, they must be linearly independent and not all lie in the same plane. Since this is true and all k_i are integers, the definition of a Bravais lattice is satisfied. The allowed $\mathbf{k}$ values must form a lattice of points which can all be reached from any other by a linear combination of $\mathbf{b}_i$.

This lattice of $\mathbf{k}$ wavevectors is known as the reciprocal lattice. Instead of being in real space, it is described as a set of points in "momentum space", "reciprocal space", or "k-space". The reciprocal lattice basis vectors can be computed for any specific lattice from the primitive vectors $\mathbf{a}_i$[2]. The concept of the reciprocal lattice is frequently used

[2] $\mathbf{b}_1 = 2\pi\frac{\mathbf{a}_2\times\mathbf{a}_3}{\mathbf{a}_1\cdot(\mathbf{a}_2\times\mathbf{a}_3)}$ and the expressions for the other two vectors are similar

Figure 1-3. A real-space 2D Bravais lattice with a Wigner Seitz unit cell outlined in blue, and its corresponding reciprocal-space lattice with a Brillouin zone outlined.

in crystallography, as it is very useful for the description of light or particles diffracting off a lattice. Because it is a Bravais lattice, we can choose a single repeating cell in k-space to examine, since the wavefunctions will repeat periodically. Typically, this is done by taking the reciprocal of the real-space Wigner-Seitz cell. The resulting section of k-space is known as the first Brillouin zone (Figure 1-3).

At each $\mathbf{k}$ in the Brillouin zone, there is a different set of wavefunctions (electronic states). Each state at a particular $\mathbf{k}$ is additionally described by the integer index n. Now that we have the set of allowed Bloch wavefunctions in the lattice, we can use the Schrödinger equation to determine their energies, ϵ_k, which are the eigenvalues of this equation. The eigenvalues, like the wavefunctions, must have the periodicity of the lattice so that $\epsilon_{\mathbf{k}} = \epsilon_{\mathbf{k}+\mathbf{k}}$, and be indexed by a particular $\mathbf{k}$ and n. By computing all $\epsilon_{n\mathbf{k}}$ in one Brillouin zone, we can get a full picture of the electronic levels of the crystal.

These levels are typically visualized in a band structure plot. For a one dimensional structure, we can simply plot energy versus k along a single axis, producing a series of bands stacked from low to high n. In three dimensional materials however, there are three components of $\mathbf{k}$, and the Brillouin zone is a three dimensional object, making a graphic visualization more difficult. These band structures are typically plotted by choosing certain high symmetry points in the Brillouin zone, and plotting along lines in k-space between these points (Figure 1-4). The set of symmetry points used

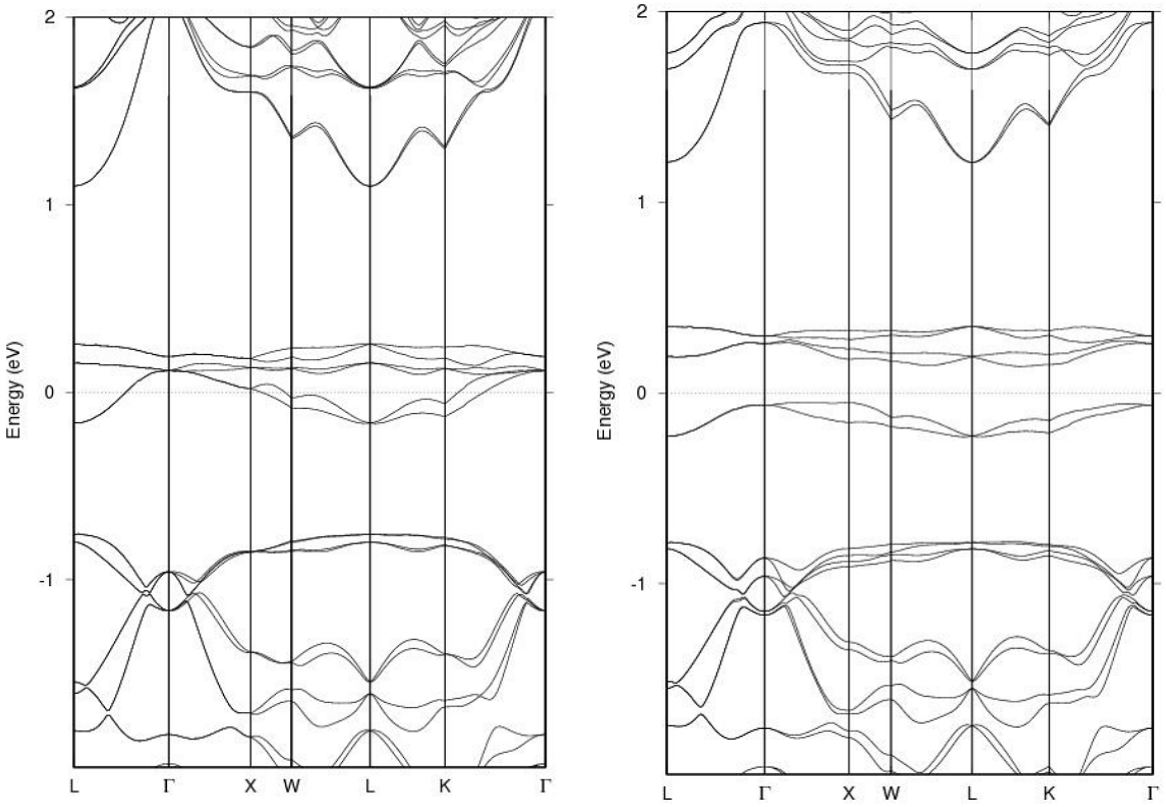

Figure 1-4. Examples of metallic (left) and insulating (right) band structures. In a metal, the Fermi energy lies within a partially filled band, and in an insulator it lies in a gap between bands. Both structures are for the material $Nb_4Se_4I_4$. The computed band structure transitions from a metal to an insulator when stronger electron correlations are included. In three-dimensional band structures like these, the letters on the bottom axis (the momentum $\mathbf{k}$) correspond to high-symmetry $\mathbf{k}$-points in the Brillouin zone, and the energies states between these points are plotted as bands.

depends on the specific Bravais lattice.

The number of electrons filling the bands is also important. Electrons are added to the bands by filling from lower to higher energy states. By the Pauli exclusion principle, each state in a band can take at most two electrons. If all occupied bands are completely filled (possible only when the number of electrons per unit cell is even), then the material is an insulator (Figure 1-4(b)). The distance between the highest filled band and the lowest empty band is called the band gap, and the energy halfway between these two bands is called the Fermi level, E_F. Conversely, if a band is partially

filled, the material will be conductive, with its electrons able to move easily through the half-filled band. In metallic materials the Fermi level lies in the middle of a band, at the highest energy that would be occupied at 0 K 1-4(a).

The remainder of this section will cover methods to determine the band energies. One approach is to continue with the nearly free electron model. Starting with the Bloch wavefunctions $\psi_{n\mathbf{k}}(\mathbf{r}) = e^{i\mathbf{k}\cdot\mathbf{r}}u_{n\mathbf{k}}(\mathbf{r})$, we assume that the periodic potential of the lattice is weak, much smaller than the difference between any two unperturbed energy states ϵ_k^0. Applying the perturbation causes the bands to repel each other, raising the energy of a band for each ϵ_k^0 level that lies below it, and lowering the energy for each level above it. However, the shift in energies is only significant if two bands are nearly degenerate, within the gap between them on the order of U. This only occurs when the wavevector $\mathbf{k}$ is close to a plane in the reciprocal lattice. If $\mathbf{k}$ lies on the plane, the change in energy will just be the potential at that point, $\mathrm{U}_{\mathbf{k}}$; one energy level will be raised by this amount, and the other will be lowered, thus breaking the degeneracy. States lying near but not on the plane will repel by a smaller amount, while away from the plane the bands will keep their parabolic free electron shape.

If instead of primarily delocalized electrons we have an insulator with electrons mainly localized at the atoms, we can instead use the tight-binding method, in which the description of the bands is based on atomic wavefunctions rather than on plane waves. Tight-binding wavefunctions that satisfy the Bloch condition can be constructed with the form

$$\psi(\mathbf{r}) = \sum_{\mathbf{R}} e^{i\mathbf{k}\cdot\mathbf{R}}\phi(\mathbf{r}-\mathbf{R}) \tag{1.8}$$

where the $\phi(\mathbf{r})$ are linear combinations of the atomic wavefunctions $\psi_n(\mathbf{r})$ using coefficients b_n:

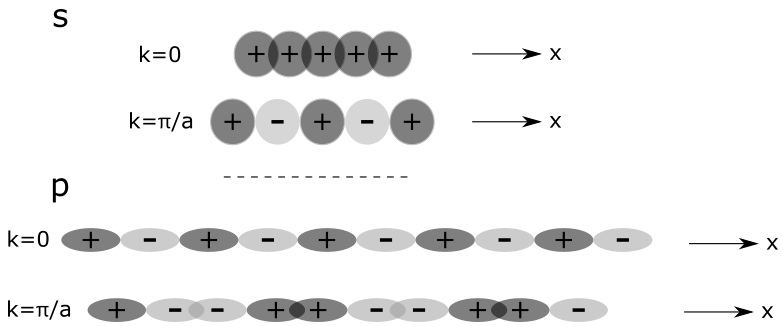

Figure 1-5. A cartoon of tight-binding orbitals for a one-dimensional chain. A band composed of s-orbitals will run from the lowest-energy fully bonding state at k = 0 to the highest-energy fully antibonding state at k = π/a. A band of p orbitals will run in the opposite direction, with the highest energy at k = 0, because of the different symmetry of the orbitals that combine to form each state.

$$\phi(\mathbf{r}) = \sum_n b_n \psi_n(\mathbf{r}) \tag{1.9}$$

The tight binding method allows a more chemically intuitive visualization of bands as overlapping atomic orbitals [7]. If we picture a one-dimensional chain of s orbitals, each on one lattice site, the lowest energy state will be one where all orbitals have the same sign, and the highest the one where their signs are alternating, which can be thought of respectively as the fully bonding and fully antibonding states. The equations for the linear combination of orbitals are consistent with this intuition (Figure 1-5). At $k = 0$, $\psi_k = \Sigma e^0 \chi_n = \Sigma \chi_n$, so all the contributing s orbitals have the same sign. At $k = \pi$/a, $\psi_k = \Sigma e^{in\pi} \chi_n = \Sigma(-1)^n$, so the signs are positive at even n and negative at odd n, giving the expected antibonding state. There is also a state at each allowed k over the range between these two extremes, giving a band whose energy increases with k.

The shape and orientation of the bands depends on the orbitals used and the degree of overlap. If the s-orbitals in our 1D chain are replaced with p-orbitals aligned head-on, at $k = 0$ the negative and positive lobes of the orbitals will overlap, creating the fully antibonding state, and the fully bonding state will be at $k = \pi$/a. The width of the band, also called the dispersion, is determined by the orbital overlap. A smaller

unit cell will lead to more orbital overlap and widen the bands, demonstrating a direct connection between chemical structure and electronic properties.

Band structures are further complicated by interactions between bands that lie close in energy, and by spin-orbit coupling (SOC). In spin-orbit coupling, the spin magnetic moment of the electron interacts with the orbital potential, breaking degeneracy between states and splitting the bands (as would also happen if an external magnetic field were applied). Spin-orbit coupling is strongest in heavy elements, and can have a major effect on band energies and material properties.

Although neither the nearly free electron model nor the tight binding model is a perfect description of an electronic band structure, they are useful as simplified descriptions. Both make an approximation that the electronic wavefunctions are all independent, removing the many electron-electron interaction terms in the full multi-electron Schrödinger equation and instead using the perturbation to the full plane wave or atomic orbitals to partially account for the interactions. Although truly solving the Schrödinger equation with all interaction terms is computationally unfeasible, many techniques have been developed to improve the necessary approximations and calculate band energies. Several of these techniques will be discussed here, with a focus on density functional theory, which was used extensively for the work described in later chapters.

One common procedure is the self-consistent field technique (also known as the Hartree-Fock method) [8, 2]. The wavefunctions are computed using an initial guess for the perturbing potential $U(\mathbf{r})$. The obtained wavefunctions are then used to compute a new $U(\mathbf{r})$. If the result differs from the starting guess, the procedure is repeated until the output $U(\mathbf{r})$ is the same as the input. At this point, the calculation has obtained self-consistency, and the obtained $U(\mathbf{r})$ and wavefunctions are used to compute the desired properties. The reliability of this technique depends strongly on the initial choice of $U(\mathbf{r})$.

Early attempts at band structure calculations defined U($\mathbf{r}$) as a spherically symmetrical potential centered at the origin of the Wigner-Seitz unit cell; this makes the problem mathematically approachable, but neglects the contributions of neighboring unit cells near the boundaries (although various techniques have been developed to deal with this boundary issue). Another approach is to use a "muffin-tin" potential. In this technique, U($\mathbf{r}$) is defined as V(|$\mathbf{r}$-$\mathbf{R}$|) within a sphere of radius r_0 around each lattice site $\mathbf{r}$, and as $V(r_0) = 0$ outside this region, removing the lattice potential in the interstitial areas between atoms but maintaining it at atomic sites. Two common methods using a muffin-tin potential are the augmented plane-wave (APW) method, which uses a superposition of plane waves in the interstitial regions and atomic-orbital-like functions near the lattice sites, and the Green's function method (KKR), which starts with an integral form of the Schrodinger equation and substitutes in the potential and the Bloch wavefunctions to get a single equation dependent on k and r.

Another approach not using a muffin-tin potential is the orthogonalized plane-wave (OPW) method [9]. In this technique, the basis functions are the sum of a plane wave and a term orthogonalizing the function with respect to all core electron levels. An expansion on this is the pseudopotential method [10–12]. A pseudopotential is chosen which simplifies the actual potential near the core but matches it beyond a certain radius. Additionally, the plane wave basis functions are replaced with a set of pseudo wave functions, which do not have the radial nodes seen in the true wavefunction in the core region, but match this wavefunction outside the cutoff radius. Two common subtypes are norm-conserving and ultrasoft. In general, norm-conserving pseudopotentials (NCPP) are "harder" - they use a smaller cut-off radius, which requires including more plane-waves in the basis to capture the behavior near the atomic cores. This increases the transferability of the pseudopotentials between different chemical environments, at the cost of also increasing computational requirements. Ultrasoft

pseudopotentials (USPP) use a larger cut-off, making the opposite trade-off [13].

Density functional theory is a broad term for methods that replace the multi-electron wavefunction with an electron density function [14–16]. The electron energy is written as a functional[3] of this density. Because the density depends only on the spatial coordinates of the overall system, while the multi-electron wavefunction depends on the coordinates of each individual electron, the computational cost is greatly reduced. The energy functional includes a term for the interaction energy like those in the other methods discussed, but can also include an additional term for the exchange correlation energy. By choosing an appropriate exchange correlation term, the method can use the self-consistent field technique to iteratively reduce the energy and approach the ground state energy. This is known as the Kohn-Sham method, an extension of the Hartree-Fock SCF technique discussed earlier. Two common types of exchange correlation functionals are the local density approximation (LDA) and generalized gradient approximation (GGA). While DFT fails systematically for certain types of problems, it can be a powerful tool for computing electronic band structures.

It is worth noting that the various techniques discussed handle different areas of the overall problem, and thus can be combined with each other. The Hartree Fock SCF method and Density Functional Theory are two general approaches to finding the energy of electrons in a solid, looking for solutions to either the multi-electron Schrodinger equation or to its reformulation in terms of electron density. Both approaches require a set of basis wave functions (plane waves, atomic-orbital-like wavefunctions, etc), an approximation of the potential (muffin-tin, pseudopotentials, etc), and in some methods an exchange correlation term (LDA, GGA, non-DFT operations used to extend the Hartree-Fock method, etc).

[3] A function of a function

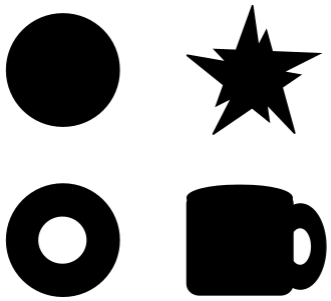

Figure 1-6. The objects within each row have the same topological genus, and can be smoothly transformed into each other. Between rows, the objects have different genuses (0 holes or 1 hole), and cannot be.

1.2 Topological materials

A topological insulator (TI) is usually defined as a material that is insulating in the bulk, but has symmetry-protected metallic surface states [17–19]. These states originate from the fact that the band structure of the TI is "inverted" or "knotted": the bands cannot be continuously deformed into an ordinary insulator without undoing the inversion. At the surfaces of a TI, the transition to a trivial topology must occur, because the vacuum beyond the material surface is an ordinary insulator. Thus the inverted bands must cross at the surface, closing the band gap as they meet there and creating the conductive surface states. Although a band inversion is required for a TI, it alone is not sufficient; the material must meet additional conditions for the surface states to be protected against disorder.

Topology is a branch of mathematics that studies the smooth deformation of objects. A canonical example of this is the comparison of a doughnut, a coffee cup, and a sphere. We can picture a doughnut being smoothly deformed into a coffee cup and vice versa, but a sphere cannot be transformed into either without poking a hole in it, which would not qualify as a smooth deformation (Figure 1-6). These two sets of objects (one hole versus no holes) are said to each have a different topological "genus"

- a characteristic number that is invariant under smooth transformations. Topological insulators and related materials are characterized by similar invariants, which depend on the curvature of the band structure: do the wavefunctions have a "knot"? These invariants can be determined by integrals over the Brillouin zone, and are unaffected by changes to the phase of the wavefunctions[4] So they can be considered a fundamental characteristic of the material; insulators with different invariants are in two distinct classes, analogous to objects with different genuses [19]

The first materials described as topological insulators were 2D materials displaying a quantized Hall conductivity under an applied magnetic field [26–29]. It was observed that the Hall resistance at low temperature and high field took on values proportional to an integer ν, referred to as the Chern number or the TKNN integer, which was shown to be a topological invariant [30]. This effect was initially observed in silicon-metal-oxide transistors (MOSFETs). Conductive 1D states appear at the edges of the MOSFET when the magnetic field is applied, although the electrons at the center remain localized, maintaining the bulk bandgap; these originate from the shape of the quantized bands (the Landau levels), which cross the Fermi level at their edges. Due to the symmetry breaking by the applied field, the edge states are chiral and the conduction electrons in them move in only one direction. The topology of the edge states - their "knotting" - can be explicitly connected to the Hall conductance and the Chern number [31, 32]. As the quantization of the Hall conductance depends on the topological invariant, it persists even if disorder creates a potential difference across the material [33].

[4]Operations that change the wavefunction's phase are known as gauge transformations (or rather, are one example of this kind of transformation). These phase changes can be physically observed in interference experiments, and can be induced by applying an electric potential or magnetic vector potential to the wavefunction, even if it is not exposed to the electric or magnetic field. If an observable property doesn't change under a gauge transformation, it is called gauge invariant. Although the phase does change under gauge transformations, if it is measured around a closed loop, the difference between the starting and ending phase is an invariant. This phase difference can be determined in a crystal by integrating the Berry curvature, a tensor dependent on the change of the wavefunctions when the wavevector $\mathbf{k}$ is smoothly (adiabatically) changed, over a closed surface (i.e., the Brillouin zone). The resulting Berry phase will be invariant modulo 2π. [20–25]

Although this effect depends on the presence of a magnetic field, a different type of 2D topological insulator can exist without one. These materials cannot display the integer quantum Hall effect described above, which depends on the broken TRS. However, analogous to the Hall effect is the spin Hall effect [34–36]. Both originate from the theory of relativity; in the ordinary Hall effect, an electron moving through a magnetic field experiences an effective electric field perpendicular to its movement by the Lorenz force, so also creating a perpendicular current. In the spin Hall effect, the analogue to the Lorenz force is the spin-orbit coupling, which induces an effective magnetic field around an electron moving through an electric field. Electrons on an atom or in a solid are always moving through the electric field of the nuclei, so SOC can act on them and split the energy levels. If TRS is present, SOC alone will not break it. However, if TRS is broken by an external field, SOC will affect the response. If a magnetic field is applied, the SOC will enhance it. If an electric field is applied, a spin polarization perpendicular to the field will be induced; this is known as the spin Hall effect. [37–39].

If the Hall effect can become quantized, why not the spin Hall effect? It was proposed that the quantized effect could occur in graphene, induced by spin-orbit coupling [40]. The spin-orbit coupling term in a Hamiltonian can be written as $\hat{H}_{SOC} = \lambda \cdot \hat{L} \cdot \hat{S}$. While the spin-free part of an N-electron electronic Hamiltonian has full spherical symmetry, in the sense that it commutes with all rotation operators, this is not true for $\hat{H}_{SOC}$. The $\hat{L}$ operator in the SOC term transforms as a pseudovector under rotations. Rather than a standard point group, the symmetry group of a Hamiltonian with SOC is instead a double group, which includes the anti-unitary TRS operator T. When spin-orbit coupling is included in a calculation of the electronic levels, it splits multiplets with the same L value into their components labeled by J. For example, the three p_l orbitals (p_{-1}, p_0, and p_1) will be split into two $p_{3/2}$ levels and one $p_{1/2}$ level. At $\mathbf{k} = 0$, p_{-1}, p_0, and p_1 are degenerate, but $p_{3/2}$ and $p_{1/2}$ are not.

In the absence of inversion symmetry, these levels will be further split by m_j value, yielding six bands at points other than $\mathbf{k} = 0$. However, at $\mathbf{k} = 0$ TRS will prevent this additional splitting.

In a system with SOC, where we must consider the spin of the electronic energy states, each state can be written as $E(\mathbf{k}, s)$, where $s =\uparrow$ or $\downarrow$ (+ or - s). Time-reversal symmetry requires that $E(\mathbf{k}, s) = E(-\mathbf{k}, -s)$. The symmetries of the energy states are described by a double group, and the operator T depends on the Pauli matrix σ_y. When TRS is unbroken and there is half-integer spin, it is also required that each state must be at least doubly degenerate (Kramers theorem). (Inversion symmetry, if present, requires that $E(\mathbf{k}, s) = E(-\mathbf{k}, s)$.) If the spin-orbit coupling term opens a band gap at a point where two bands of different parities cross each other, the states above and below the gap will have opposite signs at high-symmetry points. This sign difference means that the band structure is not topologically equivalent to an ordinary insulator, and that the gap must close at the edge of the material, where the transition back to an ordinary topology occurs. The degeneracy required by Kramers theorem forces the states closing this gap to cross at $\mathbf{k} = 0$. At the surfaces inversion symmetry is broken but time reversal is maintained, so the states at $\mathbf{k}$ and $-\mathbf{k}$ must have opposite spins. This results in conductive edge states in which electrons with opposite spins move in opposite directions (but there is electron motion in both directions, unlike in the IQHE). This should induce a spin current with a quantized spin Hall conductivity.

These spin Hall topological insulators turn out to be fundamentally different from the IQHE materials [41]. The topological invariant of the IQHE (the integer that the quantized Hall conductance is proportional to) cannot be used because the Hall effect cannot occur without breaking TRS, and the spin equivalent is lost under perturbations. However, the conductive edge states are protected as in the IQHE - a gap can't be opened at $\mathbf{k}$ without breaking the T symmetry. There must be a different

kind of topological invariant corresponding to these protected states. This is the $\mathbb{Z}_2$ invariant[5]. It can be determined by taking two integrals along a loop around half the Brillouin zone, set up so that all pairs $\mathbf{k}$ and -$\mathbf{k}$ are not in the same loop[6]. The $\mathbb{Z}_2$ depends on the number of sign changes around the loop, and takes the value zero for ordinary insulators and one for these quantum spin hall insulators. It can be used to classify time-reversal invariant materials, like the TKNN integer was used to classify quantum Hall states.

The idea of $\mathbb{Z}_2$ topological insulators can be extended to 3D materials [42, 43]. In 3D, there are four $\mathbb{Z}_2$ invariants, derived by considering the boundaries of planes through a torus model of the Brillouin zone. Three of these lead to what are considered "weak" topological insulators, which have conductive states only one particular surfaces, while the fourth is distinct and is associated with a category called "strong" topological insulators [44, 45]. Further discussion in this work will concern strong topological insulators unless otherwise noted. Just as in 2D, the $\mathbb{Z}_2$ invariants depend on the sign of the wavefunctions at the band gap - do a pair of states have the same or opposite signs? However, in 3D there are eight high-symmetry points (time-reversal invariant momenta, or TRIMS) that need to be considered. The $\mathbb{Z}_2$ invariant depends on a product of the signs at all these points. The conductive edge states become conductive surface states, and the places where these surface states cross each other in the band gap are called Dirac points.

In both 2D and 3D, these crossings must exist because of Kramer's theorem, which requires the degeneracy of all time reversal invariant states with half-integer spin. At most $\mathbf{k}$ values, this is fulfilled by having one spin state at $\mathbf{k}$ and the other at -$\mathbf{k}$, but at a TRIM, like $\mathbf{k} = 0$, the bands for each spin must intersect. It's possible for there to be multiple such band crossings, and the $\mathbb{Z}_2$ invariant is a product of all of them.

[5]The label $\mathbb{Z}_2$ means that the invariants are a group of integers ($\mathbb{Z}$) modulo 2. (So two non-equivalent values are possible)

[6]See references [41] and [42] for a more thorough mathematical treatment

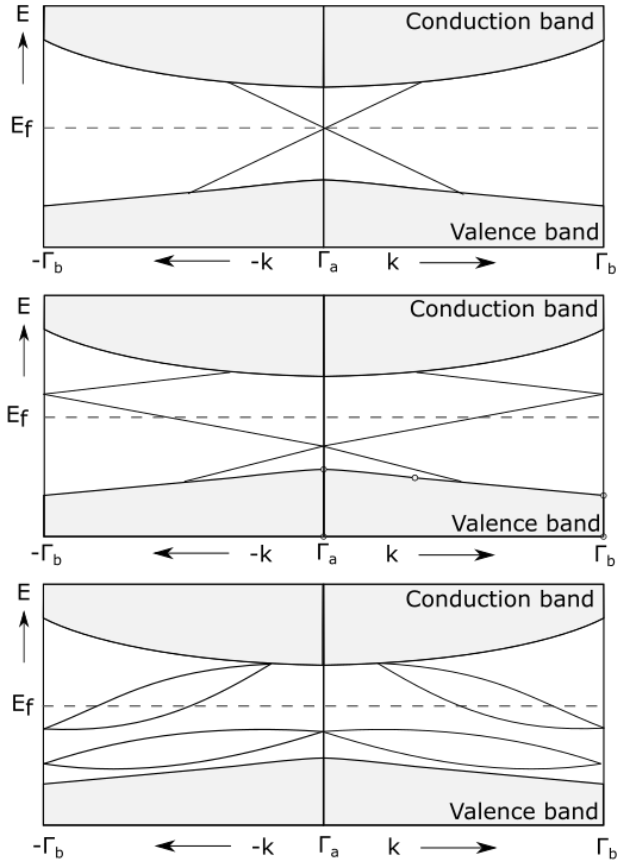

Figure 1-7. Edge/surface states arising from band inversions in a topological insulator. Time-reversal symmetry requires that the surface states cross at k = 0 (Γ_a). If there is an odd number of states, as in the top two figures, the Fermi level E_f must cross them at some point, so the metallic surface states are protected against small amounts of disorder. However, if there is an even number (bottom figure), disorder may move the Fermi energy away from the states and destroy their metallic character [18].

An odd number of crossings results in a topological insulator, and an even number (including zero) an ordinary insulator. With an even number of crossings, moving the Fermi level, or lowering the energy of the edge or surface states, can result in these states no longer crossing the Fermi level, removing their metallic nature. However, with an odd number of states, this cannot be done without breaking the degeneracy at a TRIM (Figure 1-7). The metallic character of these states is therefore protected by the time reversal symmetry.

In crystals with inversion symmetry, calculating a $\mathbb{Z}_2$ invariant is particularly simple - it can be done just by multiplying the parities of each occupied band at the TRIM points [46]. In non-inversion symmetric materials it is more difficult, but *ab initio* computational methods have been developed [47].

The next step is to find a real topological insulator. We already have a list of requirements for such a material: it must be a bulk insulator, it must have time reversal symmetry, it will most likely have strong spin-orbit coupling, the number of crossings within the bandgap must be odd, and it must be chemically stable [48]. The strength of SOC increases with the atomic number, due to the larger electric field from the nucleus, so the material should have heavy elements. As such, graphene is not likely to work. Additionally, the bandgap opened by SOC will be relatively small, so candidate materials should be semiconductors with bandgaps of a plausible size. It is also possible for a bandgap with a parity inversion to arise from effects other than SOC, such as the inert pair effect [45]. However, the same requirements of heavy elements and small bandgaps apply for this effect.

The first 2D topological insulator was physically realized in 2007 in HgTe/(Hg,Cd)Te [49]. Behavior consistent with conductive edge states was observed in appropriately sized quantum wells of this material, in accordance with theoretical predictions [50]. Similarly, $Bi_{1-x}Sb_x$ was predicted to be a three dimensional topological insulator shortly before the surface states were observed via ARPES measurements [46, 51]. Verifying a 3D topological insulator via transport measurements is difficult, because the surface conductivity is small and the surface and bulk conductivities must be separated. However, ARPES can directly observe the surface states and distinguish them from the bulk band structure. Additionally, the expected spin directionality on the surfaces has been observed and the insensitivity of the surface states to defects has been verified [52–55].

Bi_2Se3 and similar materials have also been proposed and then realized as topolog-

ical insulators [56]. Bi_2Se_3 has the advantage of a significantly larger bandgap than $Bi_{1-x}Sb_x$: ≈ 0.3 eV, which allows for potential applications at room temperature. Topological surface states and spin momentum locking were successfully demonstrated in Bi_2Se3. However, the bulk Fermi energy of Bi_2Se3 as usually grown does not lie in the band gap, contrary to theoretical predictions. This is likely due to selenium vacancies, and was compensated by doping with $< 1\%$ Ca, inducing insulating behavior [57].

Topological insulators hold promise for applications in spintronics and quantum computing. The field of topological materials encompasses many other classes of materials and effects, like topological superconductors, Majorana bound states, and Weyl and Dirac semimetals. One prediction is that a half-integer quantized Hall effect, or equivalently, a magnetoelectric polarization, will occur if a gap is opened in the surface states by breaking TR symmetry [58, 59]. It is also possible to redefine topological insulators in terms of this magnetoelectric effect. The work in this thesis centers on the search for these magnetoelectric materials - axion insulators - and the theory behind them will be covered in detail in Chapter 2.

1.3 Magnetism

Magnetism in materials is fundamentally a quantum effect, arising from interactions between electron spins [60, 61]. The observable magnetic attraction and repulsion seen in materials like refrigerator magnets or neodymium magnets occurs when unpaired spins interact with each other via magnetic exchange, aligning in the same direction. This phenomenon, known as ferromagnetism, is one of several options for the arrangement of spins in a solid.

These options can be categorized by their behavior in an applied magnetic field. In materials with no unpaired spins, known as diamagnets, there will be a weak repulsion

against an applied field, resulting in a small negative magnetic moment that does not vary with temperature. For materials that do have unpaired spins, the simplest option is a paramagnet. In a paramagnet, the strength of the interaction between spins is less than the thermal energy, so the spins move around randomly instead of aligning. However, the spins will align in the direction of an applied magnetic field, creating a measurable moment. There are two microscopic origins of paramagnetism - the local magnetic moments on atoms, and the Pauli paramagnetism of conduction electrons. Local moment magnetism is temperature dependent, while Pauli paramagnetism is a temperature independent constant.

Ferromagnetism occurs when the magnetic exchange makes it energetically favorable for spins to align. There are several models for magnetic exchange, but a common one is the Ising model, where the interaction is described by

$$U = -J \sum_{ij} S_i \cdot S_j \tag{1.10}$$

U is the interaction energy, S_i and S_j are the spins of two neighboring atoms, which are magnetic moments pointing either up or down. J is the exchange integral / magnetic coupling and can be positive or negative. Positive J values represent ferromagnetic exchange, while negative values represent antiferromagnetic. In an antiferromagnet, the spins still interact with each other, but in a way that prefers alignment in the opposite direction of neighboring spins. For example, a 1D antiferromagnetic chain of atoms will have spins pointing alternately up and down. An alternative model for magnetic exchange is the Heisenberg model, in either its classical form where the spin vectors S_i and S_j can point in any direction, or its quantum form in which the spins are quantum-mechanical operators rather than classical vectors.

Spin alignments are complicated by the composition and geometry of materials. There may be more than one type of magnetic ion in a material, and the magnetic

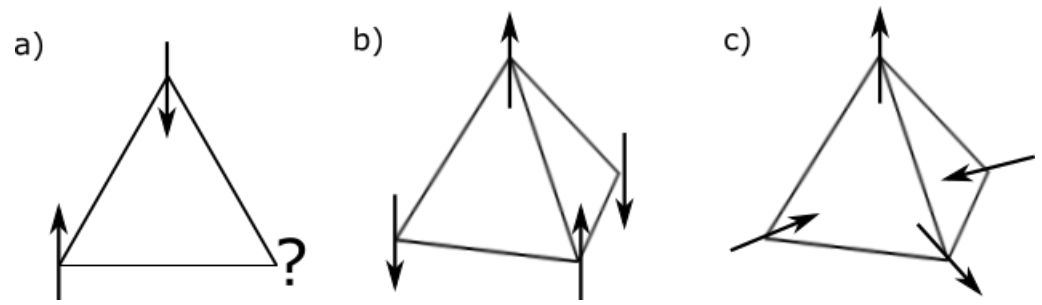

Figure 1-8. Three example of magnetic frustration. (a) A triangular lattice with antiferromagnetic exchange between spins. The third spin, labeled with a question mark, cannot align antiferromagnetically with both others. (b) A tetrahedron with antiferromagnetic exchange. Six degenerate two-up two-down spin configurations are possible. (c) a tetrahedron with ferromagnetic exchange and spins oriented along the rotational axes of the tetrahedron. Again, there are six degenerate lowest-energy configurations, each with two spins pointing in and two pointing out.

moments are frequently not arranged in a line, but can be in a wide variety of configurations depending on the material structure. Additionally, a moment may interact not only with the directly adjacent moments, but also with those further away in the material. Thus, magnetic behavior can become extremely complex. Spin-orbit coupling can also play a role, changing the effective spin of an atom and increasing its magnetic moment. This is especially significant in heavy f-block elements.

One important type of geometry-driven phenomenon is magnetic frustration [62]. This occurs when a set of magnetic ions have antiferromagnetic exchange, but their geometry prevents them from achieving the favored orientation with respect to all neighbors. A classic example is the triangle shown in Figure 1-8a. If one spin is up and another is down, the third spin cannot have an opposite alignment with both. Geometric frustration can also occur in tetrahedra. Depending on the alignment of the spins, either antiferromagnetic or ferromagnetic exchange can be frustrated (Figure 1-8 b&c).

Geometric frustration may be resolved by spins tilting to take on a magnetic order, or it may lead to a superposition of degenerate states. This second option is a necessary but not sufficient feature for a kind of material known as a quantum spin

liquid (QSL), which is a major focus of quantum materials research [63]. A quantum spin liquid retains its disordered state down to 0 K. It has been proposed that the ground state of a QSL is a resonating valence bond solid. In an ordinary valence bond solid, all spins pair up into spin zero singlet states. They are maximally entangled with the spin they are paired with, but not at all entangled with the other spins. In a QSL, instead of a single arrangement of localized singlet states, the ground state is a superposition (resonance hybrid) of many degenerate arrangements of singlets. The valence bonds in a QSL may be formed by nearest neighbors, or by pairs of spins further away from each other. This can lead to unusual excited states with fractional quantum numbers. QSL states may also be related to high-temperature superconductivity, a third major area of quantum materials research.

One example of a lattice that can host magnetic frustration is the honeycomb lattice (Figure 1-9). Each layer of a honeycomb structure contains a 2D network of hexagons. It can be described as a hexagonal Bravais lattice with a two-atom basis, or as two interpenetrating triangular lattices. It may host a variety of magnetic orders, depending on the exchange between an atom and its three nearest neighbors. In addition to purely ferromagnetic or purely antiferromagnetic (Neél) orders, a mix of FM and AFM exchange can lead to zig-zag or stripy AFM orders. Besides exchange between neighbors in the *ab* plane, the magnetic exchange between planes along the *c* direction must be considered; exchange between second-, third-, and fourth- nearest neighbors within a plane can also be significant [64, 65].

In addition to the complex magnetic ordering possible on a honeycomb lattice, it may also assume spin glass or singlet states at low temperature, or potentially even a quantum spin liquid state [66–68]. In the Kitaev model for magnetic exchange on a honeycomb lattice, the three bonds around an atom in the lattice are described by three different exchange interactions (XX, YY, and ZZ) [69]. This is similar to the Heisenberg model but is less symmetric because the three interactions need not be of

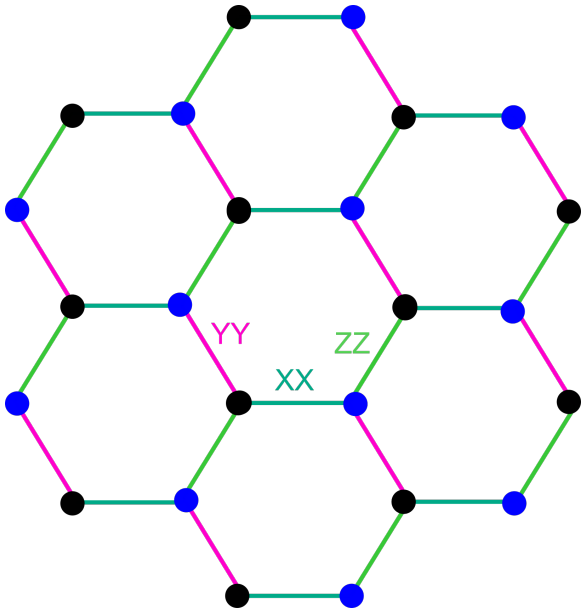

Figure 1-9. The Kitaev model on the honeycomb lattice. XX, YY, and ZZ indicate the three different magnetic exchange interactions between pairs of atoms on the lattice. Blue and black dots show the two interpenetrating triangular lattices the honeycomb lattice is composed of.

equal strength. This model can be solved exactly for $S = \frac{1}{2}$, allowing computation of the both QSL ground state and its excitations. As a result, there has been a great deal of recent interest in potential Kitaev spin liquid materials, with candidates including honeycomb iridates, α-$RuCl_3$, and cobalt honeycombs [70].

1.4 Methods

1.4.1 Solid-state synthesis

Solid-state synthesis, as the name suggests, refers to chemical reactions where all starting materials are in solid form, and reactions are carried out between them directly instead of in a liquid solution [71]. The most basic form is known as "shake and bake" chemistry: the powdered starting materials are mixed together and then heated. This requires high temperatures and long reaction times, because diffusion between solid reactants is very slow. Most of the reactions in this work were carried out under

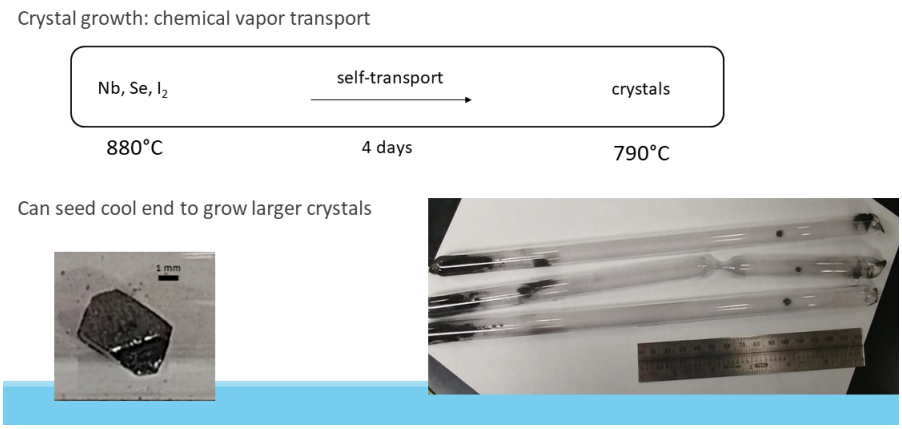

Figure 1-10. Top: A schematic of the chemical vapor transport (CVT) growth of $Nb_4Se_4I_4$ crystals. Using I_2 as a self-transport agent, materials vaporize at the hot end of the tube and deposit at the cool end. Bottom left: A crystal produced by CVT. Bottom right: Evacuated quartz reaction ampoules after a seeded CVT growth.

vacuum or argon in a sealed quartz ampoule, but reactions conducted under flowing gas are also common.

Growth of large single crystals is frequently desirable. While crystals of some materials can be grown by direct heating, somewhat more complicated methods are frequently much more effective. I'll discuss a few of them below. However, there are many additional techniques that are not covered here.

1.4.2 Chemical vapor transport

Chemical vapor transport (CVT) relies on the volatilization and deposition of the reactants [72]. Starting materials are placed at one end of a furnace with a temperature gradient. The higher end of the gradient is at the reactants, which vaporize and then deposit at the cool end, hopefully in the form of crystals. If the reactants are not sufficiently volatile, a small amount of some other transport agent, most frequently a halogen, is included as a catalyst. CVT is highly thermodynamic, relying on the equilibrium position of the transport and deposition reactions for crystal growth.

1.4.3 Flux growth

Flux growth is often used to obtain crystals from high-melting-point starting materials [73]. The reactants are heated with a large quantity of some low melting flux. After initial heating to dissolve the reactants in the flux solution, the reaction is slowly cooled to allow the nucleation and growth of crystals. After cooling and quenching, the reaction is centrifuged or etched to remove the flux and recover the crystals. Flux growth can grow a wide variety of oxide and intermetallic compounds, although it often results in smaller crystal sizes than other methods. An understanding of the phase equilibria of the reactant and flux is necessary for determining growth conditions.

1.4.4 Floating zone

Floating zone methods are a form of melt growth where a rod of starting material is moved through an area of focused light which creates a molten zone [73]. As the molten zone is moved up the rod, the rod melts and recrystallizes section by section. This can result in very large crystals, and the lack of a crucible reduces the chance of impurities. The light source may be either reflected infrared light from a halogen or xenon lamp (optical floating zone) or a system of lasers (laser diode floating zone). The traveling solvent floating zone technique, which combines the floating zone and flux techniques by moving the molten zone up a rod of reactants and solvent, is also used.

1.4.5 X-ray diffraction

X-ray wavelengths are on the same order of magnitude as interatomic distances, making them useful probes for the structure of crystals [2]. X-rays are scattered by their interactions with the electron cloud around an atom. In a periodic crystal structure, x-rays scattered from adjacent planes of atoms will interfere constructively according to Bragg's law: $n\lambda = 2d\sin\theta$, where λ is the x-ray wavelength, d is the distance

between planes, θ is the scattering angle, and n is an integer. So, at a particular scattering angle, planes separated by distance d will be observed; by rotating through a range of θ angles, we can see each set of ordered planes in the structure. Alternatively, we can use the Laue condition, under which constructive interference will occur when $\mathbf{R} \cdot (\mathbf{k} - \mathbf{k}') = 2\pi m$. $\mathbf{R}$ is a site in the lattice, $\mathbf{k}$ is the incident wave vector, and $\mathbf{k}'$ is the scattered wave vector. This can equivalently be written as $e^{i(\mathbf{k}-\mathbf{k}')\cdot\mathbf{R}} = 1$, which is the definition of the reciprocal lattice. So, we will observe a constructive interference when the change in wavevector with scattering $\mathbf{k} - \mathbf{k}'$ is a reciprocal lattice vector. The Bragg and Laue conditions are equivalent; the angle between $\mathbf{k}$ and $\mathbf{k}'$ is the scattering angle θ. Which formulation is most useful depends on the experimental geometry. In both methods, a peak (referred to as a Bragg peak) is observed for each scattering angle that allows constructive interference. For a single crystal, a full set of reflections can be measured by rotating the crystal with respect to a single-wavelength incident x-ray and recording each Bragg peak. This will yield detailed information that can then be used for structure determination. In another method, usually referred to as Laue diffraction, the crystal is left at a fixed orientation and an x-ray beam with a range of wavelengths is used. Bragg reflections for reciprocal lattice vectors within the wavelength range are observed, and others are excluded, allowing easy determination of the orientation of the crystal. A third method is x-ray powder diffraction. Because a powder is essentially a collection of small crystals of every orientation, the reflections for all crystal orientations will be seen as the scattering angle is varied. Although some information is lost by not looking at each orientation separately (making full structure determination harder, but not necessarily impossible), this technique produces a characteristic set of peaks that is useful for studying the details of a materials structure if the basics are already known. Databases of powder XRD patterns are maintained, which allow easy identification of materials by comparing their observed patterns to those already known.

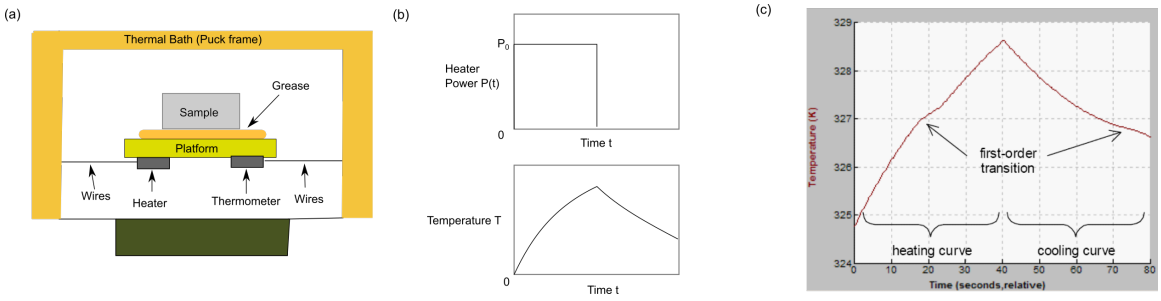

Figure 1-11. (a) A schematic of a PPMS heat capacity puck (not to scale). (b) Typical heater power and thermal relaxation curves for a semi-adiabatic heat capacity pulse. (c) A thermal relaxation curve indicating a first-order phase transition, requiring use of a long-pulse slope analysis method [74].

1.4.6 Magnetization

The primary physical characterization in this work - magnetization, heat capacity, and resistivity - was performed mainly on a Quantum Design Physical Properties Measurement System (PPMS). The system can apply a constant longitudinal magnetic field up to 9 T with a superconducting niobium-titanium solenoid magnet, cooled by liquid helium. Magnetization is measured by inserting samples into an ACMS coilset which sits within the solenoid magnet and contains both detection coils and AC drive coils. For DC measurements, the sample is moved vertically within the coilset, inducing a signal in the detection coil as its magnetic moment M changes position in the applied field H. The resulting signal is then analyzed with a digital signal processor to determine the moment based on H and temperature T. For AC, a small oscillating moment is applied by a drive coil, in addition to the constant field H. Using a system of detection and calibration coils, the AC susceptibility (the local slope of the true susceptibility M/H) is determined, with both the real and imaginary components reported.

1.4.7 Heat capacity

The heat capacity of a material is the change in temperature that results when a quantity of heat is added to a sample. For a PPMS heat capacity measurement, the sample is mounted on a platform, and a known amount of heat is applied via a heater attached to the bottom of the platform. Temperature is measured during and after heating, and the temperature response is fit to a model that accounts for the thermal relaxation of the sample and platform. This model is used to calculated the heat capacity at constant pressure

$$C_p = (\frac{dQ}{dT})_p \tag{1.11}$$

The method used by the PPMS for measuring heat capacity is a semi-adiabatic relaxation technique. In contrast to an adiabatic method, where the sample must be in total thermal isolation and the heat capacity C can be calculated directly from the change in sample temperature ΔT, the semi-adiabatic method accounts for heat loss by finding a time constant for the thermal relaxation of the sample. It requires that C be constant over the temperature range ΔT. A simple model for the relaxation, which applies if the sample and sample platform are in good thermal contact, is

$$C_{total}\frac{dT}{dt} = -K_w(T - T_b) + P(t) \tag{1.12}$$

where T is the temperature of the sample platform as a function of time t, T_b is the temperatue of the thermal bath, K_w is the thermal conductance of the wires supporting the sample platform, and $P(t)$ is the heater power, equal to P_0 while applying a heating pulse and 0 during the cooling portion of the measurement. The components of the experimental setup and sample plots of heater power and relaxation curves are shown in Figure 1-11. C_{total} is the heat capacity of the sample (if present), platform, and grease. The heating and cooling parts of the *T(t)* curves are described

by exponential functions with time constant $\tau = C_{total}/K_w$. This model is used for addenda measurements, which find the heat capacity of the platform and grease before mounting the sample.

A more accurate way of fitting the relaxation curve is the two-tau model. This model uses two time constants instead of one: τ_1 for the heat flow between the platform and the thermal bath (the frame of the sample puck) and τ_2 for the heat flow between the sample and the platform. The two-tau model is written as

$$C_{platform}\frac{dT_p}{dt} = P(t) - K_w(T_p(t) - T_b) + K_g(T_s(t) - T_p(t)) \tag{1.13}$$

$$C_{sample}\frac{dT_s}{dt} = -K_g(T_s(t) - T_p)t)) \tag{1.14}$$

Here $T_s(t)$ and $T_p(t)$ are the temperature versus time of the sample and the platform respectively, and K_g is the thermal conductance of the grease. $C_{platform}$ is determined by an addenda measurement, and other parameters including τ_1 and τ_2 are computed using a least-squares fit to the $T(t)$ curve.

The semi-adiabatic model fails if the heat capacity C changes over the temperature range of the measurement. This makes it unsuitable for first-order phase transitions, in which there is a steep increase in heat capacity that cannot be approximated as constant over ΔT [75]. Figure 1-11c shows a characteristic relaxation curve for a first-order phase transition, with the distortion in the heating and cooling curves indicating that exponential fits to the full curves are insufficient. One method used in these cases is slope analysis, which fits small sections of the heating and cooling curves to extract multiple heat capacity measurements. This allows measurement time to be decreased by using a small number of long heating pulses instead of many short ones. Equation 1.12 is divided by $\frac{dT}{dt}$ to give

$$C_{total} = \frac{P(t) - K_w(T(t) - T_b)}{dT/dt} \tag{1.15}$$

This can be further improved by combining expressions for the heating and cooling curves (dual-slope analysis). Although the PPMS Multiview software can perform this analysis, additional corrections are needed to get accurate heat capacity values from long pulses. One such correction is the recomputation of temperatures directly from thermometer resistance, as the values computed by the Multiview software are unreliable at large $T_b - T_s$. A correction to the wire conductivity K_w is also necessary, as it will vary from the value measured during puck calibration depending on sample size, position, and internal conductivity. The corrected K_w can be determined from semi-adiabatic short-pulse measurements of the sample. These corrections, and a more accurate calculation of heat capacity at a first-order transition, can be performed by the software LongPulseHC [76].

Heat capacity can provide information about the vibrational modes, conduction electrons, and magnetism of a material. The lattice heat capacity can be fit to the Debye or Einstein models to estimate the vibrational modes (phonons). Although measurements determine the constant pressure heat capacity C_p and these phonon models are for the constant volume heat capacity C_v, at low temperatures the two heat capacities are nearly identical. Phonon heat capacity has a T^3 dependence at low temperatures but conduction electrons heat capacity has a linear dependence on T, so the two components can be separated fairly easily. If there is a magnetic contribution as well, it is usually necessary to subtract the phonon heat capacity determined from an isostructural non-magnetic analogue.

Additionally, heat capacity provides information about phase transitions, whether structural, magnetic, or electron. Because of the change in entropy, phase transitions will show up as a peak in heat capacity. The entropy change can be calculated by

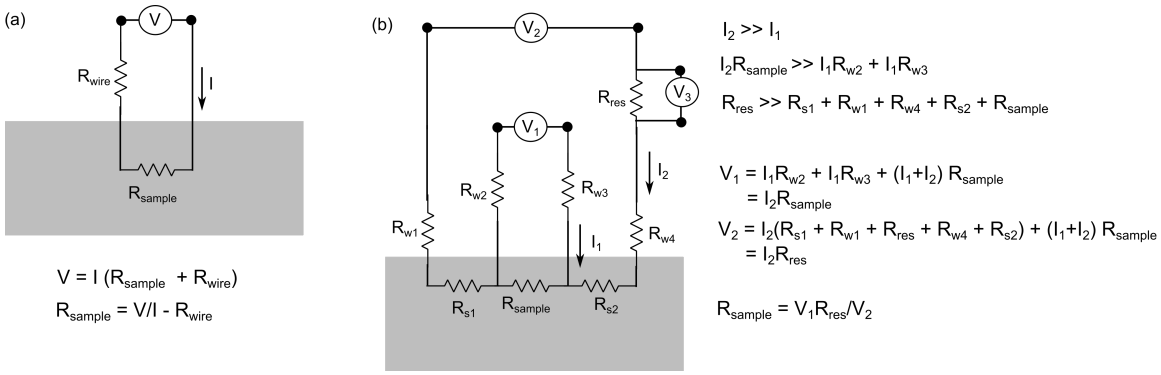

Figure 1-12. A comparison of (a) two-wire and (b) four-wire resistance measurements. The sample being measured is shown as a grey rectangle. In (b), the R_w are the resistance of the wires / contacts, the R_s are the resistance of the sample between leads, and R_{res} is the resistance of a large resistor. With an appropriate choice of R_{res} and the applied current I_2, R_{sample} can be computed without needing to know the R_w.

$$\Delta S = \int \frac{C}{T} dT \tag{1.16}$$

1.4.8 Resistivity

The resistivity of a sample is measured by applying a current through thin platinum leads attached to the surface, and then measuring the change in voltage across the sample. Typically a four-wire geometry is used, which allows the removal of contact resistances from the measured result (Figure 1-12). Resistivity measurements provide information about the electronic structure of a material. Metallic materials will have a small resistivity that increases with temperature, while the resistivity of a semiconductor will decrease as temperature goes up. (The resistivity of an insulator is similar, but is often too large to measure effectively even at room temperature). In a semiconductor, the size of the band gap can be estimated from the resistivity versus temperature curve.

The PPMS also permits measurement of other electronic transport properties, such as Hall coefficients. Additionally, the sample chamber can be connected to external setups via a breakout box, to use the thermal control and/or magnetic fields of the

PPMS with other measurement systems.

Bibliography

[1] T. M. McQueen, https://occamy.chemistry.jhu.edu/research/index.php, accessed: 2021-06-28.

[2] N. Ashcroft and N. Mermin, *Solid State Physics* (Saunders College, Philadelphia, 1976).

[3] C. P. Brock, *International Tables for Crystallography, Volume A: Space Group Symmetry*, International Tables for Crystallography (Kluwer Academic Publishers, 2002).

[4] J. Gazalet, S. Dupont, J. Kastelik, Q. Rolland, and B. Djafari-Rouhani, Wave Motion **50**, 619 (2013).

[5] G. Floquet, Annales scientifiques de l'École Normale Supérieure **12**, 47 (1883).

[6] F. Bloch, Z. Phys. **52**, 555 (1929).

[7] R. Hoffmann, Angewandte Chemie International Edition in English **26**, 846 (1987).

[8] D. R. Hartree, Mathematical Proceedings of the Cambridge Philosophical Society **24**, 111–132 (1928).

[9] J. C. Phillips and L. Kleinman, Phys. Rev. **116**, 287 (1959).

[10] M. C. Payne, M. P. Teter, D. C. Allan, T. A. Arias, and J. D. Joannopoulos, Rev. Mod. Phys. **64**, 1045 (1992).

[11] V. Heine, Solid State Physics **24**, 1 (1970).

[12] J. C. Phillips, Phys. Rev. **112**, 685 (1958).

[13] D. Vanderbilt, Phys. Rev. B **41**, 7892 (1990).

[14] P. R. Tulip, *Dielectric and lattice dynamical properties of molecular crystals via density functional perturbation theory: implementation within a first principles code*, Ph.D. thesis, Durham University, Durham City, United Kingdom (2004).

[15] M. C. Gibson, *Implementation and application of advanced density functionals*, Ph.D. thesis, Durham University, Durham City, United Kingdom (2006).

[16] W. Kohn, A. D. Becke, and R. G. Parr, J. Phys. Chem. **100**, 12974 (1996).

[17] Y. Ando, J. Phys. Soc. Jpn. **82**, 102001 (2013).

[18] M. Z. Hasan and C. L. Kane, Rev. Mod. Phys. **82**, 3045 (2010).

[19] J. Moore, Nature (London) **464**, 194 (2010).

[20] J. Schwichtenberg, arXiv preprint **1901.10420** (2019).

[21] M. V. Berry, Proc. R. Soc. A **392**, 45 (1984).

[22] R. Resta, J. Phys.: Condens. Matter **12**, R107 (2000).

[23] E. Cohen, H. Larocque, F. Bouchard, F. Nejadsattari, Y. Gefen, and E. Karimi, Nature Reviews Physics **1**, 1 (2019).

[24] J. Zak, Phys. Rev. Lett. **62**, 2747 (1989).

[25] D. Xiao, M.-C. Chang, and Q. Niu, Rev. Mod. Phys. **82**, 1959 (2010).

[26] A. P. Schnyder, S. Ryu, A. Furusaki, and A. W. W. Ludwig, AIP Conf. Proc. **1134**, 10 (2009).

[27] R. M. Kaufmann, D. Li, and B. Wehefritz-Kaufmann, Reviews in Mathematical Physics **28**, 1630003 (2016).

[28] K. v. Klitzing, G. Dorda, and M. Pepper, Phys. Rev. Lett. **45**, 494 (1980).

[29] R. B. Laughlin, Phys. Rev. B **23**, 5632 (1981).

[30] D. J. Thouless, M. Kohmoto, M. P. Nightingale, and M. den Nijs, Phys. Rev. Lett. **49**, 405 (1982).

[31] D. P. Arovas, R. N. Bhatt, F. D. M. Haldane, P. B. Littlewood, and R. Rammal, Phys. Rev. Lett. **60**, 619 (1988).

[32] Y. Hatsugai, Phys. Rev. Lett. **71**, 3697 (1993).

[33] B. I. Halperin, Phys. Rev. B **25**, 2185 (1982).

[34] J. Wunderlich, B. Kaestner, J. Sinova, and T. Jungwirth, Phys. Rev. Lett. **94**, 047204 (2005).

[35] Y. K. Kato, R. C. Myers, A. C. Gossard, and D. D. Awschalom, Science **306**, 1910 (2004).

[36] S. Murakami, N. Nagaosa, and S.-C. Zhang, Phys. Rev. Lett. **93**, 156804 (2004).

[37] M. I. Dyakonov, in *Future Trends in Microelectronics*, edited by S. Luryi, J. Xu, and A. Zaslavsky (Wiley, 2010) pp. 251–263.

[38] Y. K. Kato, R. C. Myers, A. C. Gossard, and D. D. Awschalom, Science **306**, 1910 (2004).

[39] V. Zayets, `https://staff.aist.go.jp/v.zayets/zayets_content.html`, accessed: 2021-06-01.

[40] C. L. Kane and E. J. Mele, Phys. Rev. Lett. **95**, 226801 (2005).

[41] C. L. Kane and E. J. Mele, Phys. Rev. Lett. **95**, 146802 (2005).

[42] J. E. Moore and L. Balents, Phys. Rev. B **75**, 121306 (2007).

[43] L. Fu, C. L. Kane, and E. J. Mele, Phys. Rev. Lett. **98**, 106803 (2007).

[44] Z. Ringel, Y. E. Kraus, and A. Stern, Phys. Rev. B **86**, 045102 (2012).

[45] N. Kumar, S. N. Guin, K. Manna, C. Shekhar, and C. Felser, Chemical Reviews **121**, 2780 (2021).

[46] L. Fu and C. L. Kane, Phys. Rev. B **76**, 045302 (2007).

[47] A. A. Soluyanov and D. Vanderbilt, Phys. Rev. B **83**, 235401 (2011).

[48] O. I. Malyi, G. M. Dalpian, X.-G. Zhao, Z. Wang, and A. Zunger, Materials Today **32**, 35 (2020).

[49] M. König, S. Wiedmann, C. Brüne, A. Roth, H. Buhmann, L. W. Molenkamp, X.-L. Qi, and S.-C. Zhang, Science **318**, 766 (2007).

[50] B. A. Bernevig, T. L. Hughes, and S.-C. Zhang, Science **314**, 1757 (2006).

[51] D. Hsieh, D. Qian, L. Wray, Y. Xia, Y. Hor, R. Cava, and M. Z. Hasan, Nature (London) **452**, 970 (2008).

[52] D. Hsieh, Y. Xia, L. Wray, D. Qian, A. Pal, J. H. Dil, J. Osterwalder, F. Meier, G. Bihlmayer, C. L. Kane, Y. S. Hor, R. J. Cava, and M. Z. Hasan, Science **323**, 919 (2009).

[53] T. Zhang, P. Cheng, X. Chen, J.-F. Jia, X. Ma, K. He, L. Wang, H. Zhang, X. Dai, Z. Fang, X. Xie, and Q.-K. Xue, Phys. Rev. Lett. **103**, 266803 (2009).

[54] P. Roushan, J. Seo, C. Parker, Y. Hor, D. Hsieh, D. Qian, A. Richardella, M. Z. Hasan, R. Cava, and A. Yazdani, Nature (London) **460**, 1106 (2009).

[55] Z. Alpichshev, J. G. Analytis, J.-H. Chu, I. R. Fisher, Y. L. Chen, Z. X. Shen, A. Fang, and A. Kapitulnik, Phys. Rev. Lett. **104**, 016401 (2010).

[56] A. Bansil, H. Lin, and T. Das, Rev. Mod. Phys. **88**, 021004 (2016).

[57] Y. Hor, J. Checkelsky, D. Qu, N. Ong, and R. Cava, J. Phys. Chem. Solids **72**, 572 (2011).

[58] X.-L. Qi, T. L. Hughes, and S.-C. Zhang, Phys. Rev. B **78**, 195424 (2008).

[59] A. M. Essin, J. E. Moore, and D. Vanderbilt, Phys. Rev. Lett. **102**, 146805 (2009).

[60] J. B. Goodenough, *Magnetism and the Chemical Bond* (Interscience Publishers, 1963).

[61] B. Cullity and C. Graham, *Introduction to Magnetic Materials* (John Wiley& Sons, 2009).

[62] A. P. Ramirez, Annual Review of Materials Science **24**, 453 (1994).

[63] L. Balents, Nature **464**, 199 (2010).

[64] J. R. Morey, A. Scheie, J. P. Sheckelton, C. M. Brown, and T. M. McQueen, Phys. Rev. Materials **3**, 014410 (2019).

[65] E. A. Zvereva, M. I. Stratan, A. V. Ushakov, V. B. Nalbandyan, I. L. Shukaev, A. V. Silhanek, M. Abdel-Hafiez, S. V. Streltsov, and A. N. Vasiliev, Dalton Trans. **45**, 7373 (2016).

[66] C. Broholm, R. J. Cava, S. A. Kivelson, D. G. Nocera, M. R. Norman, and T. Senthil, Science **367** (2020).

[67] A. A. Aczel, Z. Zhao, S. Calder, D. T. Adroja, P. J. Baker, and J.-Q. Yan, Phys. Rev. B **93**, 214407 (2016).

[68] S. Derakhshan, J. E. Greedan, and L. M. D. Cranswick, **arXiv preprint** (2007).

[69] A. Kitaev, Ann. Phys. **321** (2006).

[70] J. R. Chamorro, T. M. McQueen, and T. T. Tran, Chem. Rev. **121**, 2898 (2021).

[71] A. R. West, *Basic Solid State Chemistry* (Wiley, 1999).

[72] M. Binnewies, *Chemical Vapor Transport Reactions* (De Gruyter, 2012).

[73] M. Tachibana, *Beginner's Guide to Flux Crystal Growth* (National Institute for Materials Science (NIMS) / Springer, 2017).

[74] Q. Design, `https://www.qdusa.com/pharos/`, accessed: 2021-07-12.

[75] J. Lashley *et al.*, Cryogenics **43**, 369 (2003).

[76] A. Scheie, J. Low Temp. Phys. **193**, 60 (2018).

Chapter 2

The search for an intrinsic axion insulator

2.1 Motivation and background

Axion insulators are a new category of quantum material, theoretically proposed but not yet definitively observed. They are closely related to the $\mathbb{Z}_2$ topological insulators described in the previous chapter. A key feature of these topological insulators is their time-reversal symmetry, which protects the metallic edge or surface states, preventing them from becoming gapped. But what if we break this TR symmetry by applying a magnetic field or including magnetic atoms in the material? The conductivity of the surfaces states will be lost, but the band structure will still be topological, with band inversions still present across the bulk bandgap. The resulting material, known as an axion insulator, is predicted to have a large quantized magnetoelectric effect [1–3].

In a material with a magnetoelectric response, an applied magnetic field (H_j) will induce an electrical polarization (P_i), and an applied electric field (E_j) will induce a magnetization (M_i). The most commonly studied form, the linear magnetoelectric effect, can be written as

$$P_i = \sum_j \epsilon_0 \chi^e_{ij} E_j + \sum_j \alpha_{ij} H_j \tag{2.1}$$

$$M_i = \sum_j \mu_0 \chi^v_{ij} H_j + \sum_j \alpha_{ij} E_j \tag{2.2}$$

In these equations, the first terms are the more standard couplings of polarization with electric field and magnetization with applied magnetic field, and the second terms are the magnetoelectric coupling. The size and direction of this coupling are given by the tensor α_{ij}. For most materials, all components of α_{ij} are zero, but in some compounds, such as Cr_2O_3 and multiferroic materials, a non-zero magnetoelectric response can be observed [4–6]. The potential applications of strongly magnetoelectric materials include sensitive magnetic field sensors, electrical transformers, and microwave devices. The magnetoelectric coupling in Cr_2O_3 is around 1.04 ps/m [7]. In comparison, an axion insulator could have magnetoelectric coupling as large as 24.3 ps/m [8].

One component of the magnetoelectric coupling, the Chern-Simons polarization, is an isotropic response measured in terms of a parameter θ where [9, 8, 10]

$$\alpha^{CS}_{ij} = \theta \frac{e^2}{2\pi h} \delta_{ij} \tag{2.3}$$

In this equation, θ is dimensionless, e is the charge of the electron, h is Planck's constant, and δ_{ij} is a delta-function ensuring that the response is isotropic. In materials with unbroken time reversal or inversion symmetry, θ, called the axion coupling, is quantized to be either 0 or π. In conventional magnetoelectrics like Cr_2O_3, this quantization does not occur, θ is small, and thus α^{CS} is small. However, in a material with $\theta = \pi$ the magnetoelectric effect will be extremely large. The quantized θ corresponds to the $\mathbb{Z}_2$ invariant in topological insulators [11].

This magnetoelectic coupling term corresponds to a Lagrangian dependant on the magnetic and electric fields, which is added to the equations of motion. In the equation for this Lagrangian (2.4), $\mathbf{E}$ is the electric field, $\mathbf{B}$ is the magnetic field, and

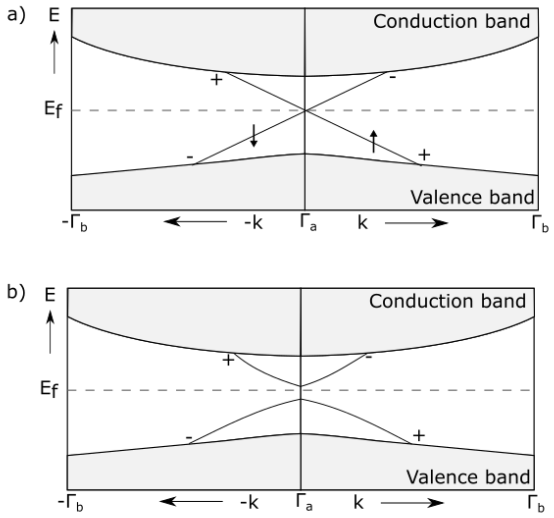

Figure 2-1. A comparison between the surface states of a topological and axion insulator. In a TI (top panel), the surface states are ungapped and can conduct spin-momentum-locked electrons. In an AI (bottom panel), a gap opens between the surface states due to the broken TR symmetry, but the sign difference caused by a band inversion remains.

e and h are the standard physical constants.

$$\Delta L_{EM}^{CS} = \theta \frac{e^2}{2\pi h} \mathbf{E} \cdot \mathbf{B} \tag{2.4}$$

The results of this Lagrangian are known as "axion electrodynamics". This offers an alternate way to define $\mathbb{Z}_2$ topological insulators, based on their magnetoelectric properties rather than their conductive surface states [12, 1]. In non-magnetoelectric materials, this axion term simply vanishes, because $\theta = 0$. In topological insulators, $\theta = \pi$ and the axion electrodynamics play a role in the electronic structure. In a TR symmetry invariant topological insulator, the resulting magnetoelectric effect will not be observable, because TR symmetry must be broken for there to be a magnetic field or a magnetic polarization. If TR symmetry is broken in a TI -like material, however, the large magnetoelectric effect should be detectable, although the conductive surface states will become gapped (Figure 2-1). Such a material is called an axion insulator.

It should also be noted that the axion electrodynamics can only affect the electron

behavior when there is a change in θ. So, they have no effect in the bulk but are significant at the surfaces, where the transition to an ordinary insulator (like vacuum) will change θ. Additionally, to have an observable magnetoelectric effect inversion symmetry must be broken, along with TR symmetry, but this I-symmetry breaking will necessarily occur at the surfaces.

The axion electrodynamics term is the same as the term used to describe a theoretical particle, the axion. Axions were proposed in 1977 as a way to resolve the "strong CP problem" in particle physics[1]. The strong CP problem is the absence of an expected symmetry breaking by the strong force in the nucleus. A term added to the Lagrangian of the strong interaction to resolve the issue leads to the axion particle as a consequence [17]. Because the physics of the axion and of the topological magnetoelectric effect are analogous, the name was applied to the TR-broken topological insulators, which can be thought of as having an axion quasiparticle [27].

Along with the quantized magnetoelectric effect, the axion term in materials should lead to a half-integer quantum Hall effect [11]. It will also have spectroscopic consequences, which often can be more easily measured. Specifically, the Faraday and Kerr rotations of polarized light will be quantized proportional to the fine-structure constant. This rotation should occur in $\mathbb{Z}_2$ TIs regardless of time-reversal symmetry, and has been experimentally observed in films of Bi_2Se_3 [21].

To create an axion insulator, one can either add magnetism to a known TI or find

[1]C refers to charge conjugation - swapping a particle with its corresponding antiparticle - and P to parity - reversing the sign of a spatial coordinate of a particle, and thus turning it into its mirror image. If a particle posseses CP symmetry, then performing these two operations in order - first flipping the charge and then the parity - will leave the particle and the laws of physics that describe it unchanged. The standard model of physics predicts that the strong interaction, which holds nuclei together, should sometimes allow violations of CP symmetry. However, so far no such violations have been observed [13]. The proposed explanation is the 1977 Peccei-Quinn theory, which describes the CP symmetry violation with a term characterized by the axion parameter θ [14]. The broken symmetry is accounted for by a particle called the axion. It was named by Frank Wilczek after a brand of laundry detergent because it "cleaned up" the strong CP problem; this won out over the other name initially proposed, the "Higglet" [15–17]. The axion is expected to be observable, and possibly a component of dark matter. There have been several claims of its detection, although none are widely accepted as definitive yet [18–20].

an intrinsic magnetic material with the right topological band structure. The former has been achieved by building a heterostructure of TI layers; several works report the expected Hall conductance in layers of magnetically doped ($(Bi,Sb)_2Te_3$) [22–24]. However, achieving a robust magnetoelectric state in heterostructures is challenging because of the usually non-homogenous distribution of magnetic ions, and the need for strong coupling between the magnetic and topological layers, so instrinsic axion insulators are a desirable next step [25, 26]. The work here focuses on how to translate the proposed physics of an intrinsic AI into a real bulk material.

An intrinsic axion insulator, like a TI, is expected to be a small bandgap insulator with heavy elements to induce strong spin-orbit coupling. Unlike TIs however, axion insulators must also contain magnetic ions. Intrinsic axion insulators can be subdivided into three categories depending on their axion coupling parameter and the symmetries they must possess; a search process will need to differentiate between these categories.

I) Topological insulators with inversion symmetry where the axion coupling $\theta = \pi$ [27]. These are the most similar to Z_2 TIs. In the absence of TR symmetry, the Z_2 invariant and surface states are protected by the inversion symmetry instead. (Although they are no longer conductive, the topological surface states must still exist.)

II) Materials where both inversion and TR symmetry are broken, and that are proximate to a topological phase (but not quite one themselves). Because both I and TR symmetries are broken, the axion coupling θ is not quantized, so it will be large but not equal to π. Although these materials do not have a Z_2 invariant, they are of interest because they are still expected to display a significantly larger ME effect than known magnetoelectric materials [8]. Because of their broken inversion symmetry, the magnetoelectric coupling will be observable in the bulk as well as the surfaces, making experimental detection much easier [9].

III) Topological insulators where the axion coupling $\theta = \pi$, and the Z_2 invariant is

protected by some symmetry other than time reversal or inversion: for example, the symmetry $S = \Theta T_{1/2}$, which is time reversal combined with a translation [28].

The materials search described here began with type II materials, but eventually encompassed all three categories.

2.2 Type II - isotropic magnetoelectric materials

The initial materials search stemmed from work by Sinisa Coh and David Vanderbilt, which considered the necessary conditions for $\mathbb{Z}_2$ TI adjacent insulators with a large isotropic magnetoelectic effect [8]. The requirement that the effect be isotropic imposes symmetry requirements on the structure of the material. These symmetry requirements were used as a starting point for the systematic search for candidate materials performed for this thesis.

Coh and Vanderbilt restricted their examination of viable crystal structures to the cubic space groups, as these are the most likely to have relatively simple structures with an isotropic ME coupling. The crystal structure of a type 2 AI must change sign under both time-reversal and inversion, in order to permit an observable magnetoelectric effect. For this effect to be isotropic, the structure must be rotationally symmetric, and for the effect to occur in the bulk as well as the surfaces, it must also be translationally symmetric. These requirements exclude all structures that are even under TR or I, or under combined symmetry operations where TR or I is followed by a proper rotation or a translation. There are 36 cubic space groups, with 308 Wyckoff orbits - sets of symmetry-related atomic positions - between them. Coh and Vanderbilt identified 62 of these Wyckoff orbits with no forbidden symmetry operations, of which 30 may have an arrangement of magnetic moments that also satisfy the symmetry criteria. Including the multiple valid magnetic arrangements on some of the Wyckoff orbits, there are a total of 44 viable structures. These 44 options have structural motifs in

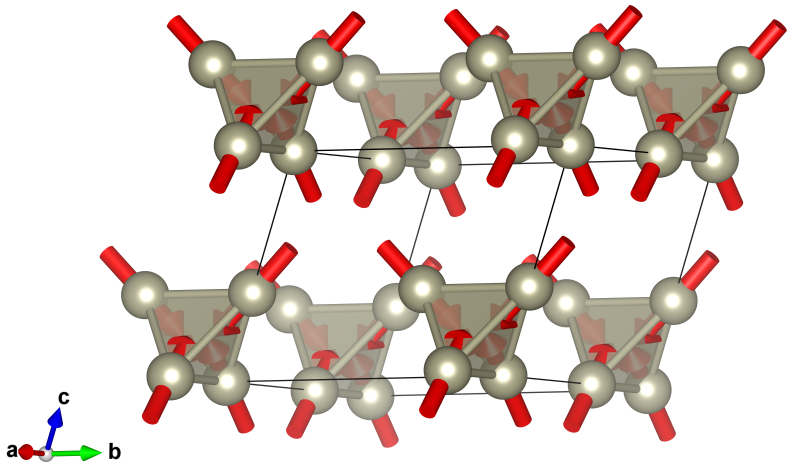

Figure 2-2. The all-in all-out spin configuration in a breathing pyrocholore. Type II AIs are expected to have this magnetic structure.

common: all are breathing pyrochlores with an all-in/all-out configuration of magnetic moments, as shown in Figure 2-2 [29].

The work done for this thesis began by searching for known materials with one of the 44 identified structures. A search of the International Crystal Structure Database (https://icsd.fiz-karlsruhe.de) was performed for each space group, and a list of materials with transition metals on the specified Wyckoff orbits was complied. Besides the symmetry requirements, candidate materials must be insulating, and must be capable of having magnetic order, so the list was narrowed down by removing any materials known to be metals, and any with only d0 or d10 transition metals, which cannot have magnetic moments. The initial list of candidates that met these criteria is given in Appendix I.

The search process for one of the 44 arrangements is described here as an example. Space group 230 with Wyckoff orbit 48g and magnetic moment Γ^{1-} is one of the identified structures. A search for materials in space group 230 with Wyckoff sequence containing "g" and with the composition including any transition metal gave 69 results

in the ICSD, including materials with ten different structure types. Of these results, fourteen materials had the transition metal on the desired Wyckoff orbit, 48g. Ten of the materials were then eliminated because they were metallic or had only d0/d10 transition metal ions, leaving four candidates in the list.

Of the 44 canonical structures, candidates were found for 35; this number dropped to 27 when metals and non-magnetic ions were removed. The next step was to select the most promising candidates from this list for computational study and synthesis. Candidates were considered more favorable if their transition metal ion was 4d or 5d, due to the stronger spin-orbit coupling these ions have. Additionally, it is desirable to start with materials belonging to a structural family with multiple suitable candidates, and which can be synthesized by standard methods. Each family of materials studied is discussed below.

2.2.1 $Re_4S_4Te_4$ and $Nb_4Se_4I_4$

$Re_4S_4Te_4$ was selected as particularly interesting because Re^{4+} is isoelectronic with Os^{5+} in $Cd_2Os_2O_7$, which is known to have an all-in/all-out magnetic order. Both had been previously reported, but had little information available on their physical properties [30–32]. Band structure calculations were performed on $Re_4S_4Te_4$ and the isostructural $Nb_4Se_4I_4$ using the Elk implementation of DFT-LDA, with a basis set of full-potential linearized augmented-plane waves plus local-orbital (FP-LAPW+LO) and a 6 x 6 x 6 k-point mesh [33]. In these calculations, $Re_4S_4Te_4$ appears to be a semi-metal with a small electron pocket; applying spin-orbit coupling splits the valence band, increasing the indirect overlap between it and the conduction band (Figure 2-3). $Nb_4Se_4I_4$ is predicted to be a metal in non-spin-polarized calculations, but becomes insulating when magnetic order and a Hubbard U are applied (Figure 2-4), a more promising result.

Both materials were synthesized in order to carry out physical properties measure-

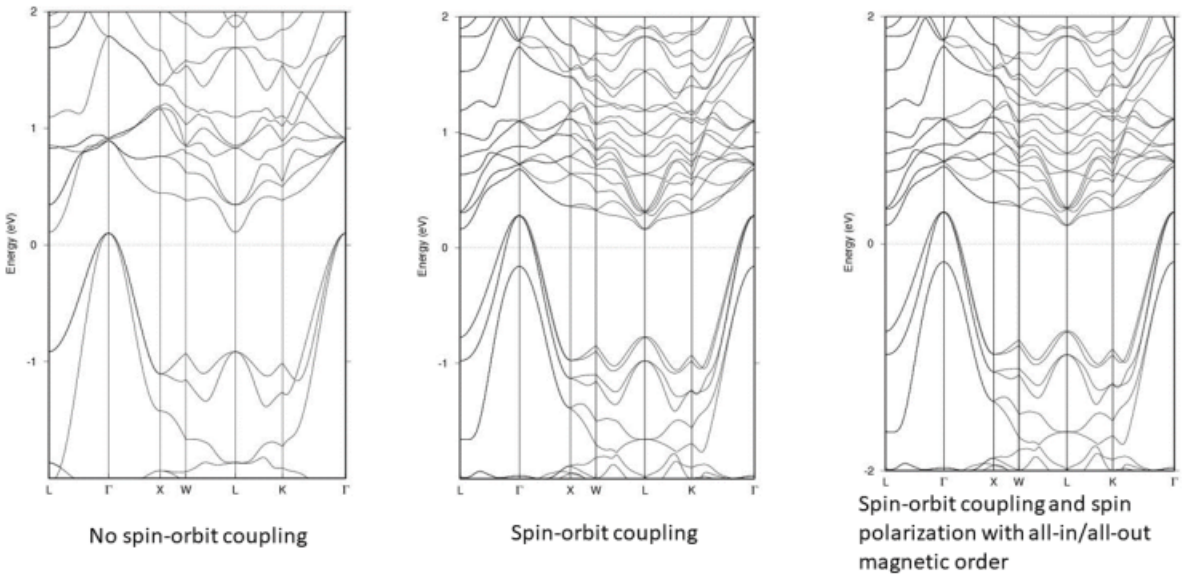

Figure 2-3. Band structure of $Re_4S_4Te_4$. DFT calculations with and without SOC and magnetic order predict a semi-metal.

ments. $Nb_4Se_4I_4$ was found to be diamagnetic, disqualifying it from being an axion insulator. However, a phase transition was discovered in heat capacity measurements that was not visible in most other characterization methods. Work was continued on $Nb_4Se_4I_4$ to examine this unusual hidden order. This research is discussed in detail in Chapter 4.

Powders of $Re_4S_4Te_4$ were synthesized from the elements by heated at 900°C for 12 hours in an evacuated quartz ampoule. Stoichiometric amounts of Re, S, and Te were ground and pressed into a 200mg pellet. Several cycles of heating were necessary to obtain the pure material. On the first cycle, the heating rate was set at 100°C per hour to avoid rapid vaporization of tellurium and sulfur. Subsequent cycles stepped directly to 900°C. The sample was reground between each cycle, and additional tellurium and sulfur were added as necessary to react with ReS_2 and Re impurities. The identity of the sample was confirmed by powder X-ray diffraction on a Bruker D8 Focus diffractometer using Cu Kα radiation and a LynxEye detector. Consistent with the literature, diffraction data from $Re_4S_4Te_4$ can be fit to the cubic

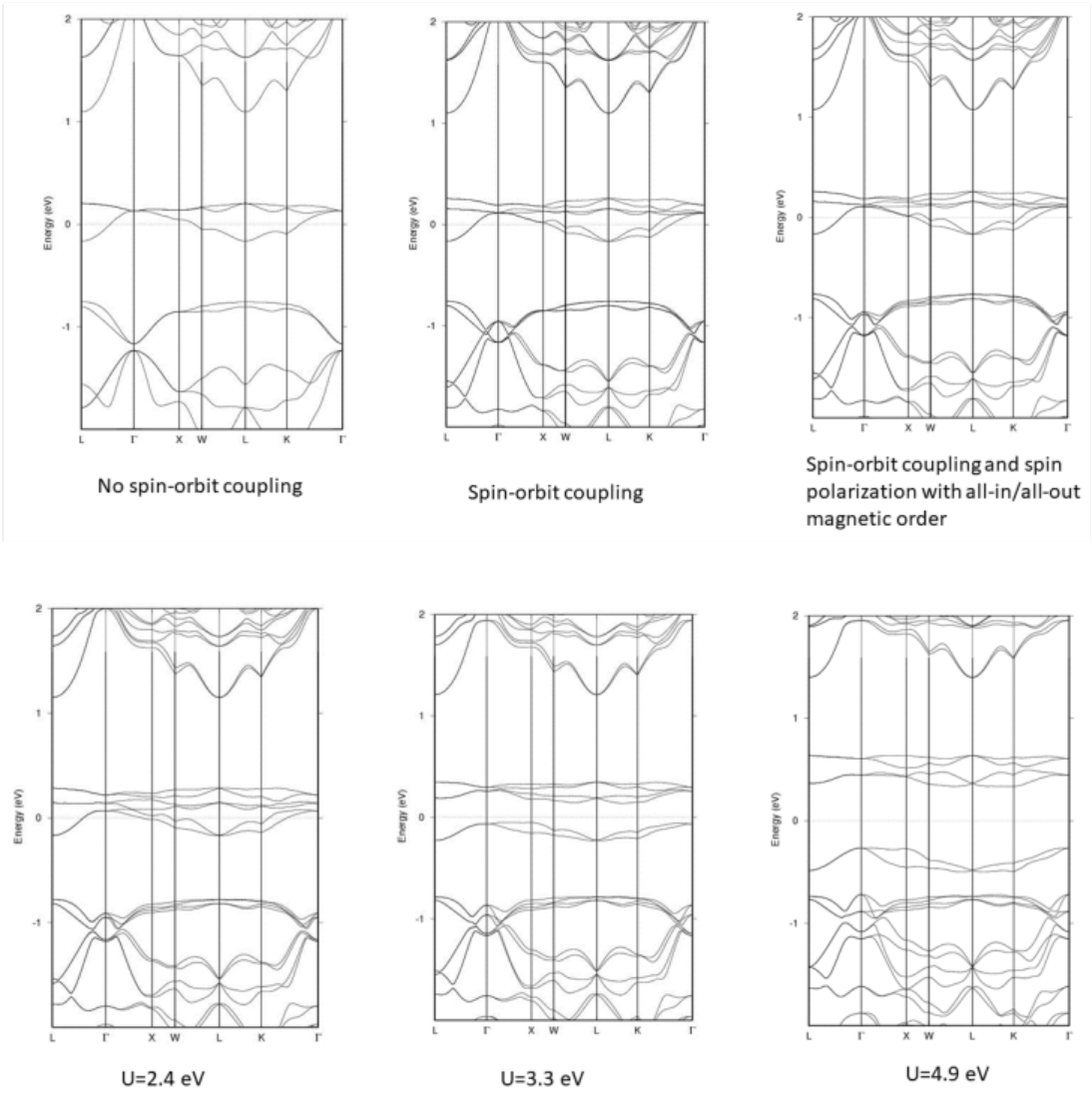

Figure 2-4. Band structure of $Nb_4Se_4I_4$. DFT calculations predict that a band gap opens when magnetic order and a Hubbard U are included. The calculations in the lower panel were all performed with SOC and an all-in/all-out magnetic order.

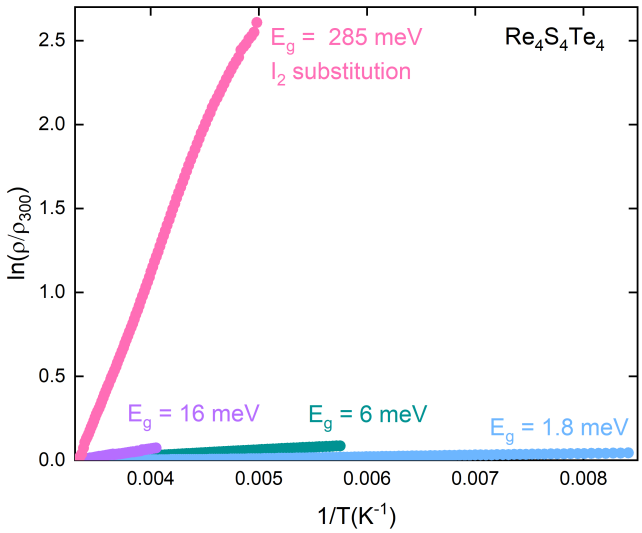

Figure 2-5. The bandgap of $Re_4S_4Te_4$ was predicted from resistivity versus temperature measurements of multiple samples. Iodine substitution ($Re_4S_4Te_{4-x}I_x$) significantly increases the gap size.

space group F-43m. The structure is a breathing pyrochlore with alternating large and small Re_4 tetrahedra.

The basic physical properties of $Re_4S_4Te_4$ were measured on a Quantum Design Physical Properties Measurement system. Resistivity was measured for three packed powder samples between T 2 - 300 K (Figure 2-6). In contrast to the computational predictions, the material appeared to be a very small bandgap semicondutor. Resistivity varied between samples but was on the order of 10^{-2} Ω·m over the full temperature range and decreased slightly with temperature. Treating $Re_4S_4Te_4$ as a semiconductor, band-gaps were estimated from the slope of ln(R/R300) vs 1/T), giving E_g = 1.8 meV, 6 meV, and 16 meV for the three samples. Magnetization versus temperature data were collected at H = 1 T (Figure 2-6). These results showed that $Re_4S_4Te_4$ is diamagnetic. The upturn at low temperatures is the background magnetization from the sample holder. The lack of magnetization is a mark against $Re_4S_4Te_4$ as an axion insulator candidate, as magnetic ions are a key feature.

Terahertz spectroscopy was attempted on $Re_4S_4Te_4$, but no transmission through

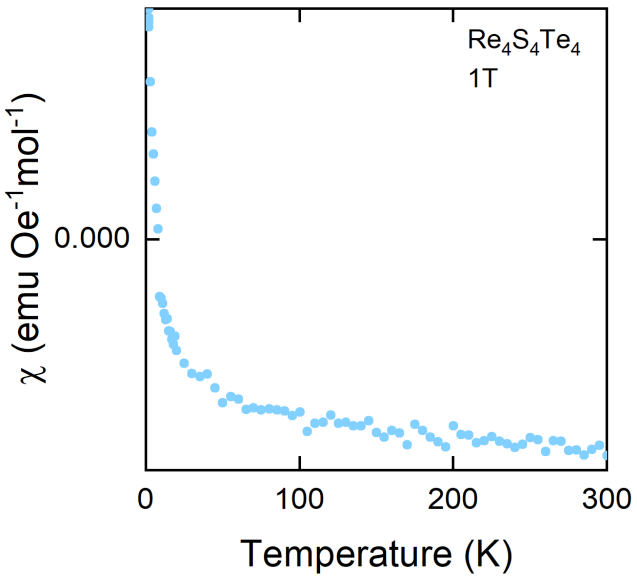

Figure 2-6. Magnetization versus temperature of $Re_4S_4Te_4$. The upturn at low temperatures is consistent with the background magnetization of the sample holder, so $Re_4S_4Te_4$ appears to be diamagnetic.

the sample could be achieved. This suggests the material has a metallic character or is a highly doped semiconductor. Due to the low magnitude of the measured resistivity, it is plausible that the gentle change with temperature derives from grain boundaries or surface oxidation on the pellets measured rather than from the bulk of the material itself. To increase the resistivity, $Re_4S_4Te_4$ was doped with iodine by substituting I_2 for a portion of the tellurium in the initial synthesis. This n-type doping was intended to raise the Fermi level, hopefully enough to have it lay in the bandgap. This appeared to successfully increase the resistivity by several orders of magnitude. For a sample with approximate composition $Re_4S_4Te_{3.5}I_{0.5}$, $R_{300K} \approx 3700\ \Omega\cdot$m and the estimated $E_g = 140$ meV.

Heat capacity measurements do not show the anomaly observed in $Nb_4Se_4I_4$. $Re_4S_4Te_4$ was thus in the work on $Nb_4Se_4I_4$ to estimate the lattice contribution to the heat capacity. Flux crystal growth of $Re_4S_4Te_4$ was also attempted, by heating for 3 weeks at 900°C in a tellurium flux, but was unsuccessful.

Attempts were also made to synthesize derivatives of $Nb_4Se_4I_4$. The analoguous materials $Nb_4S_4Br_4$, $Nb_4Se_4Br_4$, and $Nb_4S_4I_4$ have been reported, but could not be obtained in pure form [32]. Vapor transport syntheses attempted for these three materials and others of the forms $Nb_4Q_4X_4$ and $Ta_4Q_4X_4$, where Q=S, Se, and X = Cl, Br, I, were not successful, generally producing a mix of binary compounds.

2.2.2 $Pb_3M(PO_4)_3$ eulytites

Another set of materials considered were the lead eulytites $Pb_3M(PO_4)_3$ (M = V, Fe). These were selected because they belong to a large and diverse family, which has been studied for physical properties including luminescence and piezoelectricity[34]. Following a literature report, these were synthesized by standard solid state methods [35]. Starting with stoichiometric $Pb_2P_2O_7$ and Fe2O3, the M = Fe compound was made by heating the stoichiometric reactants to 800°, increasing the temperature at a rate of 50°/hr and holding for several hours at 300 and 600°C. Samples were then water-quenched from 800° and their identity was verified by powder x-ray diffraction. Syntheses of M = V were attempted by a similar method, quenching from 900 or 990°, but in PXRD the products of all attempts appeared amorphous or primarily composed of the $Pb_2P_2O_7$ starting material.

$Pb_3Fe(PO_4)_3$ was characterized by magnetization versus temperature measurements, in which it appeared paramagnetic. The resistance of the sample at room temperature was on the order of MΩ, well out of the desired range for an axion insulator candidate. Band structure calculations of either compound were not possible because of the mixed Pb/M occupancy on the 16c sites.

2.2.3 Cobaltites

A large family of materials with the CoAsS cobaltite structure met the criteria of the search. These compounds are either insulating or metallic depending on their electron

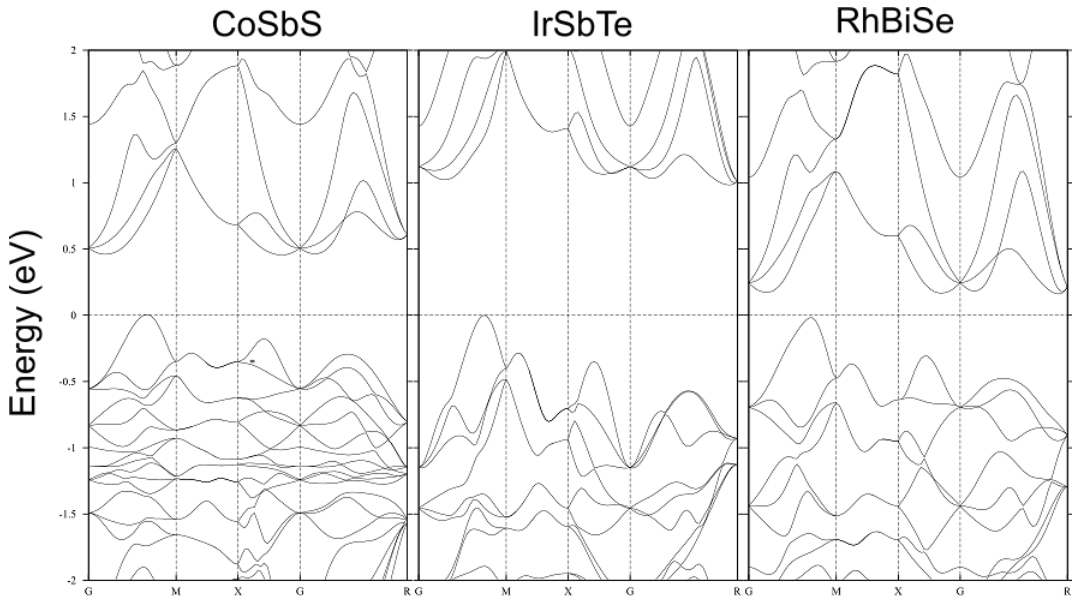

Figure 2-7. Electronic band structure calculations for three insulating cobaltite compounds.

count [36]. Band structures were computed for the insulating materials CoSbS, IrSbTe, and RhBiSe. All had wide bandgaps, and thus were not likely to be axion insulators (Figure 2-7). These calculations were performed using the Elk implementation of DFT-LDA and the Stuttgart TB-LMTO program [33, 37].

2.3 $MnBi_2Te_4$

Investigations into improved crystal growth methods for $MnBi_2Te_4$ were carried out, and powder samples were prepared and used in neutron scattering studies. $MnBi_2Te_4$ has attracted a great deal of attention recently as a magnetic topological insulator [38, 39, 28, 26]. It belongs to the third category of AIs, with its topology protected by the composite symmetry $S = \Theta T_{1/2}$. It has a septuple layer structure consisting of layers of magnetic MnTe interspersed with the topological insulator Bi_2Te_3. Below T $\approx$ 25 K, it takes on a magnetic order which is predicted to support an axion insulator state.

Preparing high-quality samples of $MnBi_2Te_4$ is a significant challenge. $MnBi_2Te_4$ is metastable at room temperature and forms within a very narrow temperature range, requiring precise control of thermal gradients during synthesis [40, 41]. Crystal growth conducted by slow cooling from a stoichiometric melt, over a stability window of ≈3 K, has been reported, producing single crystals with a maximum diameter of 200 μm [40]. Another reported slow-cooling growth yielded plate-like single crystals up to 3 mm diameter, but required careful separation of the crystals from a bulk sample chunk [42]. Additionally, the Bridgman-Stockbarger method has been used, yielding a multi-phase ingot containing single crystals of $MnBi_2Te_4$, similarly requiring careful separation [43, 28]. All of these methods result in high-quality single-crystals, but techniques that are less laborious and produce larger crystals are needed. For this thesis, flux, Bridgman-Stockbarger, and chemical vapor transport (CVT) growths were attempted, but were not successful.

Bridgman-Stockbarge growth of $MnBi_2Te_4$ was attempted using a vertical furnace. The temperature gradient of the furnace was mapped using a handheld temperature probe. Stoichiometric amounts of MnTe and Bi_2Te_3 were sealed in an evacuated quartz ampoule which was inserted into the preheated furnace attached to a vertical rod, lowered at a rate of 2mm/min (the slowest possible transport rate on this furnace) while rotating at 2 r/min around vertical axis, and then quenched by removing the sample holder rod. Growth attempts using a maximum temperature of 700°C and a 10 x 12 mm diameter quartz ampoule , with multiple trials varying final temperature and rotation rate. These produce a non-crystalline ingot of mixed $MnBi_2Te_4$ and starting material under all conditions. Lowering the maximum temperature to 620 °C resulted in large crystals of Bi_2Te_3, with a mix of phases sitting above them. Attempts to suppress the formation of Bi_2Te_3 crystals by heating at 700°C with an excess of MnTe and a narrow quartz ampoule (4 x 6 mm) resulted in a clear phase separation, with MnTe powder rising to the top of the ampoule above a Bi_2Te_3 ingot.

For flux growths, the furnace temperature was calibrated by heating an ampoule of Bi_2Te_3 to determine its melting point in the furnace used. Starting with a 1 : 5.85 ratio of MnTe : Bi_2Te_3, the mixture was melted by heating at 950°C for 12 hours, cooled at 10°C per hour to a 580°C furnace setting (estimated to actually be 590°C by the calibration), and centrifuged. No $MnBi_2Te_4$ was recovered.

Chemical vapor transport growths were attempted under a temperature gradient of 900 / 582°C. MnTe, Bi_2Te_3, and a transport agent of either $TeCl_4$ (with additional Bi to maintain stoichiometry) or I_2 were placed at the hot end of the furnace in an evacuated quartz ampoule. The temperature at the cool end of the furnace was verified with a handheld temperature probe. While both agents were able to transport all elements included to the cool zone, no $MnBi_2Te_4$ was formed. PXRD of silver deposits from the cool end of the ampoule identified Te, BiMn, and $BiMn_3$ in $TeCl_4$ growths, and Te, $MnTe_2$, Bi_4Te_5, and TeI_4 in I_2 growth. The formation of tellurium iodide suggests that $TeCl_4$ will be a better choice of transport agent if this synthesis route is pursued further.

Finally, powder samples of $MnBi_2Te_4$ were prepared, and used for a neutron scattering study in collaboration with the Broholm group at JHU [44]. $MnBi_2Te_4$ powders were synthesized by heating stoichiometric amounts of the binaries MnTe and Bi_2Te_3 as pressed pellets in evacuated quartz ampoules for 48 - 96 hours, and then quenching in air[2]. If allowed to cool slowly, only the binary starting materials are recovered. Additionally, the window of temperature stability is smaller than the temperature gradient within the box furnace, meaning that the position of the sample within the furnace affects whether $MnBi_2Te_4$ forms or not. An appropriate position was identified and a quantity of sample sufficient for neutron scattering measurements

[2]The starting materials were produced by heating the stoichiometric elements in evacuated quartz ampoules. MnTe was heated in a graphitized ampoule at 1000°C for 24 hours, cooled to 850°C, and quenched. Bi2Te3 was heated at 800°C for 24 hours. Mn powder (Alfa Aesar, 99.95%) was used as received, while Bi and Te were purified by sublimation.

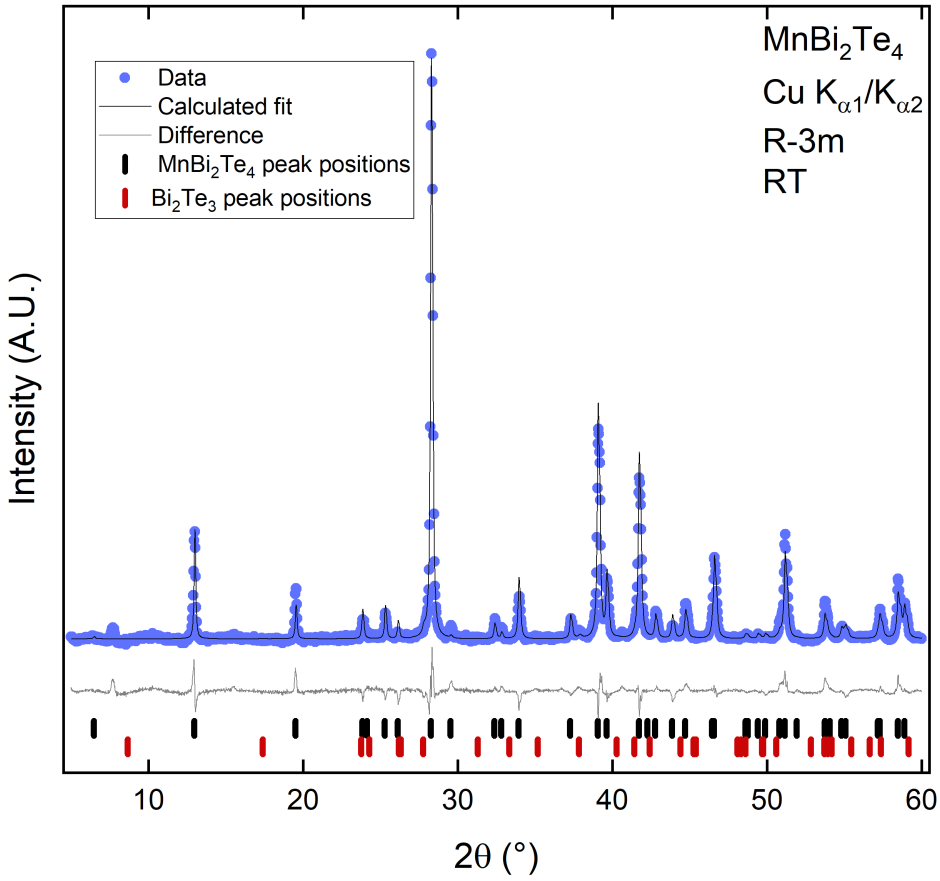

Figure 2-8. PXRD pattern of an $MnBi_2Te_4$ powder sample, showing the absence of a large Bi_2Te_3 impurity.

was prepared. The identity of the samples was confirmed by PXRD (Figure 2-8). Rietveld refinement estimated a purity of 97% for the combined samples. The neutron scattering measurements, carried out by Vincent Morano on the BT-1 and MACS instruments at the NIST Center for Neutron Research, observed the expected A-type AFM order below $T_N = 24$ K, with spin waves exhibiting competing FM and AFM interactions. Both elastic and inelastic measurements suggest a gapless excitation spectrum, apparently in contrast to previous reports [45]. Heat capacity measured at H = 0 and 9 T on a QD PPMS also points to gapless excitations.

In 2019, the flux growth of millimeter-scale crystals was reported by Yan et al, satisfying much of the need for improved crystal growth protocals. [46, 47]. Another

major difficulty with $MnBi_2Te_4$ is its electrical conductivity - all samples have displayed metallic behavior instead of the expected semiconductivity. This is likely an effect of substitutional disorder, as Mn_{Bi} and Bi_{Te} antisite defects have been observed [48]. Similar issues in Bi_2Se_3 were resolved by the inclusion of a small amount of Ca to lower the Fermi level [49]. It has now been demonstrated a similar correction could be possible in $MnBi_2Te_4$: doping with Sb allows tuning of the transport properties, and may allow access to a semiconducting state [50]. Although the synthetic issues have been reduced, and the presence of topological surface states has been thoroughly demonstrated, there is substantial evidence that the surface states are not gapped [51, 52]. Recent work has focused on thin-film $MnBi_2Te_4$, in which the quantum anomalous Hall effect has been observed despite the gapless surface, and the effects of the number of layers on the topological properties [26, 53–56].

2.4 $Y_2Ru_2O_7$

$Y_2Ru_2O_7$ is a pyrochlore containing magnetic Ru^{4+} with a transition to an antiferromagnetic state at $T_N = 77$ K. It is a candidate for a type II material, because its SOC, electron correlation U, and band gap are within the range expected for an axion insulator, meaning it may be suitable if a breathing distortion is introduced by partial oxygen substituion [57]. Although powders of $Y_2Ru_2O_7$ are straightforwardly prepared, crystal growth has not yet been achieved. Ruthenium is easily converted into volatile oxides over a large temperature range, so reaching the melting point of $Y_2Ru_2O_7$ without significant ruthenium loss is difficult. Laser-diode floating zone crystal growths were attempted, using the reported growth of Sr_2RuO_4 as a model.

$Y_2Ru_2O_7$ was synthesized from Y_2O_3 and RuO_2 at 1350°C under flowing gas for 16 hours. While below 1100°C during heating and cooling, a 90%:10% N_2:O_2 mixture was used to minimize further oxidation of RuO_2 , which was changed to 100% O_2 above this temperature. Black powders were obtained, and their identity was verified

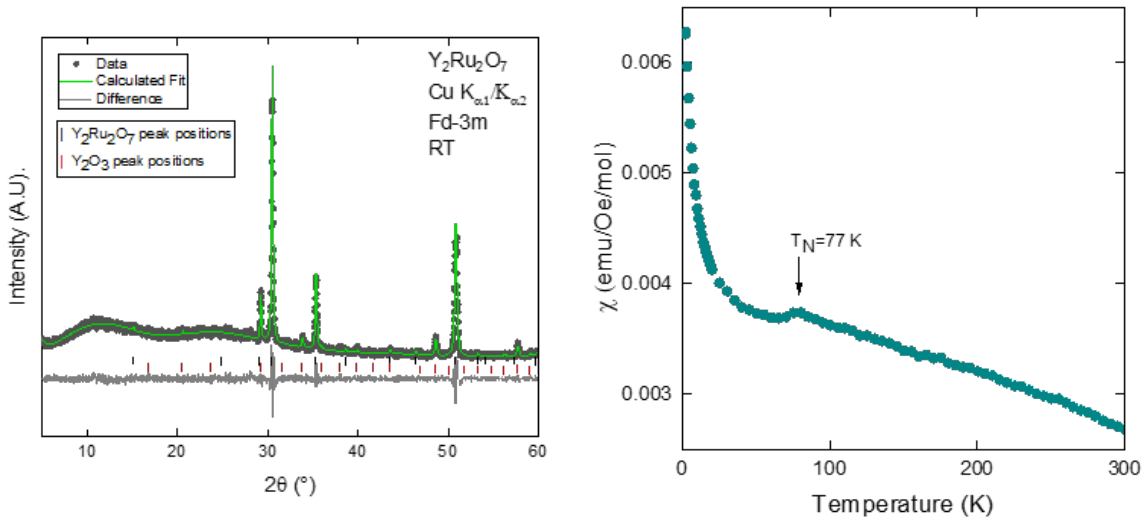

Figure 2-9. Left: PXRD pattern of a $Y_2Ru_2O_7$ powder sample. Right: magnetization versus temperature of $Y_2Ru_2O_7$, showing the expected AFM phase transition at $T_N = 77$ K.

by PXRD and magnetization versus temperature measurements (Figure 2-9). An AFM resonance below T = 77 K in terahertz spectroscopy presented another clear signature of the magnetic phase transition.

These powders were used to prepare feed and seed rods for laser diode floating zone crystal growths. Four growths were performed, varying the movement speed of the molten zone up the rod, the relative rotation directions of the two rods, and the gas under which the growth was performed (O_2 or Ar). Ruthenium loss was a major issue in all attempts, evident both from the Y_2O_3 content of the rods after a growth and the black ruthenium oxide powder that coated the furnace.

The first growth yielded a gold-colored surface layer which displayed potentially superconducting behavior in AC magnetization measurements (Figure 2-10). The growth was performed with a rectangular piece cut from a large pressed pellet as the seed rod, rather than the typical cylindrical rod used in all other cases. It was performed under O_2 gas, with no rotation. Energy-dispersive X-ray spectroscopy (EDS) in a scanning electron microscope (SEM) estimated a composition of $\approx$ 85$ Ru

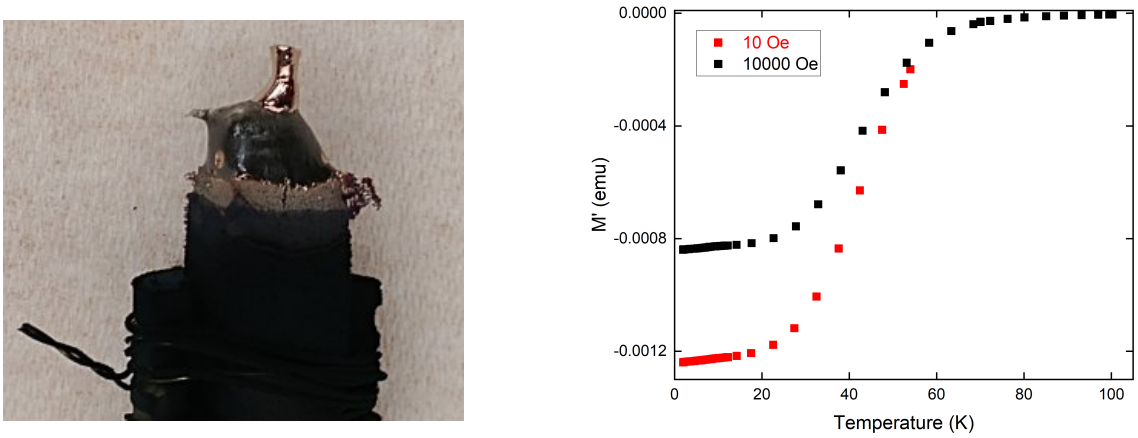

Figure 2-10. Results of a floating-zone crystal growth of $Y_2Ru_2O_7$. Left: an image of the thin layer of a gold ruthenium oxide produced on the seed rod. Right: AC magnetic susceptibility of the piece of sample with this layer, with behavior that resembles a superconducting transition.

and 15% O. However, this material could not be replicated either in the floating zone or in an electrical arc melter.

Flux growths such as the traveling solvent method are a technique that can circumvent volatilization issues like those occurring in this growth. $Y_2Ru_2O_7$ was heated in an alumina crucible at 1000° for 12 hours with the flux candidates Li_2MoO_4, $Na_2B_4O_7$, V_2O_5, B_2O_3, MoO_3 and LiCl to test their suitability. The first four reacted with $Y_2Ru_2O_7$, while MoO_3 and LiCl simply evaporated, leaving $Y_2Ru_2O_7$ and RuO_2 behind.

2.5 $EuMn_2P_2$

After the design and crystal growth in 2019 of $EuSn_2P_2$, which is an antiferromagnet below 30 K and displays topological surface states (but also bulk metallic conductivity), europium zintl phases became an area of interest in the search for topological materials [58]. The previously known material $EuMn_2P_2$ was investigated because of its antiferromagnetic order and small bandgap [59]. It possesses inversion symmetry,

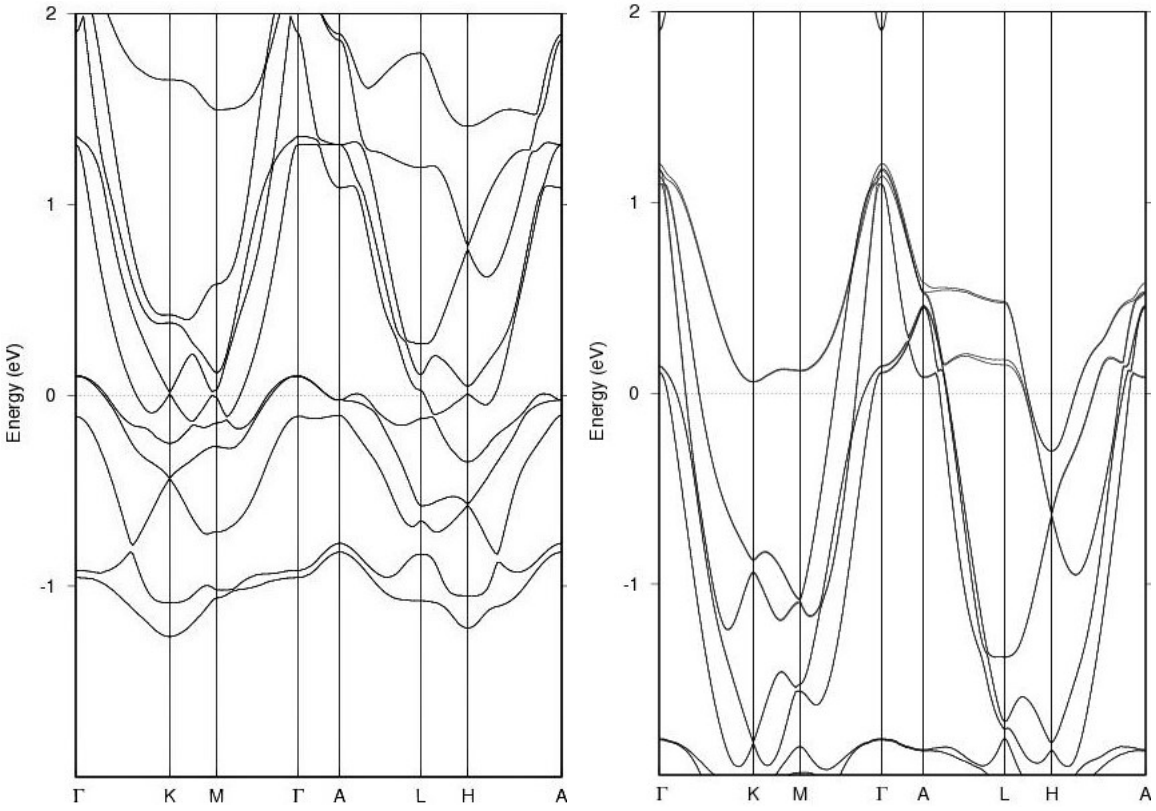

Figure 2-11. Band structure of $EuMn_2P_2$ computed with DFT. The material is predicted to be metallic regardless of the magnetism on Eu. Left: SOC, not spin-polarized. Right: SOC, U = 10 eV, c-direction magnetic field applied on Eu. It was later found that magnetic order on the Mn ions is required to open a gap.

making it a Type I candidate.

DFT calculations of $EuMn_2P_2$ predicted metallic behavior under most conditions. Figure 2-11 shows a band structure with no magnetic moments applied, and one with a c-direction moment on Eu and a large Hubbard U. The inclusion of magnetic moments on europium was not sufficient to open a gap. It was eventually determined by Nico Varnava and David Vanderbilt at Rutgers University that a gap opens only when certain manganese AFM orders are applied. As neutron data seems to indicate manganese has a weak magnetic moment in this structure, this motivates further investigation of the material.

$EuMn_2P_2$ crystals were successfully grown by the flux method. Stoichiometric

amounts of the elements were placed in a Canfield crucible along with tin pellets at an ≈1:25 Eu:Sn ratio (about 0.5 g $EuMn_2P_2$ and 4.5 g tin). This was heated in a quartz ampoule under 0.2 bar argon. Ramping up at 100°C per hour, the reaction was held for 4 hrs at 500°C and for 3 hrs at 1150°C, cooled to 1075°C at a rate of 5°C/hr, and then cooled to 800°C at a rate of 0.5°C/hr. Samples were quenched from 800°C and the tin flux was removed using a centrifuge. As the crystals were not stable to HCl, excess tin was removed manually. Well-faceted mm-scale single crystals were recoved, and were used by collaborators for transport and neutron diffraction studies [60].

Other europium zintl phases were investigated computationally, including $EuPt_2P_2$ and $EuZn_2P_2$. The platinum compound appeared metallic with no obvious way of opening a gap via magnetism, while the zinc had the opposite problem - only europium f states sat near the Fermi level, and applying magnetism was expected to open too wide a bandgap for the compound to be topological.

2.6 Additional candidates

A search of the Topological Materials Database by collaborators yielded a list of more potential candidates, by filtering the database to identify materials with inversion symmetry, potentially magnetic ions, and a non-trivial $\mathbb{Z}_2$ index [61]. The ≈ 20 materials identified were investigated in the literature by members of the McQueen group including this author. Most appeared to have large bandgaps or were synthetically impractical, but the candidate Rb_2RuO_4 was investigated further.

Rb_2RuO_4 and the isostructural K_2RuO_4 have both been reported to have antiferromagnetic transitions [62]. DFT calculations predicted a metallic structure for both. Due to the chemical instability of the reported precursors ($RbO_{1.6}$ and K_2O_2), synthesis was attempted by reacting MNO_3 (M = Rb, K) with RuO_2 under flowing oxygen, at several temperatures from 400 to 780°C, with no success.

In a follow-up literature search, we approached the problem from the opposite direction, looking first for small bandgap magnetic materials, and then working with collaborators to investigate their topology. $EuMn_2P_2$ was identified during this search, as were other rare earth compounds still under investigation. A list of candidates identified at this time is included in Appendix I.

Another search of the Topological Materials Database (by this author) looked for non-magnetic materials with an even number of band inversions, with the hope that the substitution of magnetic ions would drive an additional inversion. One of the materials found was La_2S_5Sn, which has known magnetic analogues Nd_2S_5Sn and Pr_2S_5Sn [63, 64]. Another was Ba_2Sn, with analogues Eu_2Sn and Eu_2Pb [65–67]. Both sets of materials were investigated with DFT by collaborators, and were found to be topologically trivial. However, Nd_2S_5Sn and Pr_2S_5Sn were synthesized and displayed interesting magnetic behavior. A full report on these approximate honeycomb lattice materials is given in chapter 3.

Bibliography

[1] N. P. Armitage and L. Wu, SciPost Phys. **6**, 46 (2019).

[2] A. Sekine and K. Nomura, J. Appl. Phys. **129**, 141101 (2021).

[3] M. Franz, Physics **1**, 36.

[4] I. Dzyaloshinskii, Sov. Phys. JETP **10**, 628 (1960).

[5] D. Astrov, Sov. Phys. JETP **11**, 708 (1960).

[6] C.-W. Nan, M. I. Bichurin, S. Dong, D. Viehland, and G. Srinivasan, J. Appl. Phys. **103**, 031101 (2008).

[7] A. Malashevich, S. Coh, I. Souza, and D. Vanderbilt, Phys. Rev. B **86**, 094430 (2012).

[8] S. Coh and D. Vanderbilt, Phys. Rev. B **88**, 121106 (2013).

[9] S. Coh, D. Vanderbilt, A. Malashevich, and I. Souza, Phys. Rev. B **83**, 085108 (2011).

[10] F. Hehl, Y. Obukhov, J.-P. Rivera, and H. Schmid, Physics of Condensed Matter **71**, 321 (2009).

[11] N. Varnava and D. Vanderbilt, Phys. Rev. B **98**, 245117 (2018).

[12] X.-L. Qi, T. L. Hughes, and S.-C. Zhang, Phys. Rev. B **78**, 195424 (2008).

[13] T. Mannel, Nucl. Phys. B - Proceedings Supplements **167**, 170 (2007).

[14] R. D. Peccei and H. R. Quinn, Phys. Rev. Lett. **38**, 1440 (1977).

[15] F. Wilczek, Phys. Rev. Lett. **40**, 279 (1978).

[16] S. Weinberg, Phys. Rev. Lett. **40**, 223 (1978).

[17] F. Wilczek, Phys. Rev. Lett. **58**, 1799 (1987).

[18] E. Aprile *et al.* (XENON Collaboration), Phys. Rev. D **102**, 072004 (2020).

[19] C. Beck, Physics of the Dark Universe **7-8**, 6 (2015).

[20] G. Fraser, A. Read, S. Sembay, J. Carter, and E. Schyns, Monthly Notices of the Royal Astronomical Society **445**, 2146 (2014).

[21] L. Wu, M. Salehi, N. Koirala, J. Moon, S. Oh, and N. P. Armitage, Science **354**, 1124 (2016).

[22] D. Xiao, J. Jiang, J.-H. Shin, W. Wang, F. Wang, Y.-F. Zhao, C. Liu, W. Wu, M. H. W. Chan, N. Samarth, and C.-Z. Chang, Phys. Rev. Lett. **120**, 056801 (2018).

[23] M. Mogi, M. Kawamura, A. Tsukazaki, R. Yoshimi, K. S. Takahashi, M. Kawasaki, and Y. Tokura, Science Advances **3** (2017).

[24] S. Grauer, K. M. Fijalkowski, S. Schreyeck, M. Winnerlein, K. Brunner, R. Thomale, C. Gould, and L. W. Molenkamp, Phys. Rev. Lett. **118**, 246801 (2017).

[25] V. N. Men'shov, V. V. Tugushev, S. V. Eremeev, P. M. Echenique, and E. V. Chulkov, Phys. Rev. B **88**, 224401 (2013).

[26] Y. Zhao and Q. Liu, arXiv preprint **2105.14575** (2021).

[27] A. M. Essin, J. E. Moore, and D. Vanderbilt, Phys. Rev. Lett. **102**, 146805 (2009).

[28] M. Otrokov *et al.*, Nature (London) **576**, 416 (2019).

[29] S. Coh and D. Vanderbilt, Phys. Rev. B **90**, 159903 (2014).

[30] V. Fedorov, Y. Mironov, V. Fedin, and Y. I. Mironov, J. Struct. Chem. **35**, 146 (1994).

[31] V. Fedorov, Y. Mironov, V. Fedin, H. Imoto, and T. Saito, Acta Crystallogr.

C52, 1065 (1996).

[32] M. N. Sokolov and V. P. Fedin, Coordination Chemistry Reviews **248**, 925 (2004).

[33] The Elk Code, http://elk.sourceforge.net/.

[34] P. P. Sahoo, E. Gaudin, J. Darriet, and T. Guru Row, Mater. Res. Bull. **44**, 812 (2009).

[35] R. Shpanchenko, R. Panin, J. Hadermann, C. Bougerol, E. Takayama-Muromachi, and E. Antipov, J. Solid State Chem. **178**, 3715 (2005).

[36] F. Hulliger, Nature (London) **198**, 382 (1963).

[37] O. K. Andersen, C. Arcangeli, R. W. Tank, T. Saha-Dasgupta, G. Krier, O. Jepsen, and I. Dasgupta, arXiv preprint **9804166** (1998).

[38] D. S. Lee, T.-H. Kim, C.-H. Park, C.-Y. Chung, Y. S. Lim, W.-S. Seo, and H.-H. Park, CrystEngComm **15**, 5532 (2013).

[39] M. Otrokov *et al.*, 2D Materials **4**, 025082 (2017).

[40] A. Zeugner, F. Nietschke, A. U. B. Wolter, S. Gaß, R. C. Vidal, T. R. F. Peixoto, D. Pohl, C. Damm, A. Lubk, R. Hentrich, S. K. Moser, C. Fornari, C. H. Min, S. Schatz, K. Kißner, M. Ünzelmann, M. Kaiser, F. Scaravaggi, B. Rellinghaus, K. Nielsch, C. Hess, B. Büchner, F. Reinert, H. Bentmann, O. Oeckler, T. Doert, M. Ruck, and A. Isaeva, Chemistry of Materials **31**, 2795 (2019).

[41] J. Ning, Y. Zhu, J. Kidd, Y. Guan, Y. Wang, Z. Mao, and J. Sun, npj Computational Materials **6** (2020).

[42] H. Li, S. Liu, C. Liu, J. Zhang, Y. Xu, R. Yu, Y. Wu, Y. Zhang, and S. Fan, Phys. Chem. Chem. Phys. **22**, 556 (2020).

[43] Z. S. Aliev *et al.*, J. Alloys and Compounds **789**, 443 (2019).

[44] V. Morano, V. Stewart, Y. Qiu, C. Brown, T. McQueen, and C. L. Broholm (2020), APS March Meeting.

[45] J.-Q. Yan, Q. Zhang, T. Heitmann, Z. Huang, K. Y. Chen, J.-G. Cheng, W. Wu, D. Vaknin, B. C. Sales, and R. J. McQueeney, Phys. Rev. Materials **3**, 064202 (2019).

[46] J.-Q. Yan, Q. Zhang, T. Heitmann, Z. Huang, K. Y. Chen, J.-G. Cheng, W. Wu, D. Vaknin, B. C. Sales, and R. J. McQueeney, Phys. Rev. Materials **3**, 064202 (2019).

[47] A. F. May, J. Yan, and M. A. McGuire, J. Appl. Phys. **128**, 051101 (2020).

[48] Z. Huang, M.-H. Du, J. Yan, and W. Wu, Phys. Rev. Materials **4**, 121202 (2020).

[49] Y. Hor, J. Checkelsky, D. Qu, N. Ong, and R. Cava, J. Phys. Chem. Solids **72**, 572 (2011).

[50] B. Chen *et al.*, Nature Communications **10**, 1 (2019).

[51] P. Swatek, Y. Wu, L.-L. Wang, K. Lee, B. Schrunk, J. Yan, and A. Kaminski, Phys. Rev. B **101**, 161109 (2020).

[52] Y.-J. Hao *et al.*, Phys. Rev. X **9**, 041038 (2019).

[53] D. Ovchinnikov *et al.*, Nano Letters **21**, 2544 (2021).

[54] S. Zhang *et al.*, Nano Letters **20**, 709 (2020).

[55] J. Wu, F. Liu, M. Sasase, K. Ienaga, Y. Obata, R. Yukawa, K. Horiba, H. Kumigashira, S. Okuma, T. Inoshita, and H. Hosono, Science Advances **5** (2019).

[56] C. Liu, Y. Wang, H. Li, O. Chun, Y. Li, J. Li, K. He, Y. Xu, J. Zhang, and Y. Wang, Nature Materials **19**, 1 (2020).

[57] W. Witczak-Krempa, G. Chen, Y. B. Kim, and L. Balents, Annual Review of Condensed Matter Physics **5**, 57 (2014).

[58] X. Gui *et al.*, ACS Central Science **5**, 900 (2019).

[59] A. C. Payne, A. E. Sprauve, M. M. Olmstead, S. M. Kauzlarich, J. Y. Chan, B. Reisner, and J. Lynn, J. Solid State Chem. **163**, 498 (2002).

[60] T. Berry *et al.* (2021), APS March Meeting.

[61] B. Bradlyn, L. Elcoro, J. Cano, M. G. Vergniory, Z. Wang, C. Felser, M. I. Aroyo, and B. A. Bernevig, Nature (London) **547**, 298 (2017).

[62] D. Fischer, R. Hoppe, K. Mogare, and M. Jansen, Cheminform **37** (2006).

[63] P. Jaulmes, Acta Crystallogr. Sect. B , 2283 (1974).

[64] M. Daszkiewicz, L. Gulay, and V. Shemet, Acta Crystallogr. Sect. B , 172 (2008).

[65] G. Bruzzone and E. Franceschi, J. Less Common Metals **57**, 201 (1978).

[66] O. McMasters and K. Gschneidner, J. Less Common Metals **13**, 193 (1967).

[67] A. Palenzona, P. Manfrinetti, and M. Fornasini, J. Alloys and Compounds **280**, 211 (1998).

Chapter 3

Integer vs. half-integer spin on an approximate honeycomb lattice

This work is available as a preprint under the following citation and was co-written with the following authors:

arXiv:2103.16684 (2021).

https://arxiv.org/abs/2103.16684

V. J. Stewart[1,2], J. R. Chamorro[1,2], and T. M. McQueen[1,2,3]

[1]Department of Chemistry, The Johns Hopkins University, Baltimore, Maryland 21218, USA

[2]Institute for Quantum Matter, Department of Physics and Astronomy, The Johns Hopkins University, Baltimore, Maryland 21218, USA

[3]Department of Materials Science and Engineering, The Johns Hopkins University, Baltimore, Maryland 21218, USA

3.1 Abstract

Recent interest in honeycomb lattice materials has focused on their potential to host quantum spin liquid (QSL) states. Variations in bond angles and spin allow a range of interesting behaviors on this lattice, from the predicted QSL ground state of the Kitaev model to exotic magnetic orders. Here we report the physical properties of two

compounds with rare earths on an approximate honeycomb lattice. The isostructural compounds Nd_2S_5Sn ($J = \frac{9}{2}$) and Pr_2S_5Sn ($J = 4$) permit a direct comparison of half-integer versus integer spins on this lattice. We find strikingly different magnetic properties for the two compounds. Nd_2S_5Sn orders antiferromagnetically at $T_N \approx 2.5$ K and undergoes several magnetic transitions to other ordered states under applied field. Pr_2S_5Sn displays no magnetic ordering transition above $T = 0.41$ K, and may be proximate to a spin liquid state.

3.2 Introduction

Honeycomb lattice materials have been of recent interest as quantum spin liquid (QSL) candidates, as they can host magnetically frustrated spin configurations that may have a disordered ground state [1–3]. Much of this interest has arisen due to the Kitaev model, which predicts a quantum spin liquid ground state on a honeycomb lattice with the right magnetic exchange interactions and is exactly solvable for $S = \frac{1}{2}$ [4]. Candidate materials for this Kitaev spin liquid include α-$RuCl_3$ and Ir^{4+} honeycomb iridates such as Li_2IrO_3 and Na_2IrO_3 [3, 5]. So far, all of these candidate materials have been found to magnetically order, but the unconventional magnetic orders they adopt suggest that they are adjacent to a QSL state [5–7].

Looking at honeycomb materials beyond the prototypical spin $\frac{1}{2}$ on an ideally symmetrical lattice is also valuable. The potential of larger spins to allow a QSL state has sometimes been investigated. Higher-spin models cannot be solved exactly and have weaker quantum fluctuations than $S = \frac{1}{2}$. Even so, computational studies of $S = 1$ moments with both Kitaev and Heisenberg interactions predict a spin liquid region of the phase diagram if the Heisenberg/Kitaev exchange ratio is appropriate [8–10]. $A_3Ni_2XO_6$ with X = Bi, Sb and A = Li, Na have been suggested as candidate materials [8].

Extensions to the model with a bond-dependent off-diagonal exchange term included along with Kitaev and Heisenberg terms in the Hamiltonian have been proposed to explain the magnetic order seen in Na_2IrO_3 [11]. In this material, the absence of global hexagonal or trigonal symmetry allows the Ir-O-Ir bond angles to deviate from 90°. Although this may move the material away from a Kitaev spin liquid state, it allows study of the relationship between this state and the long-range magnetic orders adopted.

Even in the absence of Kitaev interactions, spins on a honeycomb lattice can display a range of exotic magnetic states [12, 13]. Further, recent studies have shown proximal spin liquid behaviors in a number of layered rare earth compounds, including $NaYbX_2$ (X = O, Se) and $YbMgGaO_4$, as well as 3D variants including $Ce_2Zr_2O_7$ and $Pr_2Zr_2O_7$ [14–17].

Here we present magnetic and thermodynamic characterization of Nd_2S_5Sn and Pr_2S_5Sn, two isostructural materials containing an approximate honeycomb lattice of rare earth ions. They allow a direct comparison between integer (Pr^{3+}) and half-integer (Nd^{3+}) spins on this lattice. Strikingly, despite point charge calculations revealing a very similar single ion ground state, different physical properties result. The half-integer spin Nd_2S_5Sn orders antiferromagnetically at $T = 2.5$ K, and undergoes a series of transitions under applied field, adopting an intermediate magnetic order between its antiferromagnetic and ferromagnetic states. In integer-spin Pr_2S_5Sn on the other hand, no magnetic ordering is observed down to 0.41 K. These results add to our understanding of the complex magnetic behavior seen in honeycomb materials.

3.3 Methods

Nd_2S_5Sn, Pr_2S_5Sn, and a non-magnetic analogue La_2S_5Sn were prepared from stoichiometric ratios of the elements. Starting materials were sealed in quartz tubes under ≈

0.2 bar argon gas and heated at 870 K for 4 hr. After cooling and regrinding, pellets of the materials in evacuated quartz tubes were heated at a rate of 100 K/hr to 1320 K. After 12 hours, they were cooled to 870 K at a rate of 15 K/hr and water-quenched. Air-stable grey powders were obtained. Products were checked with x-ray diffraction, and if necessary additional sulfur was added to the sample and the 1320 K heating cycle was repeated.

Powder X-ray diffraction (PXRD) patterns were collected on a laboratory Bruker D8 Focus diffractometer (Cu tube, Kα_1 = 1.540596 Å, Kα_2 = 1.544493 Å) with a LynxEye detector. Structural refinements were performed with GSAS-II [18]. Structures were visualized with VESTA [19]. The crystal field splitting for a point charge model of Nd^{3+} and Pr^{3+} was computed using PYCRYSTALFIELD [20].

Magnetization data were collected on a Quantum Design Physical Property Measurement System (PPMS) using the ACMS option, and on a Quantum Design Magnetic Property Measurement System (MPMS). Magnetic susceptibility was approximated as magnetization divided by the applied magnetic field ($\chi \approx M/H$). Heat capacity data were collected on the PPMS using the semi-adiabatic method and a 1% temperature rise. For Nd_2S_5Sn, data from T = 0.12 - 3.8 K were collected using a dilution refrigerator. The heat capacity of Nd_2S_5Sn from T = 2 - 10 K was additionally measured using a long-pulse method with 30% temperature rise and analyzed using the LONGPULSEHC software package [21].

3.4 Results

3.4.1 Structure

Both compounds were refined in the space group *Pbam*, consistent with the literature. The structural parameters obtained were also consistent with previous reports [22, 23]. Refinement indicated a small $Ln_{10}OS_{14}$ (Ln = Nd, Pr) impurity in each compound

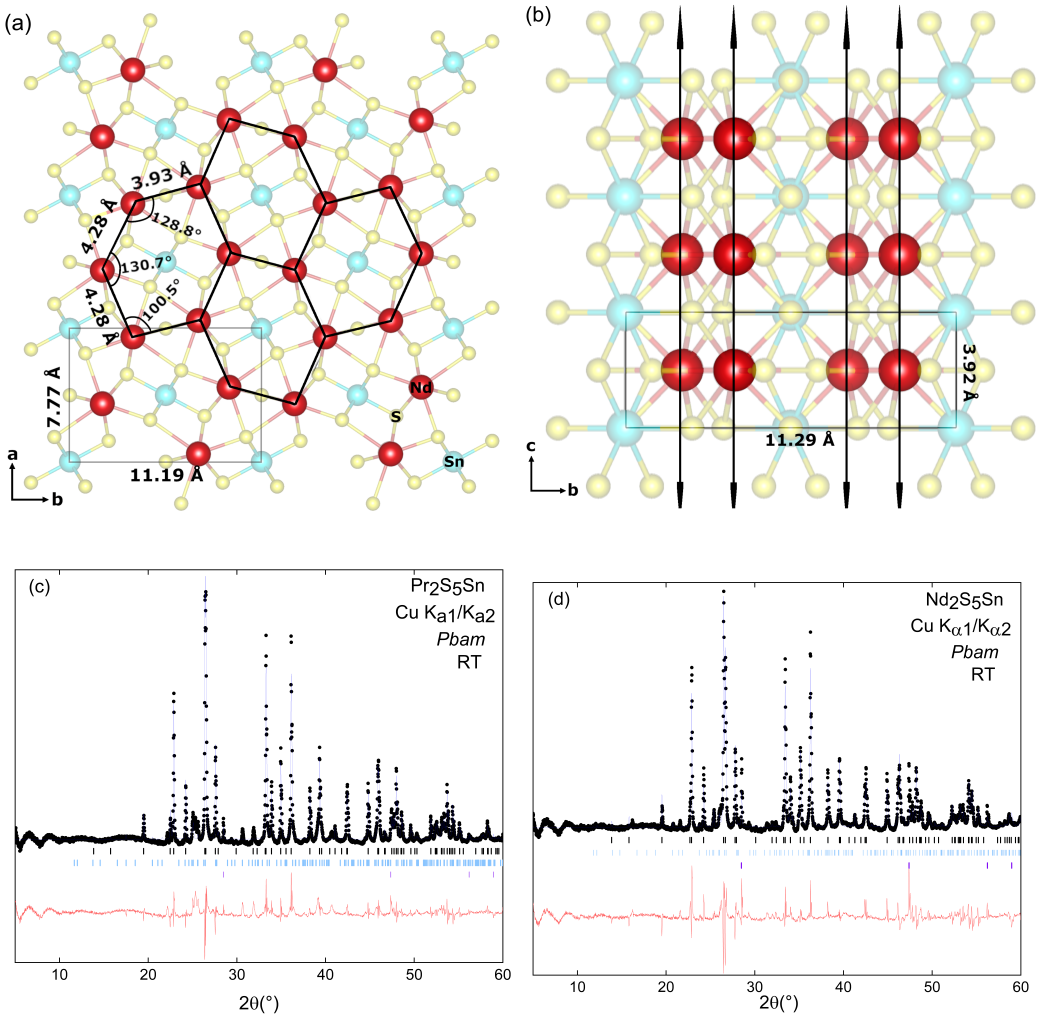

Figure 3-1. (a) The structure of Nd_2S_5Sn in the *ab* plane, showing the approximate honeycomb lattice of Nd^{3+} ions. Lattice parameters and bond lengths were estimated by refinement of powder x-ray diffraction data in space group *Pbam*. Nd atoms are shown by red spheres, Sn by cyan, and S by yellow. Structural parameters are given to their full precision in Table 3-I, as are the parameters for Pr_2S_5Sn. (b) The structure in the *bc* plane, showing the 1D columns of Nd^{3+}. (c) and (d) show the PXRD pattern (black circles), refinement (blue line), and differences (red line) for the Pr and Nd compounds. Black, light blue, and purple dashes are the *hkl* indices for Ln_2S_5Sn, $Ln_{10}OS_{14}$, and Si respectively.

(estimated weight fraction ≈ 3% in both compounds). These most likely originate from oxide impurities in the starting materials, and are expected to have minimal effect on the magnetic properties due to their small weight percentage.

The Ln^{3+} rare earth ions of Pr_2S_5Sn form an approximate honeycomb lattice in the ab plane. Each hexagon of Ln^{3+} is skewed away from equilateral, as shown in Figure 3-1(a). Along the c direction, the Ln^{3+} ions align to form a column (Figure 3-1(b)). Each rare earth is coordinated by nine sulfur atoms, while tin and sulfur are respectively octahedrally and tetrahedrally coordinated. This structure may allow Ln_2S_5Sn to behave as a pseudo-two-dimensional crystal, with each column (a 1D chain) functioning as a single unit for magnetic exchange. In both compounds, the distances between nearest-neighbor Ln^{3+} within the planes and along the columns are similar, ranging from ≈ 3.9 to 4.3 Å (Table 3-I). All Ln^{3+} atoms are connected via sulfur bonds, and the presence of this bonding between layers makes the stacking fault disorder present in some layered honeycomb materials unlikely here.

Table 3-I. Lattice parameters, Ln-Ln distances, and internal angles of the Ln_6 hexagons determined by Rietveld refinement of PXRD data. Distance and angles are given along the perimeter of a hexagon as shown in Figure 3-1(a).

	Pr_2S_5Sn	Nd_2S_5Sn
a (Å)	7.7723(3)	7.7690(3)
b (Å)	11.1942(4)	11.2329(4)
c (Å)	3.9168(1)	3.9510(1)
Ln-Ln distances (Å)	3.9337(1)	3.9384(1)
	4.2758(1)	4.2856(1)
	4.2758(1)	4.2856(1)
Ln-Ln-Ln angles (°)	128.8285(5)	129.8429(4)
	130.702(3)	130.028(2)
	100.470(2)	100.130(2)

3.4.2 Magnetization

Magnetization versus temperature measurements ($M(T)$) show a clear antiferromagnetic (AFM) phase transition for Nd_2S_5Sn at $T_N = 2.6$ K, while Pr_2S_5Sn appears

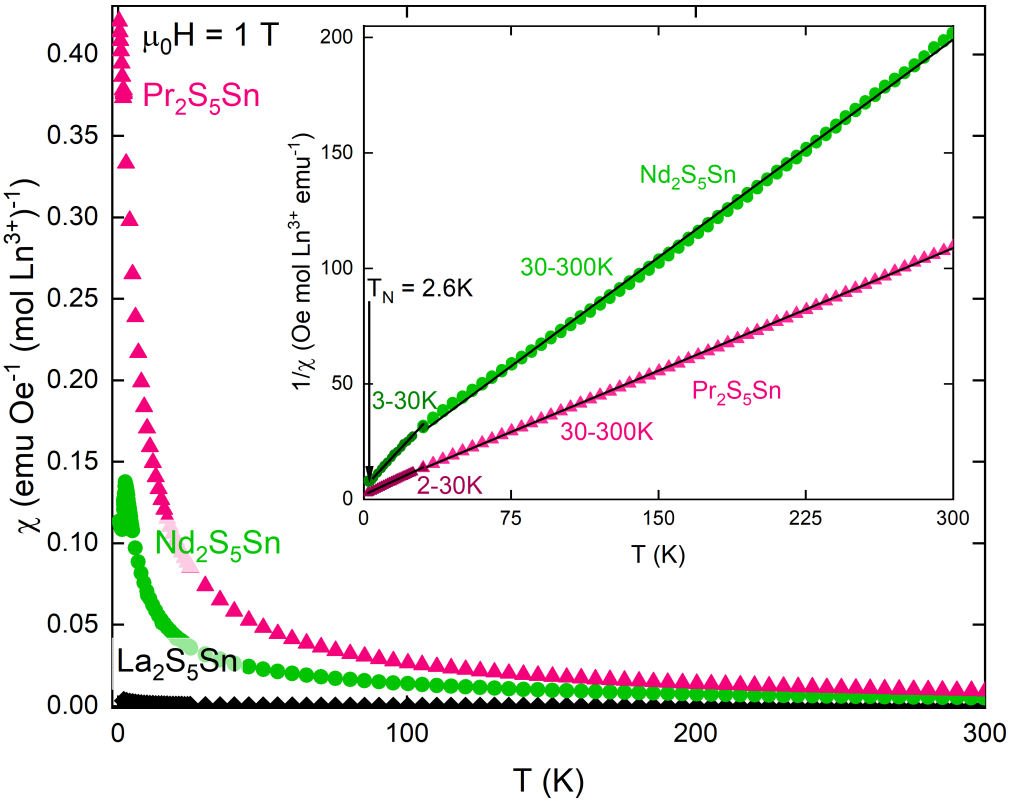

Figure 3-2. Magnetization versus temperature for Nd_2S_5Sn (green circles) and Pr_2S_5Sn (pink triangles). The inset shows Curie-Weiss fits to high and low temperature regions for each compound. The non-magnetic analog La_2S_5Sn (black diamonds) is also included for reference.

paramagnetic down to $T = 0.41$ K (Figure 3-2). Parameters obtained from Curie-Weiss fits for each compound are given in Table 3-II. Fits were performed over the range $T = 30$ - 300 K, as well as over a lower temperature range (3 - 30 K for Nd_2S_5Sn and 2 - 30 K for Pr_2S_5Sn) to avoid excited crystal fields. In all cases, best fit was achieved with no temperature-independent contribution ($\chi_0 = 0$). The room temperature susceptibility of the non-magnetic analog La_2S_5Sn was χ = - $2.06{\cdot}10^{-4}$ emu $(\text{Oe mol Ln}^{3+})^{-1}$. By comparison to the literature diamagnetic susceptibility of La^{3+} (χ_D = - $2{\cdot}10^{-5}$ emu $(\text{Oe mol Ln}^{3+})^{-1}$), this value is consistent with a negligible χ_0 [24].

The estimated Weiss temperatures θ_w (given in Table 3-II) are negative over both temperature ranges, indicating that antiferromagnetic interactions are dominant. Also

Table 3-II. Parameters obtained from Curie-Weiss analysis of Nd_2S_5Sn and Pr_2S_5Sn magnetization data. Low temperature (LT) and high temperature (HT) ranges were fitted separately. The units of the Curie constant c are $\mathrm{emu\,K\,(Oe\,mol\,Ln^{3+})^{-1}}$

	Pr LT	Pr HT	Nd LT	Nd HT
Range (K)	2-30	30-300	3-30	30-300
c	2.529(4)	2.825(1)	1.093(7)	1.589(3)
θ (K)	-4.7(1)	-7.3(8)	-5.3(5)	-16(5)
p_{eff} (μ_B)	4.49(2)	4.75(1)	2.96(2)	3.57(1)

for both ranges, the magnitude of θ_w is larger for the Nd compound, meaning that the interaction strength is larger than in the Pr. The effective magnetic moments calculated from the Curie constant are somewhat higher than the free-ion moment for Pr (3.58 μ_B), and lower than the free-ion moment for Nb (3.62 μ_B).

Crystal field splitting computed from the point charge model offer an explanation for the large moment of Pr (Figure 3-3). Nd^{3+} ($J = \frac{9}{2}$) splits into five Kramers doublets, while $Pr^{3+}(J = 4)$ splits into nine singlet states. In Pr^{3+}, the energy gap between the two lowest states is only 0.27 meV ($\approx$ 2.6 K). Due to this low energy barrier, these states may act as a "pseudo-doublet", allowing an effective $J = \frac{1}{2}$ and providing the unpaired spins necessary for the paramagnetic behavior of Pr_2S_5Sn.

The influence of these crystal field levels means that the higher-temperature Curie-Weiss fits are likely to be unreliable. However, they are included for the sake of comparison. The lower-temperature fits, in which $p_{eff} = 4.49(2)$ for Pr and $p_{eff} = 2.96(2)$ for Nd, can additionally be compared to the low-temperature moments for the Pr and Nd pyrochlores, which are also magnetically frustrated and have properties significantly influenced by their crystal field states: $Pr_2Pb_2O_7$ ($p_{eff} = 2.53(1)\ \mu_B$), $Pr_2Zr_2O_7$ ($p_{eff} = 2.5(1)\ \mu_B$), $Pr_2Sn_2O_7$ ($p_{eff} = 2.6\ \mu_B$), $Nd_2Pb_2O_7$ ($p_{eff} = 2.55(7)\ \mu_B$), $Nd_2Zr_2O_7$ ($p_{eff} = 2.543(2)\ \mu_B$), and $Nd_2Sn_2O_7$ ($p_{eff} = 2.63(3)\ \mu_B$ [25–30].

To investigate possible ordering in Pr_2S_5Sn at $T < 2$ K, *M(T)* and magnetization

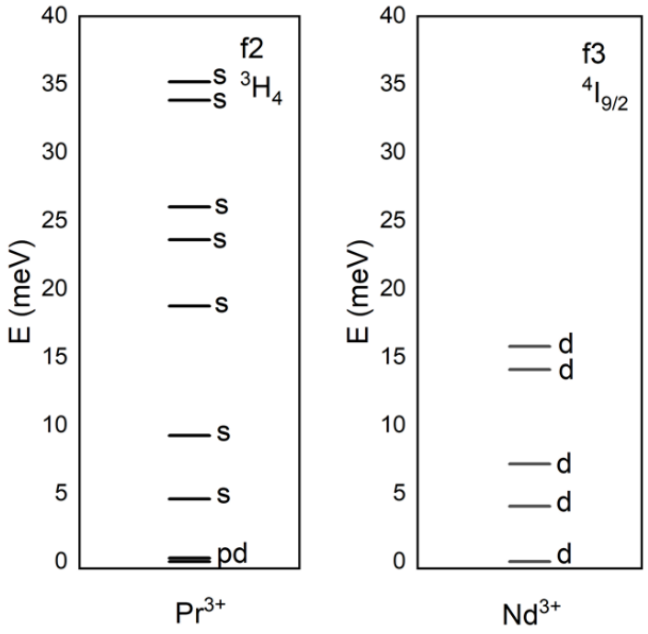

Figure 3-3. Computed single-ion crystal field levels for Pr^{3+} and Nd^{3+}. *s* indicates a singlet state, *d* a doublet, and *pd* a "pseudo-doublet". The low-energy pseudo-doublet of Pr^{3+} can explain its paramagnetic behavior.

versus field (*M(H)*) measurements were performed in a ^{3}He system (Figure 3-4). No evidence of magnetic ordering was found down to T = 0.41 K, either in *M(T)* or *M(H)* at any field. We thus conclude that Pr_2S_5Sn remains paramagnetic for T > 0.41 K. The *M(H)* curves approach field saturation as expected for a paramagnet at low temperatures, but do not appear to fully saturate in the $\mu_0 H = 7$ T range measured.

To look more closely at the observed phase transition in Nd_2S_5Sn, *M(H)* data were collected at temperatures between 0.45 and 6 K (Figure 3-5). Data points with temperature or sample center position values outside of two standard deviations are excluded from the figure. No hysteresis was observed. Derivatives of the *M(H)* curves allow clear visualization of the features of this data. At T = 3 K and above, as expected, the M versus H curves are smooth and featureless, consistent with the absence of the phase transition at these temperatures.

At lower temperatures, three distinct peaks are present in the derivative: one near 0.25 T, one near 2.2 T, and one broad peak near 4 T. These peaks decrease in intensity

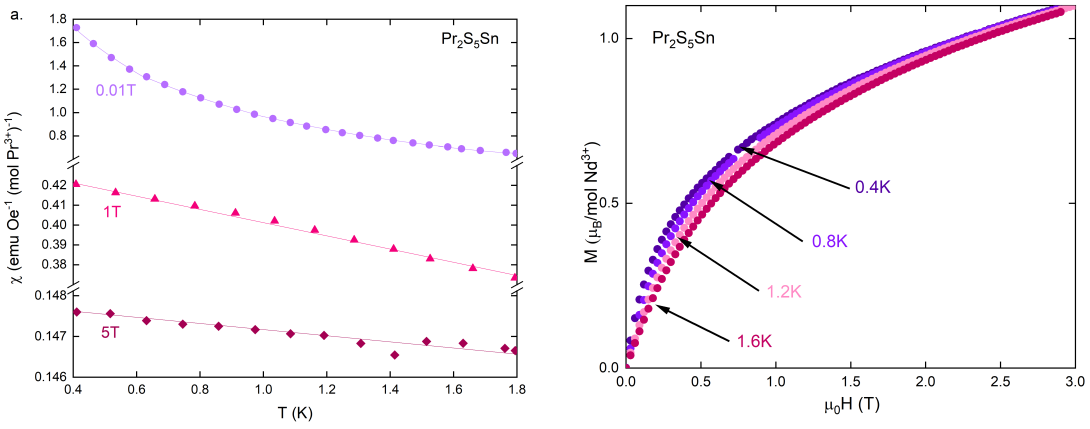

Figure 3-4. (a) Magnetization versus temperature for Pr_2S_5Sn, measured from $T = 0.4$ - 1.8 K in a ^{3}He system. Each of the three fields measured is plotted on a different scale to clearly show change versus temperature. Lines are to guide the eye. No ordering transition was observed. (b) Magnetization versus field for Pr_2S_5Sn.

and shift to lower field as temperature is raised. By 2 K, the 0.25 and 2.2 T peaks are not discernable, and the derivative curve appears to have one broad hump centered near 3 T. This suggests that the loss of anti-ferromagnetic order with increasing field occurs in three steps, with two intermediate states between full AFM order and full alignment with the applied field. The energy difference between the steps decreases with higher temperature.

3.4.3 Heat Capacity

Heat capacity measurements corroborate the magnetization data (Figure 3-6(a)). For Pr_2S_5Sn, there is a weak divergence of C/T as $T \to 0$, with no evidence of a phase transition. For Nd_2S_5Sn, a peak is observed at $T = 2.4$ K. Poor fitting of temperature curves below ≈ 6 K by the semi-adiabatic pulse method suggested a first-order phase transition, so a long-pulse technique was used for the low temperature heat capacity. The long-pulse measurements were of larger magnitude near the peak at $T = 2$ K but were in good agreement with the short-pulse data above the peak temperature, consistent with the phase transition being first-order. Additional short-pulse data

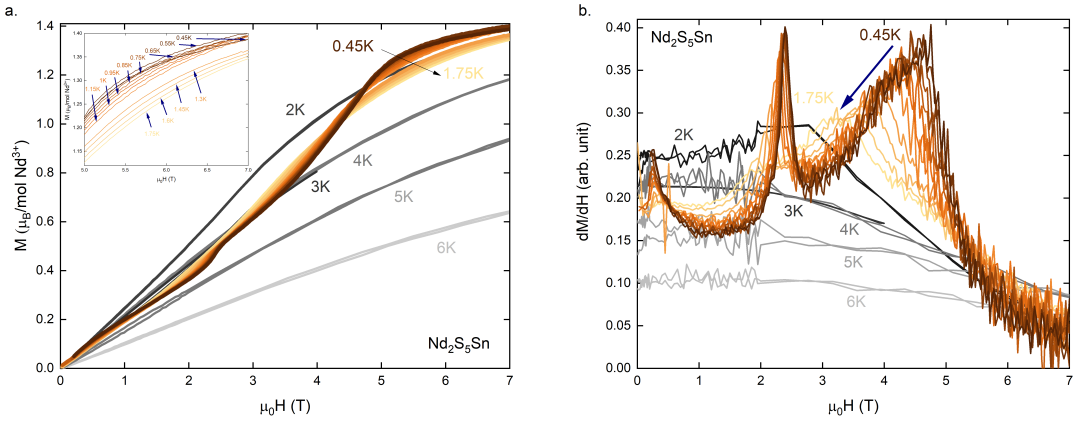

Figure 3-5. (a) Magnetization versus field for Nd_2S_5Sn at temperatures from $T = 0.45$ - 6 K. The inset shows the temperature spacing in the $\mu_0 H = 5$ - 7 T region. No hysteresis was observed in field sweeps. (b) Derivative of Nd_2S_5Sn magnetization vs field, showing three distinct peaks at temperatures below 2 K.

collected down to $T = 0.12$ K with a dilution refrigerator is truncated at 1.8 K to avoid the first-order peak.

The phonon heat capacity, estimated from the non-magnetic analogue La_2S_5Sn, was subtracted to find the magnetic contribution, C_m (Figure 3-6(a) inset). The upturn at low temperature is due to the nuclear specific heat. The magnetic entropy was calculated by integrating C_m/T (Figure 3-6(b)). For the Nd compound, entropy passes $\Delta S = R\ln 2$ near 5 K, which is sensible given its doublet ground state. It briefly plateaus, and then rises to $\Delta S = R\ln 3$ by 100 K. This is qualitatively consistent but somewhat less than expected from the point charge model, suggesting that the second excited doublet state is somewhat higher in energy than predicted. For Pr, the entropy reaches $\Delta S = R\ln 2$ around 35 K before plateauing, suggesting that only the two lowest-lying energy levels are accessible. The gradual further increase in entropy up to 50 K is qualitatively consistent with expectations and suggests that the energy gap to the third singlet state is again larger than predicted by the crystal field splitting model. Above $\approx$ 100 K for the Nd compound and $\approx$ 50 K for the Pr, the small magnitude of the magnetic heat capacity compared to the subtracted phonon

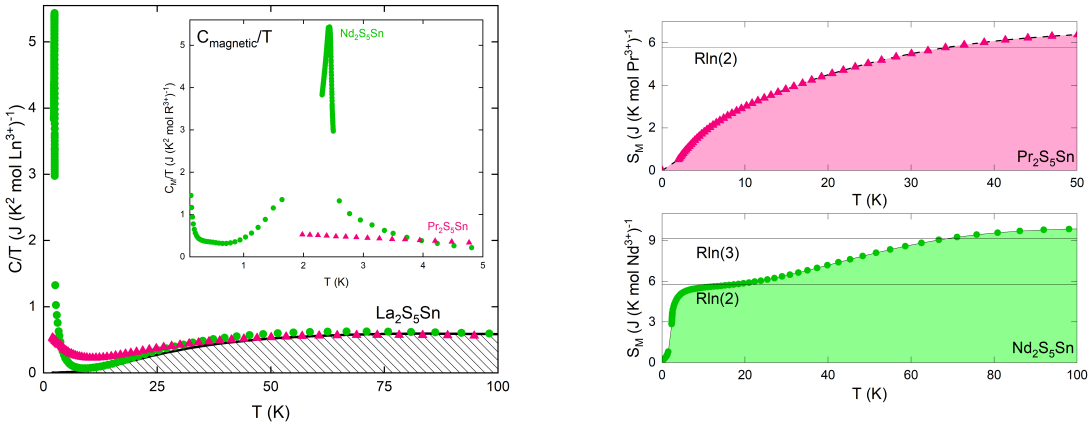

Figure 3-6. (a) Heat capacity over temperature (C/T) of La_2S_5Sn, Nd_2S_5Sn, and Pr_2S_5Sn. The inset shows the magnetic heat capacity of Nd_2S_5Sn and Pr_2S_5Sn, with the estimated phonon heat capacity subtracted. (b) Magnetic entropy of Nd_2S_5Sn (top, green) and Pr_2S_5Sn (bottom, pink), computed by integration of C_M/T.

contribution makes the computed entropy unreliable.

The heat capacity of both compounds was also measured under magnetic field (Figure 3-7). For Nd_2S_5Sn, the $T = 2.4$ K peak is suppressed with field as expected, since the presence of a large magnetic field disrupts antiferromagnetic ordering. The peak gradually decreases in magnitude from $\mu_0 H = 0$ to 3 T, and seems to disappear completely between $\mu_0 H = 3$ and 5 T. This change is visible in the magnetic entropy of these field measurements (Figure 3-8), which drops below the Rln2 plateau at and above $\mu_0 H = 3$ T, suggesting that some magnetic states are no longer frozen out or that higher energy states have become inaccessible. This change between $\mu_0 H = 1$ and 3 T may correspond to the sharp peak in dM/dH near 2.2 T. Additionally, the flattening of the heat capacity peak at 2.4 K with increasing field, and its disappearance by $\mu_0 H = 5$ T, is in agreement with the broad dM/dH peak between 3 and 5 T.

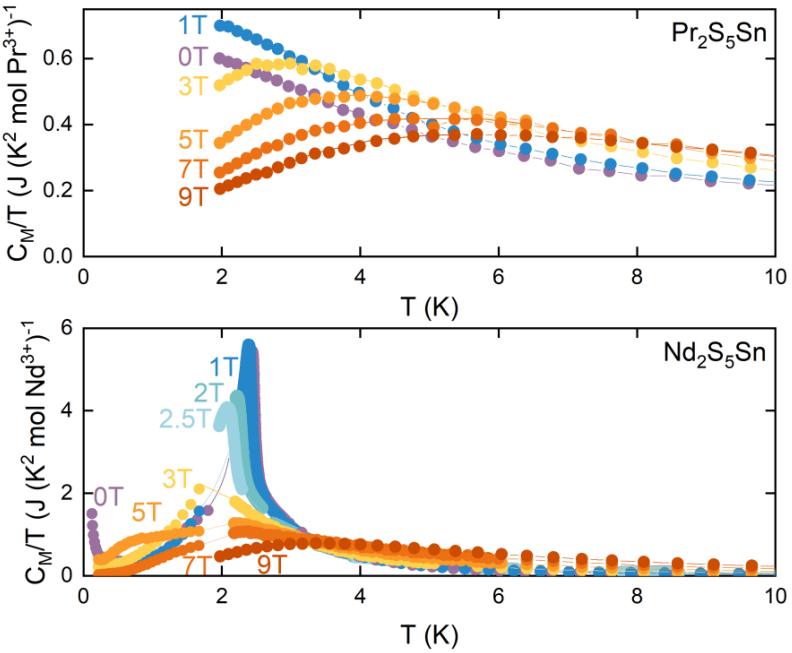

Figure 3-7. Magnetic heat capacity (as C_M/T) of Pr_2S_5Sn and Nd_2S_5Sn under applied magnetic fields. Lines are to guide the eye.

3.5 Discussion

Both our magnetic and thermodynamic measurements make it clear that although they are isostructural, the properties of Pr_2S_5Sn and Nd_2S_5Sn are quite distinct. The integer-spin Pr compound is paramagnetic down to at least $T = 0.41$ K, while the half-integer Nd compound undergoes an anti-ferromagnetic ordering transition near $T = 2.5$ K. Besides this most obvious change, we observe that although the two compounds have nearly the same Weiss temperature (θ_w) in Curie-Weiss fits below 30 K, over the higher temperature range their θ_w values differ significantly. The crystal field splitting for a point charge model of Nd^{3+} and Pr^{3+} helps explain why. The gap between the lowest-lying states (the doublet in Nd and the "pseudo-doublet" in Pr) is large compared to the temperature at 30 K. While both ions effectively have a single doublet state primarily populated, the interaction strengths of the spins in this state may be similar. At higher temperatures where other energy states are accessible, the

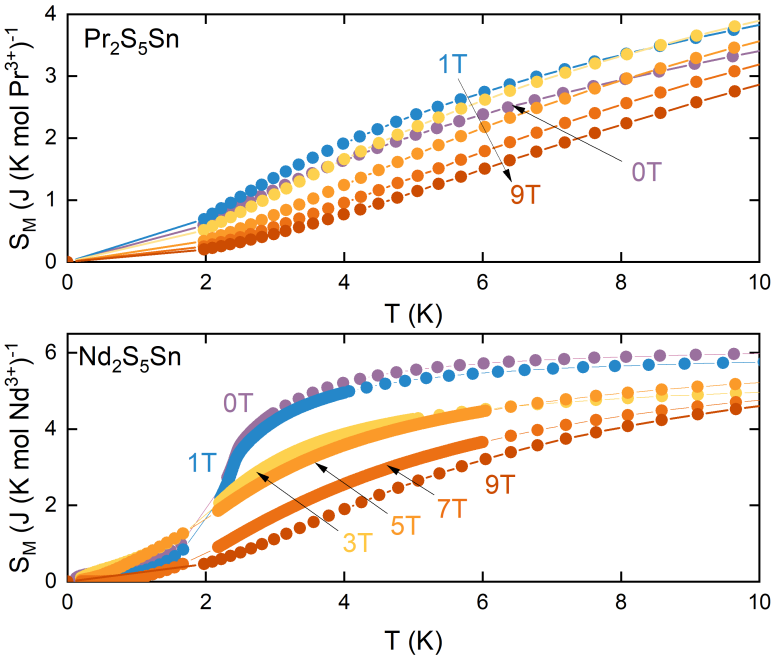

Figure 3-8. Magnetic entropy of Pr_2S_5Sn and Nd_2S_5Sn under applied magnetic field, computed by integration of C_M/T. Lines are to guide the eye.

differences between the two compounds allow the antiferromagnetic exchange in the Nd to become stronger than that of the Pr.

A magnetic phase diagram for Nd_2S_5Sn can be constructed from the *M(T)* and heat capacity under field results (Figure 3-9). From the MvH, we observed that the loss of the antiferromagnetic phase with field occurs in three stages, with the field distance between these stages shrinking at higher temperatures. The two higher-field transitions merge together by about $T = 2$ K, shown in the meeting of the phase boundaries in the diagram. The remaining transition occurs at much lower field (≈0.25 T near 1 K), indicating a less energetically difficult change in the magnetic order. Data near $T = 2.5$ K at low fields is limited, and further study is need to accurately determine the intersection of the four phases in this region.

How is the magnetic order changing at these metamagnetic transitions? Presumably above the highest field transition, the spins are fully aligned with the applied field,

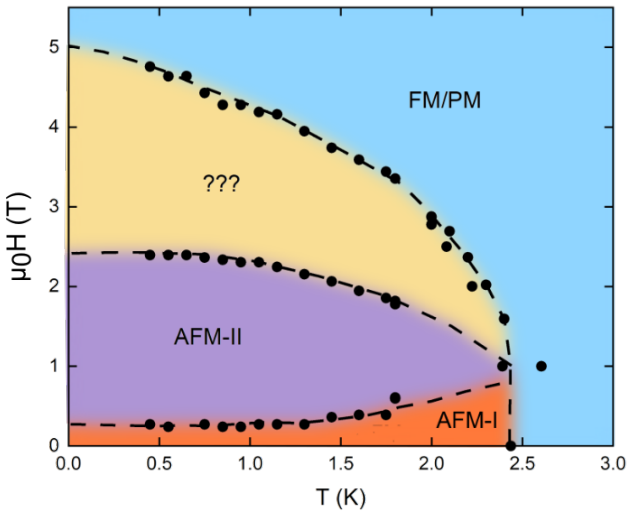

Figure 3-9. Magnetic phase diagram of Nd_2S_5Sn, estimated from magnetization and heat capacity measurements.

behaving as they would in a ferromagnet. Below this, the specifics of the magnetic order are unknown. The lowest field change may be a spin-flop transition, with spins reorienting to lie parallel to the applied field. In this case, we have one antiferromagnetic ground state and a second intermediate state before all spins align with the field, which is not entirely uncommon in anisotropic antiferromagnets [31–34]. The frustration parameter ($f = |\frac{\theta_w}{T_N}|$) of Nd_2S_5Sn is ≈ 2, relatively low, so the ground state may be a Néel antiferromagnet. Then at the second transition with field, a subset of the spins may flip along the easy axis, resulting in a magnetic order such as a stripy or zigzag arrangement. Finally, at high enough fields the remaining spins flip to give a ferromagnetic arrangement. However, further study is required to understand the specific antiferromagnetic orders present. The easy axis is unknown, as the material has only been measured in powder form, and the large deviation of the lattice from equilateral hexagons may lead to more complicated anisotropic effects.

For Pr_2S_5Sn, the lack of observed magnetic ordering raises the question of whether it has spin liquid character. Power-law fitting of the field-dependent C_m/T versus T did not match the scaling relationship observed in other frustrated spin $\frac{1}{2}$ materials

[35]. Additionally, when performing the Curie-Weiss fits, a linear fit was best achieved with the temperature-independent susceptibility χ_0 equal to zero, in contrast to many candidate QSL materials [1]. At the same time, the behavior is similar to that observed in QSL candidates based on Pr, such as $Pr_2Pb_2O_7$. Further work should clarify the behavior of this material.

3.6 Conclusion

We have investigated the physical properties of the isostructural approximate honeycomb compounds Pr_2S_5Sn and Nd_2S_5Sn, finding that the Pr compound displays no magnetic ordering down to 0.41 K, and that the Nd undergoes antiferromagnetic ordering near $T = 2.5$ K. These materials may be usefully compared to the lead pyrochlores $Pr_2Pb_2O_7$ and $Nd_2Pb_2O_7$. In these, the Pr material shows no order to 0.4 K but has a spin ice like specific heat anomaly at 1.2 K, which the Nd analog seems to adopt long-range magnetic order at 0.41 K [25]. The similar material $Pr_2Zr_2O_7$ does not order above 0.2 K and has excitations consistent with a quantum spin system; like Pr_2S_5Sn, it has a non-Kramers doublet ground state [17, 26]. Pr_2S_5Sn lacks order at low temperatures and the minimum frustration parameter $f = 4.7$ K / 0.41 K = 11 is greater than 10, suggesting the presence of magnetic frustration. Understanding how this frustration occurs on the geometry of this approximate honeycomb is of interest. Nd_2S_5Sn displays a series of magnetic transitions under applied field and seems to adopt an intermediate magnetic order between its AFM and FM states. Neutron scattering measurements on this compound to determine the magnetic order, and lower-temperature characterization of Pr_2S_5Sn, would allow us to better understand these materials.

3.7 Acknowledgments

This work was supported as part of the Institute for Quantum Matter, and Energy Frontier Research Center funded by the U.S. Department of Energy, Office of Science, Office of Basic Energy Sciences, under Award DE-SC0019331. The ^{3}He MPMS was funded by the National Science Foundation, Division of Materials Research, Major Research Instrumentation Program, under Award 1828490.

Bibliography

[1] L. Balents, Nature **464**, 199 (2010).

[2] C. Broholm, R. J. Cava, S. A. Kivelson, D. G. Nocera, M. R. Norman, and T. Senthil, Science **367** (2020).

[3] J. R. Chamorro, T. M. McQueen, and T. T. Tran, Chem. Rev. **121**, 2898 (2021).

[4] A. Kitaev, Ann. Phys. **321** (2006).

[5] J. A. Sears, M. Songvilay, K. W. Plumb, J. P. Clancy, Y. Qiu, Y. Zhao, D. Parshall, and Y.-J. Kim, Phys. Rev. B **91**, 144420 (2015).

[6] J. Chaloupka, G. Jackeli, and G. Khaliullin, Phys. Rev. Lett. **105**, 027204 (2010).

[7] Y. Singh, S. Manni, J. Reuther, T. Berlijn, R. Thomale, W. Ku, S. Trebst, and P. Gegenwart, Phys. Rev. Lett. **108**, 127203 (2012).

[8] P. P. Stavropoulos, D. Pereira, and H.-Y. Kee, Phys. Rev. Lett. **123**, 037203 (2019).

[9] X.-Y. Dong and D. N. Sheng, Phys. Rev. B **102**, 121102(R) (2020).

[10] P. H. Y. Li, R. F. Bishop, and C. E. Campbell, J. Phys.: Conf. Ser. **702**, 021001 (2016).

[11] J. G. Rau, E. K.-H. Lee, and H.-Y. Kee, Phys. Rev. Lett. **112**, 077204 (2014).

[12] G. N. Rao, R. Sankar, I. P. Muthuselvam, and F. C. Chou, J. Magn. Magn. Mater. **370**, 13 (2014).

[13] J. W. F. Venderbos, M. Daghofer, J. van den Brink, and S. Kumar, Phys. Rev.

Lett. **107**, 076405 (2011).

[14] M. M. Bordelon, C. Liu, L. Posthuma, P. M. Sarte, N. P. Butch, D. M. Pajerowski, A. Banerjee, L. Balents, and S. D. Wilson, Phys. Rev. B **101**, 224427 (2020).

[15] Y. Li, G. Chen, W. Tong, L. Pi, J. Liu, Z. Yang, X. Wang, and Q. Zhang, Phys. Rev. Lett. **115**, 167203 (2015).

[16] J. Gaudet, E. M. Smith, J. Dudemaine, J. Beare, C. R. C. Buhariwalla, N. P. Butch, M. B. Stone, A. I. Kolesnikov, G. Xu, D. R. Yahne, K. A. Ross, C. A. Marjerrison, J. D. Garrett, G. M. Luke, A. D. Bianchi, and B. D. Gaulin, Phys. Rev. Lett. **122**, 187201 (2019).

[17] J.-J. Wen, S. M. Koohpayeh, K. A. Ross, B. A. Trump, T. M. McQueen, K. Kimura, S. Nakatsuji, Y. Qiu, D. M. Pajerowski, J. R. D. Copley, and C. L. Broholm, Phys. Rev. Lett. **118**, 107206 (2017).

[18] B. Toby and R. von Dreele, J. Appl. Crystallogr. **46**, 544 (2013).

[19] K. Momma and F. Izumi, J. Appl. Crystallogr. **44**, 1272 (2011).

[20] A. Scheie, arXiv preprint **2006.15151** (2020).

[21] A. Scheie, J. Low Temp. Phys. **193**, 60 (2018).

[22] P. Jaulmes, Acta Crystallogr. Sect. B , 2283 (1974).

[23] M. Daszkiewicz, L. Gulay, and V. Shemet, Acta Crystallogr. Sect. B , 172 (2008).

[24] G. A. Bain and J. F. Berry, J. Chem. Ed. **85**, 532 (2008).

[25] A. M. Hallas, A. M. Arevalo-Lopez, A. Z. Sharma, T. Munsie, J. P. Attfield, C. R. Wiebe, and G. M. Luke, Phys. Rev. B **91**, 104417 (2015).

[26] K. Kimura, S. Nakatsuji, J.-J. Wen, C. Broholm, M. B. Stone, E. Nishibori, and H. Sawa, Nat. Commun.s **4**, 1934 (2013).

[27] A. J. Princep, D. Prabhakaran, A. T. Boothroyd, and D. T. Adroja, Phys. Rev. B **88**, 104421 (2013).

[28] K. Matsuhira, Y. Hinatsu, K. Tenya, H. Amitsuka, and T. Sakakibara, J. Phys. Soc. Japan **71**, 1576 (2002).

[29] M. Ciomaga Hatnean, C. Decorse, M. R. Lees, O. A. Petrenko, D. S. Keeble, and G. Balakrishnan, Mater. Res. Express **1**, 026109 (2014).

[30] A. Bertin, P. Dalmas de Réotier, B. Fåk, C. Marin, A. Yaouanc, A. Forget, D. Sheptyakov, B. Frick, C. Ritter, A. Amato, C. Baines, and P. J. C. King, Phys. Rev. B **92**, 144423 (2015).

[31] A. Paduan-Filho, M. S. Droiche, and C. C. Becerra, J. Magn. Magn. Mater. **54-57**, 699 (1986).

[32] K. Yamada and J. Kanamori, Prog. Theo. Phys. **38**, 541 (1967).

[33] I. Maartense, I. Yaeger, and B. M. Wanklyn, Solid State Commun. **21**, 93 (1977).

[34] G. F. Tuthill, J. Phys. C **14**, 2483 (1981).

[35] I. Kimchi, J. P. Sheckelton, T. M. McQueen, and P. Lee, Nat. Commun. **22**, 9(1):4367 (2018).

Chapter 4

Hidden order in the breathing pyrochlore $Nb_4Se_4I_4$

A manuscript of this work is in preparation. It was co-written with the following authors:

Veronica J. Stewart[1,2], Rishi Bhandia[2], Fahad Mahmood[2], Peter Armitage[2], Yuanyuan Xu[2], Natalia Drichko[2], Yuan Tian[3], Mingwei Chen[3], and Tyrel M. McQueen[1,2,3]

[1]Department of Chemistry, The Johns Hopkins University, Baltimore, Maryland 21218, USA

[2]Institute for Quantum Matter, Department of Physics and Astronomy, The Johns Hopkins University, Baltimore, Maryland 21218, USA

[3]Department of Materials Science and Engineering, The Johns Hopkins University, Baltimore, Maryland 21218, USA

4.1 Abstract

The breathing pyrochlore $Nb_4Se_4I_4$ displays a heat capacity anomoly suggestive of a second-order phase transition. However, no evidence of a magnetic or structural transition is observed. This is in contrast to other pyrochlore materials, in which stabilizing Jahn-Teller distortions are not uncommon, but may be compared to "hidden

order" materials such as URu_2Si_2 and $Cd_2Re_2O_7$, where the order parameter of a transition is uncertain. Subtle changes in the phonon modes observed in Raman spectroscopy corroborate the observed transition. Electronic structure calculations suggest that the niobium atoms are highly correlated. Pair distribution function analysis of x-ray diffraction data reveals that the short-range correlations cannot be modeled without a deviation from the cubic structure within the scale of a single tetrahedron. We propose that the observed transition is a change in the manifold of accessible local distortions, driven by Nb-Nb bonding.

4.2 Introduction

The term “hidden order" refers to phases where a symmetry-breaking transition is detectable in thermodynamic measurements, but the order parameter cannot be determined. It was coined to refer to a phase in URu_2Si_2, which forms below a second-order phase transition at $T = 17.5\,K$ [1, 2]. This transition is clearly present in specific heat, with $S \approx 0.2\,R\,ln2$, and was initially attributed to antiferromagnetic ordering or a charge/spin density wave [3–5]. However, further analysis revealed that no long-range magnetic order was present in this phase; the observed magnetism was due to impurities in the sample, and the actual magnetic moment was far too small to account for the entropy in the transition. Likewise, no superlattice associated with charge density wave formation has been observed. Transport, thermoelectricity, and thermal expansion studies also show the transition to the hidden order state [6–8]. Properties from inelastic neutron scattering to magnetic torque to quantum oscillations have provided a great deal of information about this state, and several possibilities for the symmetry breaking have been proposed [9–11]. (Is the symmetry breaking four-fold rotational, time reversal, translational? Is the order spin nematic, hastatic, multipolar? [12–17, 1, 2]) None have been conclusively demonstrated, and after decades of study the nature of this phase is still unknown.

Hidden order phases have been observed in other materials including $Cd_2Re_2O_7$, Sr_2IrO_4, CeCoSi, and NpO_2. CeCoSi enters an ordered state between T = 9.4 and 12 K, or under applied pressure. No magnetic ordering or structural change are observed, but the transition is visible as a kink in heat capacity and magnetization, and as a large anomaly in resistivity under pressure. It has been proposed that the low-temperature and high-pressure states are the same, and that they possess antiferroquadrupolar order [18–20]. In Sr_2IrO_4, breaking of rotational and inversion symmetries are observed via optical second-harmonic generation and polarized neutron diffraction, although structural and magnetic measurements show no such symmetry change. Proposed explanations are ordering of high-rank magnetic multipoles and loop current ordering, as proposed from superconducting cuprates [21, 22]. NpO_2 has a large anomaly in heat capacity at T = 26 K, but the nature of the transition has been difficult to determine. A symmetry lowering seen in NMR measurements was explained as quadrupolar ordering, but later muon spin-rotation experiments contradict this. Among other order parameters, triakontadipolar order has been proposed as an explanation for the experimental data [23–25]. Finally, $Cd_2Re_2O_7$ is a pyrochlore superconductor which has a second-order phase transition at T = 200 K, observed in specific heat, magnetization, and transport measurements, and an additional structural transition at T = 120 K. The higher-temperature transition is cubic to tetragonal, but the small distortion that occurs is not sufficient to explain the entropy loss seen in specific heat; conversely, the entropy loss is too small for long-range magnetic ordering to be likely. The structural changes occuring at the lower-temperature transition are poorly understood. As with the other materials discussed, the order parameter of these transitions requires further study [26–30].

$Nb_4Se_4I_4$ is a breathing pyrochlore material, isoelectronic with $Cd_2Re_2O_7$. The pyrochlore lattice can host magnetically frustrated spins on its a three-dimensional network of corner-sharing tetrahedra, which may give rise to a wide range of prop-

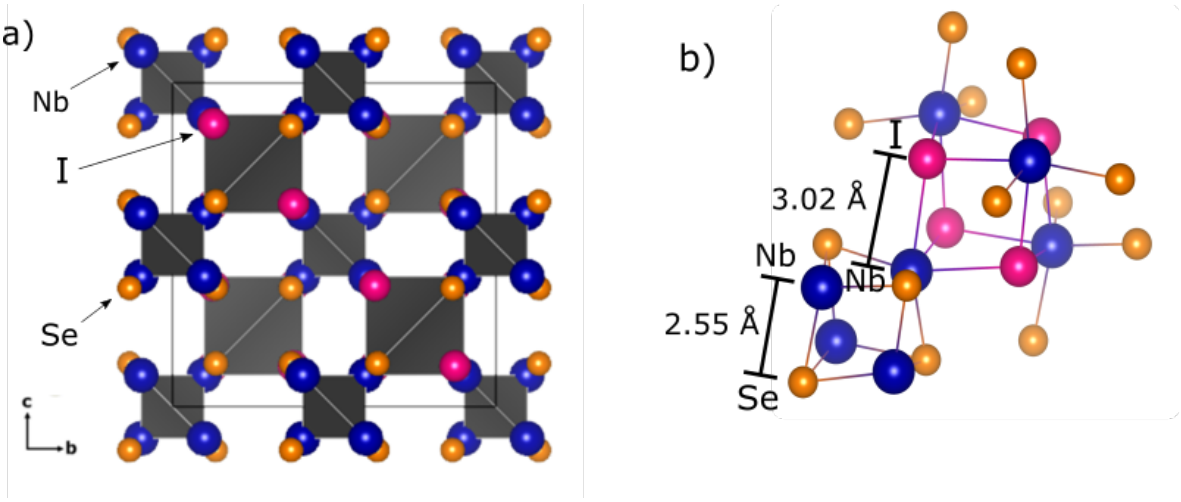

Figure 4-1. (a) The breathing pyrochlore $Nb_4Se_4I_4$, composed of alternating large and small tetrahedra (b) The local structure of the Nb_4 tetrahedra.

erties [31]. Breathing pyrochlores are a closely related class of materials in which the tetrahedra are alternately large and small, giving a "breathing" motif. The formation of tetrahedral clusters in this lattice can be described as a set of atomic displacements from the uniform pyrochlore lattice, lowering the symmetry from Fd-3m to F-43m. $LiGaCr_4O_8$, $LiInCr_4O_8$, $Ba_3Yb_2Zn_5O_{11}$, and $GaMo_4S_8$ are several examples of breathing pyrochlore lattice materials whose magnetic properties have been studied [32–36].

Here we investigate the physical properties of $Nb_4Se_4I_4$, based on previous reports of its synthesis and crystal structure [37–39]. We observe a heat capacity anomaly at $T = 95\,K$ that appears to indicate a transition to a hidden order phase. Structural and magnetic probes show no transition at this temperature, but Raman spectroscopy corroborates it, demonstrating a change in the phonon distribution at low temperatures. In contrast to other materials with hidden order, $Nb_4Se_4I_4$ is entirely diamagnetic, which further narrows the possible origins of the phase transition. We propose a change in the manifold of accessible local Jahn-Teller distortions at the Nb_4 clusters as the most likely explanation.

4.3 Experimental methods

Crystals of $Nb_4Se_4I_4$ were grown using chemical vapor transport, with iodine as a self-transport agent. Starting compositions ranging from 1:1:1 Nb:Se:I to $\approx$ 1:1:1.1 were effective for crystal growth, as was a 0.2:0.8:1 ratio of NbI_5:Nb:Se. The starting materials were heated for 96 hours in an evacuated quartz tube under a 880/790/790°C temperature gradient, yielding well-faceted octahedral black crystals. By repeating this process with a seed crystal, crystals up to ≈ 3 mm in diameter and ≈ 200 mg were obtained. Back-scattered X-ray Laue diffraction on a Multiwire Laboratories MWL with a tungsten source was used to orient the crystals, and indicated that the as-grown crystal surfaces are the $\{1\ 1\ 1\}$ planes.

Single crystal x-ray diffraction (SCXRD) of a representative crystal was performed on a Rigaku SuperNova diffractometer using Mo Kα radiation and an Atlas CCD detector. Data reduction was performed using the CrysAlisPro software package, and the structure was solved with SHELXS and refined with SHELXL [40]. Laboratory powder X-ray diffraction was performed on a Bruker D8 Focus diffractometer and a Bruker D8 Advance powder diffractometer with an Oxford Cryosystems PheniX low-temperature closed cycle cryostat, both using Cu Kα radiation and a LynxEye detector. Synchrotron powder diffraction data were collected on beamline 11-BM-B at the Advanced Photon Source at Argonne National Laboratory, at a wavelength of 0.457878 Å. Discrete detectors covering an angular range from -6 to 16° 2θ were scanned over a 34° 2θ range, with data points collected every 0.001° 2θ and scan speed of 0.01°/s. Data was collected at intervals from 85.0 to 300.0K using an Oxford Cryostream 700+ N_2 cryostat, and from 5.2 to 81.2 K using an Oxford Helium Cryostat. Rietveld refinements were performed with GSAS-II [41]. Isodistort and the program MAXSUB from the Bilbao Crystallographic Server were used for symmetry analysis, structures were visualized with VESTA, and pair distribution function analysis was

performed with PDFgui [42–47].

Magnetization data were collected on a Quantum Design Physical Properties Measurement System (PPMS) using the ACMS option, and on a Quantum Design MPMS 3 Squid Magnetometer. Heat capacity data were collected on the PPMS using the semi-adiabatic method and a 1% temperature rise, and resistivity was measured on the same PPMS using a four-probe method. Crystal surfaces were examined using a JEOL JSM IT100 scanning electron microscope (SEM) with EDS capabilities. Raman spectra were collected from 4 to 290 K with a 10 mW, 514.5 nm laser. Fourier transform infrared spectroscopy (FTIR) reflectivity spectra were collected on a Bruker Vertex 80 in the mid-IR regime from 5-290 K using a MCT detector for room temperature measurements and a DTGS detector for lower temperatures. Terahertz spectra were collected from 5 - 295 K. TEM images and electron diffraction patterns were collected on a Thermo Scientific TF30 300 kV TEM with an ASTAR scanning precession electron diffraction system and analyzed with ImageJ [48, 49]. OriginLab and Python 3.9 were additionally used for data analysis.

Density functional theory calculations were performed using the Elk and Quantum Espresso code suites, the former an all-electron full-potential linearised augmented-plane wave basis with local orbitals (FP-LAPW + LO) (Elk) and the latter a plane-wave basis set with pseudopotentials [50–52]. We used the pseudopotentials Nb.rel-pbe-spn-kjpaw_psl.1.0.0.UPF, Se.rel-pbe-n-kjpaw_psl.1.0.0.UPF, and I.rel-pbe-n-kjpaw_psl.1.0.0.UPF obtained from https://www.quantum-espresso.org/ [53].

4.4 Results

Single crystal x-ray diffraction data was refined in the F-43m space group with a = 10.74620(9), confirming a structure consistent with the literature (Figure 4-1). Refinement details are given in the supporting information (SI 4-12). The breathing

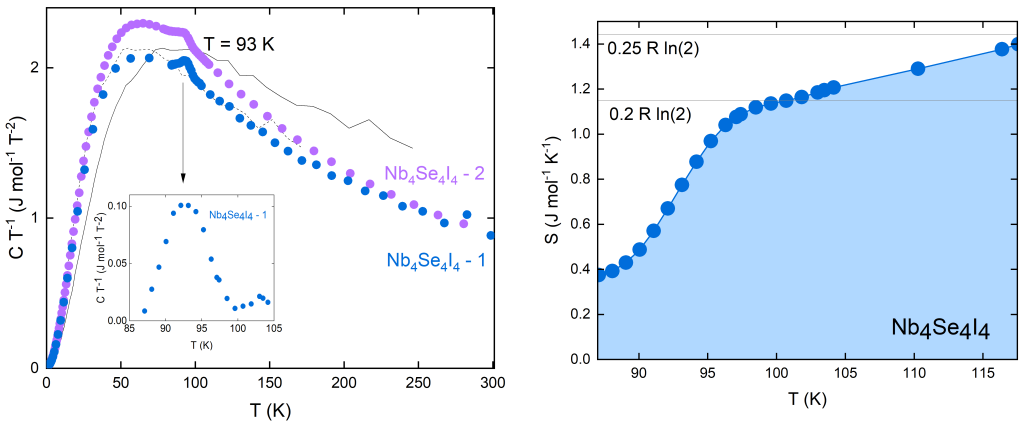

Figure 4-2. (a) Heat capacity of two samples of $Nb_4Se_4I_4$, both with an anomaly at T = 93 K. The inset shows the heat capacity of sample one with the phonon contribution subtracted via the isostructural $Re_4S_4Te_4I_4$. The solid black line in the main plot is the C/T of $Re_4S_4Te_4I_4$, and the dotted line is the mass-density scaled C/T used for the phonon subtraction. (b) Entropy of the transition in $Nb_4Se_4I_4$ at T = 93 K, estimated by integration of heat capacity over temperature of the phonon-subtracted data.

pyrochlore lattice is composed of alternating large and small tetrahedra of niobium. Selenium atoms form the other four corners of a cube with each small Nb_4 tetrahedron, and iodine atoms do the same with the large tetrahedra. The structure can also be described as two interpenetrating face-centered cubic lattices with Nb_4Se_4 clusters as the points of one lattice and I_4 fragments as the points of the other. Each niobium atom is octahedrally coordinated with three Se and three I atoms. Nb has a formal valence of 3+, and thus d2 filling. Since the Nb_4 clusters contain an even number of electrons, the material is expected to be diamagnetic, with the electrons in singlet states at the niobium clusters.

Heat capacity measurements display an anomaly at T = 93 K, consistent across multiple samples (Figure 4-2(a)). The feature suggests a second-order phase transition is occurring. Measurement with a long-pulse HC method, analyzed with the program LongPulseHC, gave no significant difference in heat capacity values, indicating that the transition is unlikely to be first-order [54]. The entropy of the transition was estimated by subtracting the heat capacity of the isostructural material $Re_4S_4Te_4$,

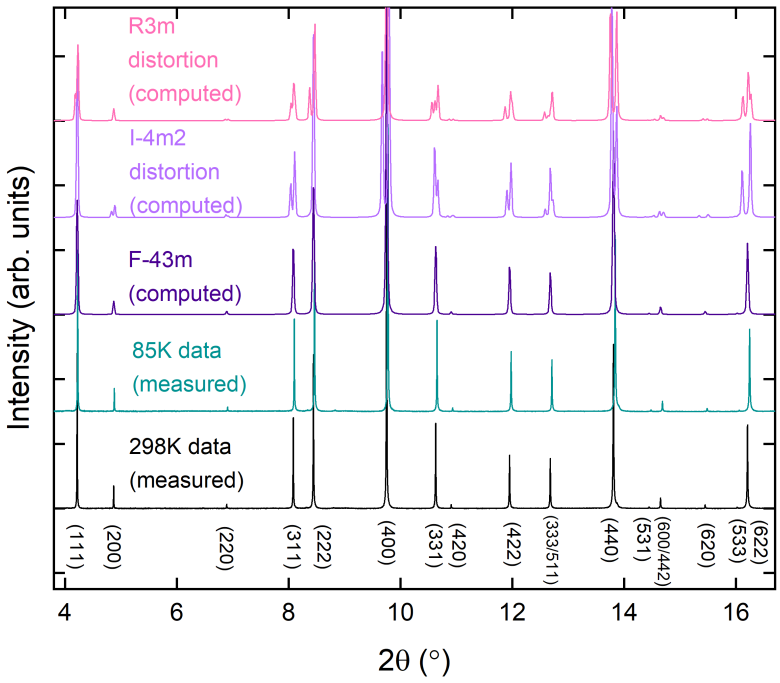

Figure 4-3. A comparison between the PXRD patterns measured above and below the T = 93 K transition and the computed PXRD patterns for the cubic F-43m structure and two possible distortions. No peak splitting consistent with a distortion is observed at either temperature.

after scaling to account for the effect of mass density on the phonon distribution. The entropy was found to be ≈ 1.2 J K^{-1} mol^{-1}, or 0.25 R ln(2) (Figure 4-2(b)).

One possible source of the observed heat capacity anomaly is a magnetic ordering transition. However, magnetic susceptibility measurements indicate no such transition is occurring (SI Figure 4-13). The magnetization is constant across the transition, weakly positive under applied fields of μ_0H = 0.1 T and below, and weakly negative at and above μ_0H = 1 T. The positive component may be attributed to a small Pauli paramagnetism, outweighed by diamagnetism under larger fields. This is consistent with the expected diamagnetic behavior, and a magnetic transition is clearly not responsible for the feature in heat capacity.

Another plausible source for the feature is a structural transition. Powder x-ray diffraction (PXRD) of a ground crystal was performed on the 11-BM-B beamline

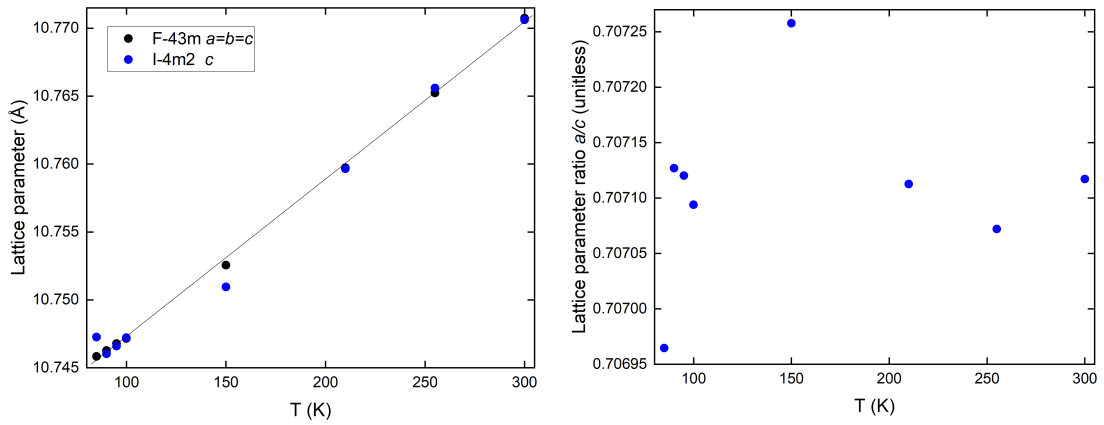

Figure 4-4. Lattice parameters of Nb_4Se_4 determined from sequential refinements in the F-43m and I-4m2 space groups. The change of lattice parameter with temperature is roughly linear in both space groups, with no kink observed at the transition temperature. The second panel shows the ratio of the a and c parameters of I-4m2. This ratio is close to constant, with no temperature dependence, suggesting that no tetragonal distortion is present.

at Argonne National Lab, at temperatures from 5 to 298 K. No peak splitting or broadening was visible across the transition temperature (Figure 4-3). PXRD patterns for transitions to the maximal subgroups of F-43m (I-4m2, R3m, F23, and P-43m) were computed to determined the expected peak splittings [45, 42, 43, 55]. The patterns for I-4m2 and R3m, with a strain distortion of amplitude 0.01 applied, are shown in Figure 4-3 for reference.

Data was sequentially refined in the F-43m space group. Reasonable F-43m refinements could be achieved at all temperatures, and the change in lattice parameter versus temperature remained linear across the transition. Refinements at multiple temperatures in the tetragonal space group I-4m2 also showed no significant change in quality or kink in lattice parameters at the transition (Figure 4-4(a)). Refinements attempted in various additional space groups, including P-43m, F23, P-4n2, and I-4, found no improvement over the cubic structure. We conclude that no structural transition is identifiable in this data set.

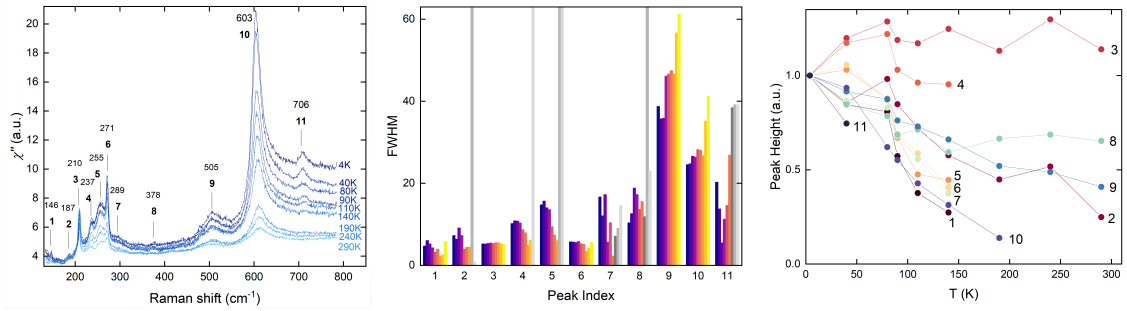

Figure 4-5. (a) Raman spectroscopy of $Nb_4Se_4I_4$. Eleven peaks are identified at T = 4 K. (b) Full width half maximum (FWHM) of each identified peak. Each bar plotted for a single peak represents a different temperature, running from low to high. Grey bars indicate that the peak intensity was too low to get a reliable fit. (c) Peak height versus temperature for each identified peak. Trends in height and FWHM vary between peaks, with some remaining constant (eg. peak 3), some dropping sharply at T = 93 K (eg. peak 4), and some varying linearly with temperature (eg. peak 10). This suggests a subtle change in the nature of the Raman-active modes at the transition temperature.

As neither magnetic or structural experiments showed evidence of the transition, we turned to spectroscopy to investigate the electronic and vibrational structure of the material. Raman spectroscopy results, shown in figure 4-5, corroborate the observed phase transition. Symmetry analysis predicts eleven Raman-active modes in F-43m ($3A_1 + 3E + 5T_2$), and eleven corresponding peaks can be identified at T =4 K [56]. These peaks were integrated at each measured temperature, and the trends in their widths and heights are shown in Figure 4-5(b) and 4-5(c). Some remain nearly constant, some change steadily with temperature, and some, such as the peaks at 187 and 237 cm^{-1}, remain nearly constant below 90 K and show a sharp drop in width and/or height between 90 and 110 K . This behavior suggests that some change affecting the phonon modes is occurring at the transition, but also provides more evidence that this change is not a bulk structural distortion. No peak splitting is observed, and the phonon modes for F-43m persist below the transition, but undergo a subtle change in their temperature dependence.

The eleven peaks are not all identifiable at high temperature. However, because

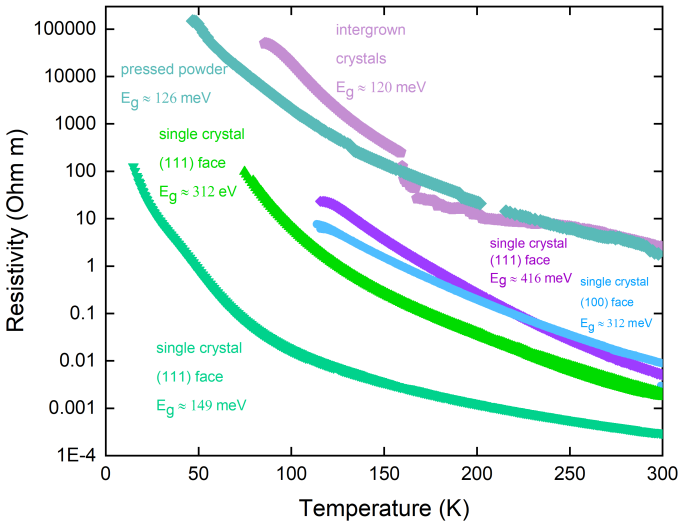

Figure 4-6. Resistivity versus temperature of several samples of Nb_4Se_4. Nb_4Se_4 behaves as a small band-gap semiconductor. The variation between samples is attributed to surface oxidation.

of the low intensity at these temperatures and the evidence from XRD, we believe this does not contradict the identified F-43m structure. Peaks that could not be well fit because of their broadness or low intensity are colored grey in figure 4-5(b), and omitted from figure 4-5(c). The very broad peak at 603 cm^{-1} may be attributed to a crystal effective field level [57].

At 4 K, spectra were collected using two different polarizations, and no clear dependence was observed. Mid-IR FTIR reflectivity and terahertz spectroscopy measurements were also performed. Both show a steady variation with temperature, with no major change below T = 93 K (SI Figure 4-14). No notable features were observed in the measured FTIR range, indicating that the optical band gap most likely lies in the far-IR energy regime.

4.5 Electronic structure

A second puzzle with this material was its insulating nature, which initially seemed incompatible with electronic structure calculations.

Resistivity data was collected on multiple samples, including slices of crystal cut to {111} and {100} faces and a pellet of compressed powder. All samples showed semiconducting behavior, with conductivity decreasing at lower temperatures. Band-gaps were estimated from the slope of ln(R/R300) vs 1/T, and ranged from 120 - 416 meV. The considerable variation between samples most likely originates from surface oxidation. SEM/EDS corroborated this, with oxygen seen on the surface of a crystal left in air for several months. The oxidation seems to occur on the order of days, with the crystal surface gradually discoloring from black to dull brown. This layer can be removed with polishing. The oxide is not visible in laboratory PXRD measurements of ground crystals. To avoid interference from the oxide layer, spectroscopic measurements were performed on crystals that had been stored in an argon glovebox, or had been removed from their sealed quartz tubes immediately before the measurement.

Electronic structure calculations without spin-polarization on the niobium atoms predict that the material is a metal (Figure 4-7). Applying spin-orbit coupling is not sufficient to open a band gap. However, adding a Hubbard U opens a gap; with spin polarization this occurs at the Fermi level, and without it occurs just above, leaving the material as a metal. These results suggest that spin-polarization is required for Nb_4Se_4 to become insulating, which is inconsistent with the observed resistivity and magnetization of the material.

This discrepancy was resolved by using a hybrid functional. By better accounting for electron correlations via a Fock operator, a band gap opens at the Fermi level without magnetism. To understand why this method is more successful, we can examine the Γ point more closely. Without spin orbit coupling, the band at the Fermi level is triply degenerate at this point. Symmetry analysis using the tetrahedral double group shows that an applied spin orbit coupling splits this band into a doublet and a quartet. In non-spin-polarized plane wave calculations, the doublet lies at a

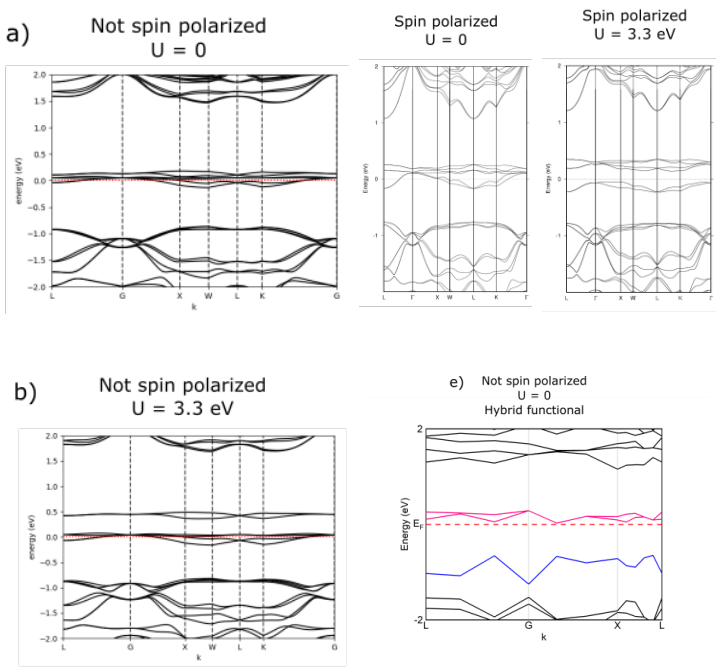

Figure 4-7. Electronic structure calculations for $Nb_4Se_4I_4$. Spin-orbit coupling was turned on for all calculations. (a)-(d) were computed using plane wave DFT, (a) and (b) with the software Quantum Espresso and (c) and (d) with Elk. A band gap opens at the Fermi level only if both spin-polarization and a Hubbard U are applied, suggesting that to be an insulator $Nb_4Se_4I_4$ will have magnetism. (e) However, including a hybrid functional opens a gap at the Fermi level without spin polarization or a U, providing a theoretical justification for $Nb_4Se_4I_4$ to be a non-magnetic insulator as observed. The limited *k* range and point density is due to the computational expense of the calculation.

higher energy and the quartet remains at the Fermi level, leaving the material as a metal. However, by using the hybrid functional (or applying magnetism) the quartet sits above the doublet and a band gap opens over the Fermi level. So, this offers an explanation for why $Nb_4Se_4I_4$ is a non-magnetic insulator: the band gap is opened by electron correlations. These correlations are a factor to consider in explaning the observed phase transition.

Phonon band structure calculations in Quantum Espresso were performed on a non-spin polarized model with no Hubbard U, using a set of fully plane-wave pseudopotentials. These yield an unphysical mix of positive and negative energy levels, further suggesting that this is a poor model for the material. A phonon band structure

could not be attained using hybrid functionals, as only scf calculations are possible in Quantum Espresso using these. This is a direction for future work.

4.6 Discussion

The evidence collected points to a subtle reordering in $Nb_4Se_4I_4$, apparent in thermodynamic and spectroscopic measurements, but not observed in structural or magnetic characterization. Three possible origins of this behavior were considered:

1) A small Jahn-Teller distortion, subtle enough to be not identified in PXRD. Such distortions, driven by spin or orbital ordering, are reported in pyrochlores and spinels with M_4 tetrahedral clusters [58]. Of these materials, the closest analogue to $Nb_4Se_4I_4$ may be GeV_4S_8, which is F-43m at room temperature and has V_4 clusters with eight electrons, the same count as $Nb_4Se_4I_4$ [59, 60]. GeV_4S_8 undergoes a transition to an orthorhombic Imm2 phase at T $\approx$ 30 K. The highest-energy tetrahedral 3d levels, t2, are occupied by two electrons. The orbital-ordering Jahn-Teller distortion splits these levels, stabilizing the material by placing both electrons into a lower-energy a1 level. We might expect the same to occur in $Nb_4Se_4I_4$. Also reported are, for example, a rhombohedral distortion in GaV_4S_8, a tetragonal distortion in ZnV_2O_4, and a metal-insulator and cubic-tetragonal distortion in $MgTi_2O_4$, leading to the formation of spin singlets [61–64]. In all the above, the structural transition is visible in X-ray diffraction measurements, and often accompanied by a magnetic transition. A subtle structual transition in $Nb_4Se_4I_4$ cannot be completely ruled out, but the lack of any apparent peak splitting in our synchrotron PXRD data makes it improbable.

2) A change in space group from F-43m to F23. All atoms in the crystal structure sit on Wyckoff site 16e, which is identical in the two space groups [65]. This could potentially result in a transition with no structural change observed in diffraction. However, there is no apparant driving force behind such a transition, and it does not

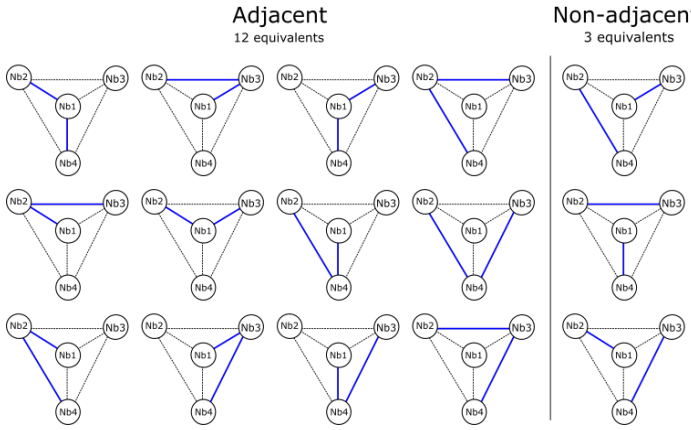

Figure 4-8. Possible configurations of two Nb-Nb bonds within a tetrahedron. Each group of equivalent bond positions corresponds to a set of degenerate structural distortions.

seem physically meaningful as the sole change in the material.

3) A change in the manifold of accessible local distortions. The tetrahedral symmetry of the Nb_4 clusters means that Jahn-Teller distortions in different directions can be equivalent. If the stabilizing effect of a distortion is relatively weak, it may be possible for the Nb atoms to move locally between degenerate distortions, rather than settling in one. The observed transition could then be explained by a change in what sets of degenerate distortions are energetically available.

These local distortions can be thought of as changes in the Nb-Nb bonds. One possibility is that additional bonding is developed between four of the six pairs of Nb-Nb in each tetrahedron, using the eight Nb^{3+} d electrons available. This shortens the distance between these Nb-Nb pairs, leaving the other two distances longer. We consider the different ways the two longer-distance pairs can be arranged on the tetrahedron, and find there are two sets of degenerate configurations (Figure 4-8), with the two longer bonds either adjacent or non-adjacent. The former would correspond to a monoclinic distortion, and the latter to a tetragonal one.

If only the twelve "adjacent" configurations are accessible at low temperature, but all fifteen are at high temperature. We would see a change in entropy from R ln(15) $\approx$ 22.5 J mol^{-1} K^{-1} to R ln(12) $\approx$ 20.7 J mol^{-1} K^{-1}, a loss of 1.8 J mol^{-1} K^{-1}. This

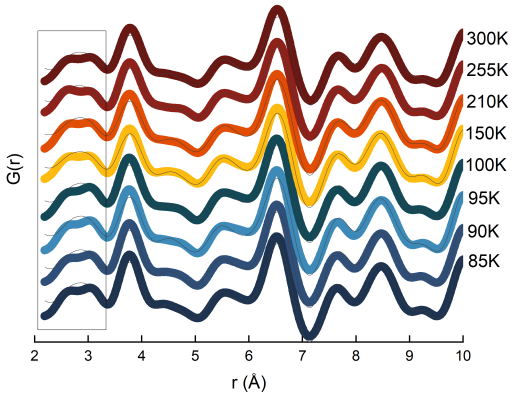

Figure 4-9. Pair distribution function (PDF) analysis of the refined syncrotron PXRD data at various temperatures. Colored lines are the G(r) of the collected data, and thin black lines are a fit in *F-43m*.

is not far from the 1.2 J mol^{-1} K^{-1} of the observed transition.

Although the size of the entropy change makes this seem promising, it is not the only option for the local transitions. For example, we might also see a rhombohedral distortion, with one Nb moving away from the others and elongating its tetrahedron. To investigate further, we used electron diffraction and pair distribution function (PDF) analysis to search for local order in the material. Electron diffraction at room temperature shows a clean single-crystalline pattern indexable in F-43m, with no clear evidence of the local distortions (SI figure 4-15). PDF however, showed the effect of the Nb motion.

At every temperature investigated, the PDF pattern above r $\approx$ 3.3 Å can be well fit in F-43m. However, the short-range pattern cannot be captured by this model (Figure 4-9). The two peaks at the left end are attributed to pairings between Nb-Se ($\approx$ 2.5 Å), Nb-Nb ($\approx$ 3.0 Å), and Nb-I ($\approx$ 3.0 Å). The ratio between the heights of these two peaks varies with temperature, apparently non-systematically. Because there is no splitting of longer-range peaks, such as the I-I peak at r $\approx$ 3.8 Å, we believe the short-range behavior is due to local distortions involving the correlated motion of Nb atoms within a single tetrahedron.

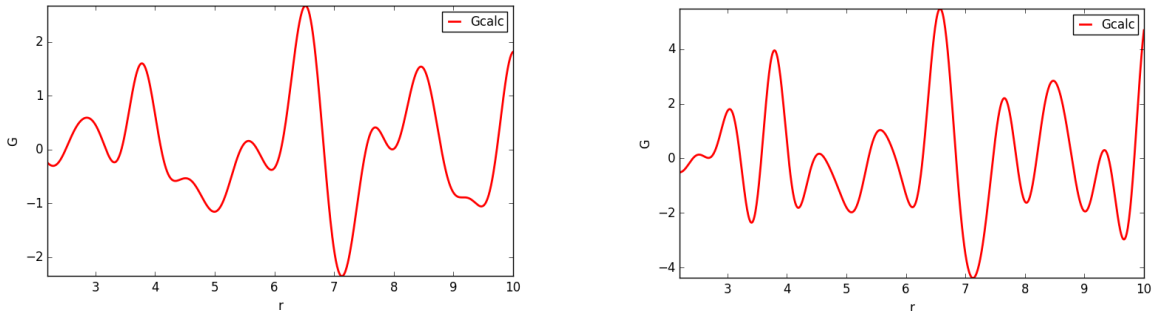

Figure 4-10. Computed PDF patterns for $Nb_4Se_4I_4$. (a) uses the structure determined by our refinement of SCXRD data, and (b) uses a structure from the literature ([38]). The former resembles our PDF data above ≈3.3 Å, but does not capture the short-range peak splitting, while the latter is a poor fit to our data overall, but does show the peak split.

Calculating the expected PDF pattern provides further evidence that the discrepancy between the short and long-range fits is inherent to the F-43m structural model, and not just a result of a poor refinement. The PDF computed from the result of our single-crystal structure solution fits the measured powder PDF well at long range, but fails for the first two peaks (Figure 4-11). The opposite is true for the PDF from a previously-published $Nb_4Se_4I_4$ structure, which captures the short-range peak splitting but fails at long-range [38]. The key difference between the two structures is the thermal parameter of iodine. The short-range peak split is visible if this parameter is low enough, but at the cost of a poor fit at long range. However, this splitting could also be induced by a local distortion that changes the Nb-I distance relative to the Nb-Nb and Nb-Se, which are very similar in F-43m. Due to the large thermal parameter of iodine, the short-range region of our model is dominated by the Nb-I peak, drowning out the peak splitting, but a distortion that moves the Nb-I peak away from the others could allow the split to become visible.

To test this, we constructed lower-symmetry models for three possible distortions. Two were as shown in Figure 4-8, and the third was a rhombohedral elongation as reported in GaV_4S_8. Using Isodistort,we identified the vibrational modes of F-43m corresponding to each distortion: GM3 to tetragonal I-4m2, GM4 to rhombohedral

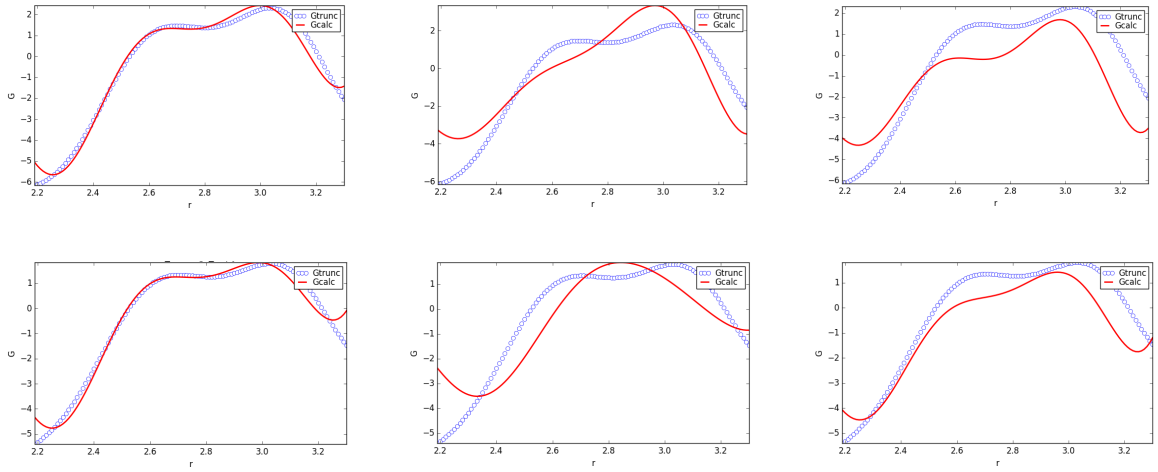

Figure 4-11. Short-range PDF fits in the spacegroups of several possible distortions. Top row: 85 K, bottom row: 300 K. Left to right: R3m, I-4m2, Cm.

R3m, and GM5 to monoclinic Cm [42, 43]. Only the motion of the Nb atoms was considered. In PDFgui, the atomic positions were constrained to limit them to the appropriate vibrational mode. Using the full-range result at each temperature as a starting point, the PDF pattern below 3.3 Å was fit in each of the three space groups. Surprisingly, R3m was by far the best fit at both low and high temperatures.

4.7 Conclusion

Further examination of $Nb_4Se_4I_4$ is required to determine the exact nature of the local distortions, but we have demonstrated that it is a new example of a hidden order material, where the order parameter of a transition is not easily determined. It is distinct from other hidden order materials in that no significant magnetization is observed. We hypothesize that the observed transition is due to a change in the set of energetically accessible local Jahn-Teller distortions, which cause no macroscopic structural distortion due to the symmetry of the Nb_4 tetrahedra. To further investigate this behavior, low-temperature electron diffraction, x-ray diffraction on a dedicated PDF instrument, and phonon band structure calculations using a hybrid functional or

otherwise better modeling the electron correlations would be valuable next steps.

4.8 Acknowledgements

This work was supported as part of the Institute for Quantum Matter, and Energy Frontier Research Center funded by the U.S. Department of Energy, Office of Science, Office of Basic Energy Sciences, under Award DE-SC0019331. Use of the Advanced Photon Source at Argonne National Laboratory was supported by the U. S. Department of Energy, Office of Science, Office of Basic Energy Sciences, under Contract No. DE-AC02-06CH11357. The ^{3}He MPMS was funded by the National Science Foundation, Division of Materials Research, Major Research Instrumentation Program, under Award 1828490. V. Stewart thanks Saul Lapidus for assistance on the 11-BM beamline, Thao T. Tran for helpful discussion, and Chris M. Pasco for assistance with PDF data analysis.

4.9 Supplementary Information

	NbSeI
M (g mol^{-1})	298.77
T (K)	110(2)
Wavelength (Å)	0.71073
Crystal system	cubic
Space group	F-43m (216)
a (Å)	10.74620(9)
V (Å)	1240.98(3)
Z	12
D_c (g cm^{-3})	4.797
μ (mm^{-1})	18.924
θ_{max} (°)	27.272
Number of unique reflections	175
Number of parameters	11
R_{int}	0.0302
GOF	1.329
R(F)	0.0487
$R_w(F_0^2)$	0.115

Figure 4-12. Single crystal x-ray diffraction refinement details.

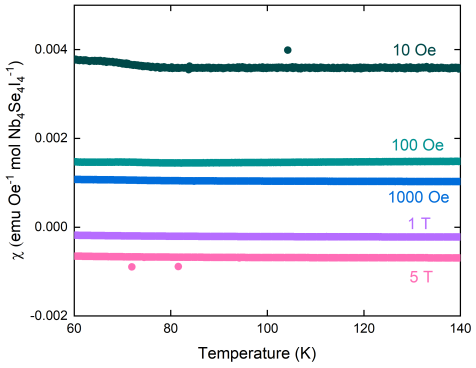

Figure 4-13. DC magnetization of $Nb_4Se_4I_4$ versus temperature. The magnetization is small and constant under all applied fields measured, indicating that $Nb_4Se_4I_4$ is diamagnetic.

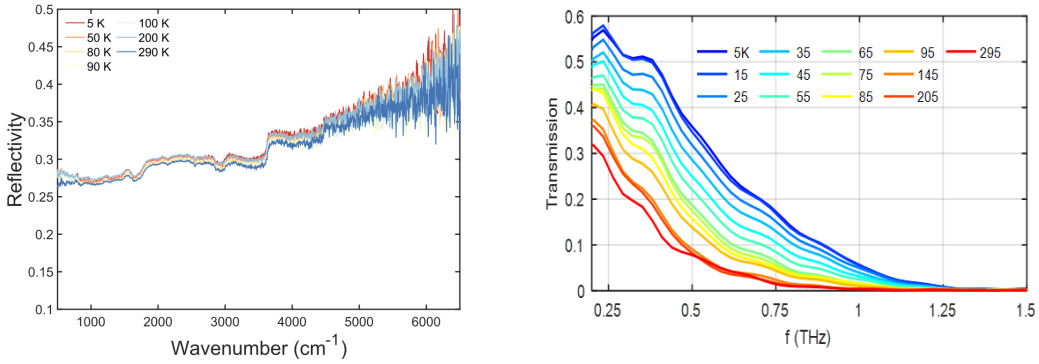

Figure 4-14. (a) Mid-IR FTIR reflectivity. (b) Terahertz spectroscopy of the (111) face of a Nb_4Se_4 crystal.

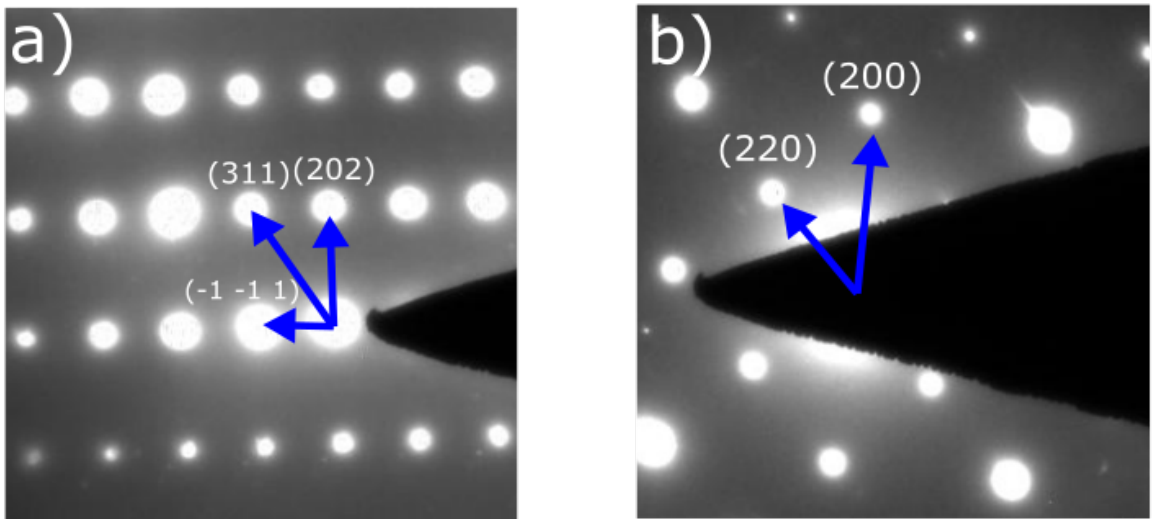

Figure 4-15. TEM/ED images of $Nb_4Se_4I_4$. The patterns can be cleanly indexed in F-43m.

Bibliography

[1] J. A. Mydosh and P. M. Oppeneer, Rev. Mod. Phys. **83**, 1301 (2011).

[2] J. A. Mydosh, P. M. Oppeneer, and P. S. Riseborough, J. Phys.: Condens. Matter **32**, 143002 (2020).

[3] W. Schlabitz, J. Baumann, B. Pollit, U. Rauchschwalbe, H. Mayer, U. Ahlheim, and C. Bredl, Z. Phys. B **62**, 171 (1986).

[4] C. Broholm, J. K. Kjems, W. J. L. Buyers, P. Matthews, T. T. M. Palstra, A. A. Menovsky, and J. A. Mydosh, Phys. Rev. Lett. **58**, 1467 (1987).

[5] M. B. Maple, J. W. Chen, Y. Dalichaouch, T. Kohara, C. Rossel, M. S. Torikachvili, M. W. McElfresh, and J. D. Thompson, Phys. Rev. Lett. **56**, 185 (1986).

[6] R. Bel, H. Jin, K. Behnia, J. Flouquet, and P. Lejay, Phys. Rev. B **70**, 220501 (2004).

[7] A. de Visser, F. E. Kayzel, A. A. Menovsky, J. J. M. Franse, J. van den Berg, and G. J. Nieuwenhuys, Phys. Rev. B **34**, 8168 (1986).

[8] T. T. M. Palstra, A. A. Menovsky, and J. A. Mydosh, Phys. Rev. B **33**, 6527 (1986).

[9] R. Okazaki, T. Shibauchi, H. J. Shi, Y. Haga, T. D. Matsuda, E. Yamamoto, Y. Onuki, H. Ikeda, and Y. Matsuda, Science **331**, 439 (2011).

[10] H. Shishido, K. Hashimoto, T. Shibauchi, T. Sasaki, H. Oizumi, N. Kobayashi, T. Takamasu, K. Takehana, Y. Imanaka, T. D. Matsuda, Y. Haga, Y. Onuki,

and Y. Matsuda, Phys. Rev. Lett. **102**, 156403 (2009).

[11] C. Broholm, H. Lin, P. T. Matthews, T. E. Mason, W. J. L. Buyers, M. F. Collins, A. A. Menovsky, J. A. Mydosh, and J. K. Kjems, Phys. Rev. B **43**, 12809 (1991).

[12] E. R. Schemm, R. E. Baumbach, P. H. Tobash, F. Ronning, E. D. Bauer, and A. Kapitulnik, Phys. Rev. B **91**, 140506 (2015).

[13] R. Yoshida, K. Tsubota, T. Ishiga, M. Sunagawa, J. Sonoyama, D. Aoki, J. Flouquet, T. Wakita, Y. Muraoka, and T. Yokoya, Scientific reports **3**, 2750 (2013).

[14] S. Fujimoto, Phys. Rev. Lett. **106**, 196407 (2011).

[15] P. Chandra, P. Coleman, and R. Flint, Nature (London) **493**, 621 (2013).

[16] P. Santini and G. Amoretti, Phys. Rev. Lett. **73**, 1027 (1994).

[17] Y. L. Wang, G. Fabbris, D. Meyers, N. H. Sung, R. E. Baumbach, E. D. Bauer, P. J. Ryan, J.-W. Kim, X. Liu, M. P. M. Dean, G. Kotliar, and X. Dai, Phys. Rev. B **96**, 085146 (2017).

[18] H. Tanida, K. Mitsumoto, Y. Muro, T. Fukuhara, Y. Kawamura, A. Kondo, K. Kindo, Y. Matsumoto, T. Namiki, T. Kuwai, and T. Matsumura, J. Phys. Soc. Jpn. **88**, 054716 (2019).

[19] H. Tanida, Y. Muro, and T. Matsumura, J. Phys. Soc. Jpn. **87**, 023705 (2018).

[20] E. Lengyel, M. Nicklas, N. Caroca-Canales, and C. Geibel, Phys. Rev. B **88**, 155137 (2013).

[21] J. Jeong, Y. Sidis, A. Louat, V. Brouet, and P. Bourges, Nature Communications **8** (2017).

[22] L. Zhao, D. Torchinsky, H. Chu, V. Ivanov, R. Lifshitz, R. Flint, T. Qi, G. Cao, and D. Hsieh, Nature Physics **12** (2015).

[23] Y. Tokunaga, Y. Homma, S. Kambe, D. Aoki, H. Sakai, E. Yamamoto, A. Nakamura, Y. Shiokawa, R. E. Walstedt, and H. Yasuoka, Phys. Rev. Lett. **94**, 137209

(2005).

[24] E. F. Westrum, J. B. Hatcher, and D. W. Osborne, The Journal of Chemical Physics **21**, 419 (1953).

[25] L. V. Pourovskii and S. Khmelevskyi, Proceedings of the National Academy of Sciences **118**, 10.1073/pnas.2025317118 (2021).

[26] R. Jin, J. He, J. Thompson, M. Chisholm, B. Sales, and D. Mandrus, J. Phys.: Condens. Matter **14** (2002).

[27] Z. Hiroi, M. Hanawa, Y. Muraoka, and H. Harima, J. Phys. Soc. Jpn. **72**, 21 (2003).

[28] I. A. Sergienko and S. H. Curnoe, J. Phys. Soc. Jpn. **72**, 1607 (2003).

[29] Z. Hiroi, J.-i. Yamaura, T. C. Kobayashi, Y. Matsubayashi, and D. Hirai, J. Phys. Soc. Jpn. **87**, 024702 (2018).

[30] M. R. Norman, Phys. Rev. B **101**, 045117 (2020).

[31] J. S. Gardner, M. J. P. Gingras, and J. E. Greedan, Rev. Mod. Phys. **82**, 53 (2010).

[32] Y. Okamoto, G. J. Nilsen, J. P. Attfield, and Z. Hiroi, Phys. Rev. Lett. **110**, 097203 (2013).

[33] Y. Tanaka, M. Yoshida, M. Takigawa, Y. Okamoto, and Z. Hiroi, Phys. Rev. Lett. **113**, 227204 (2014).

[34] J. G. Rau, L. S. Wu, A. F. May, A. E. Taylor, I.-L. Liu, J. Higgins, N. P. Butch, K. A. Ross, H. S. Nair, M. D. Lumsden, M. J. P. Gingras, and A. D. Christianson, J. Phys.: Condens. Matter **30**, 455801 (2018).

[35] E. C. Schueller, D. A. Kitchaev, J. L. Zuo, J. D. Bocarsly, J. A. Cooley, A. Van der Ven, S. D. Wilson, and R. Seshadri, Phys. Rev. Materials **4**, 064402 (2020).

[36] S. Reschke, F. Meggle, F. Mayr, V. Tsurkan, L. Prodan, H. Nakamura, J. Deisen-

hofer, C. A. Kuntscher, and I. Kézsmárki, Phys. Rev. B **101**, 075118 (2020).

[37] H. B. Yaich, J. C. Jegaden, M. Potel, M. Sergent, A. K. Rastogi, and R. Tournier, J. Less Common Metals **102**, 9 (1984).

[38] V. E. Fedorov, V. K. Evstaf'ev, S. D. Kirik, and A. V. Mishchenko, Zh. Neorg. Khim.; (USSR) **26:10**.

[39] M. N. Sokolov and V. P. Fedin, Coordination Chemistry Reviews **248**, 925 (2004).

[40] G. M. Sheldrick, Acta Crystallogr. Sect. A **64**, 112 (2008).

[41] B. Toby and R. von Dreele, J. Appl. Crystallogr. **46**, 544 (2013).

[42] B. Campbell, H. Stokes, D. Tanner, and D. Hatch, ISODISPLACE computer programs J. Appl. Cryst **39**, 607 (2006).

[43] H. Stokes, D. Hatch, and B. Campbell, .

[44] M. Aroyo, J. Perez-Mato, D. Orobengoa, E. Tasci, G. De La Flor, and A. Kirov, Bulgarian Chemical Communications **43**, 183 (2011), cited By 291.

[45] M. I. Aroyo, J. M. Perez-Mato, C. Capillas, E. Kroumova, S. Ivantchev, G. Madariaga, A. Kirov, and H. Wondratschek, Z. Kristallogr. **221**, 15 (2006).

[46] M. I. Aroyo, A. Kirov, C. Capillas, J. M. Perez-Mato, and H. Wondratschek, Acta Crystallogr. Sect. A **62**, 115 (2006).

[47] C. L. Farrow, P. Juhas, J. W. Liu, D. Bryndin, E. S. Božin, J. Bloch, T. Proffen, and S. J. L. Billinge, J. Phys.: Condens. Matter **19**, 335219 (2007).

[48] C. Rueden, J. Schindelin, M. Hiner, B. Dezonia, A. Walter, and K. Eliceiri, BMC Bioinformatics **18** (2017).

[49] J. Schindelin, I. Arganda-Carreras, E. Frise, V. Kaynig, M. Longair, T. Pietzsch, S. Preibisch, C. Rueden, S. Saalfeld, B. Schmid, J.-Y. Tinevez, D. White, V. Hartenstein, K. Eliceiri, P. Tomancak, and A. Cardona, Nature Methods **9**, 676 (2012).

[50] The Elk Code, http://elk.sourceforge.net/.

[51] P. Giannozzi *et al.*, J. Phys.: Condens. Matter **21**, 395502 (2009).

[52] P. Giannozzi, O. Andreussi, T. Brumme, O. Bunau, M. B. Nardelli, M. Calandra, R. Car, C. Cavazzoni, D. Ceresoli, M. Cococcioni, N. Colonna, I. Carnimeo, A. D. Corso, S. de Gironcoli, P. Delugas, R. A. DiStasio, A. Ferretti, A. Floris, G. Fratesi, G. Fugallo, R. Gebauer, U. Gerstmann, F. Giustino, T. Gorni, J. Jia, M. Kawamura, H.-Y. Ko, A. Kokalj, E. Küçükbenli, M. Lazzeri, M. Marsili, N. Marzari, F. Mauri, N. L. Nguyen, H.-V. Nguyen, A. O. de-la Roza, L. Paulatto, S. Poncé, D. Rocca, R. Sabatini, B. Santra, M. Schlipf, A. P. Seitsonen, A. Smogunov, I. Timrov, T. Thonhauser, P. Umari, N. Vast, X. Wu, and S. Baroni, J. Phys.: Condens. Matter **29**, 465901 (2017).

[53] A. Dal Corso, Computational Materials Science **95**, 337 (2014).

[54] A. Scheie, J. Low Temp. Phys. **193**, 60 (2018).

[55] K. Momma and F. Izumi, J. Appl. Crystallogr. **44**, 1272 (2011).

[56] E. Kroumova, M. Aroyo, J. Perez-Mato, A. Kirov, C. Capillas, S. Ivantchev, and H. Wondratschek, Phase Transitions **76**, 155 (2003).

[57] A. Scheie, arXiv preprint **2006.15151** (2020).

[58] Y. Yamashita and K. Ueda, Phys. Rev. Lett. **85**, 4960 (2000).

[59] S. Widmann, A. Günther, E. Ruff, V. Tsurkan, H.-A. Krug von Nidda, P. Lunkenheimer, and A. Loidl, Phys. Rev. B **94**, 214421 (2016).

[60] D. Bichler, H. Slavik, and D. Johrendt, Zeitschrift für Naturforschung B **64**, 915 (2009).

[61] K. Xu and H. J. Xiang, Phys. Rev. B **92**, 121112 (2015).

[62] Y. Ueda, N. Fujiwara, and H. Yasuoka, Journal of the Physical Society of Japan **66**, 778 (1997).

[63] M. Schmidt, W. Ratcliff, P. G. Radaelli, K. Refson, N. M. Harrison, and S. W. Cheong, Phys. Rev. Lett. **92**, 056402 (2004).

[64] S. Leoni, A. N. Yaresko, N. Perkins, H. Rosner, and L. Craco, Phys. Rev. B **78**, 125105 (2008).

[65] E. Kroumova, J. M. Perez-Mato, and M. I. Aroyo, J. Appl. Crystallogr. **31**, 646 (1998).

Conclusions

The in-depth characterization of several materials with unusual properties has been reported. One, the breathing pyrochlore $Nb_4Se_4I_4$, exhibits a subtle phase transition, apparent in thermodynamic measurements, but not in bulk structural or magnetic properties. The others, the distorted hexagonal lattice materials Nd_2S_5Sn and Pr_2S_5Sn, display strikingly different magnetic properties despite being isostructural. The Nd compound antiferromagnetically orders at $T_N = 2.6$ and undergoes a series of quantum phase transitions driven by an applied magnetic field. The Pr compound behaves paramagnetically down to T = 0.45 K, and may be proximate to a spin liquid state. Both $Nb_4Se_4I_4$ and the Ln_2S_5Sn had been previously reported, but very little physical properties characterization had been published. The work here raises questions that may lead to further research on these materials. What precisely is occuring in the hidden order transition in $Nb_4Se_4I_4$? Can the hypothesized manifold of degenerate Jahn-Teller distortions be confirmed? What AFM order is present in Nd_2S_5Sn, and what changes does it undergo in an applied magnetic field? What is the behavior of Pr_2S_5Sn below T = 0.45 K? Is there a connection to the Kitaev quantum spin liquid, and if so, how does the reduced symmetry of its distorted hexagonal lattice affect the magnetism?

The reported materials were identified as part of a search for axion insulators, a hypothesized category of topological materials, illustrating one of the strengths of the materials by design process. By starting from the general properties needed for a class of materials - such as large spin-orbit coupling or particular symmetries - we cast a

wide net and identify many materials with properties that may lead to interesting behavior. The materials discussed here were not axion insulators, but without this seach process, their unusual properties may not have been discovered.

The search for an intrinsic axion insulator is still ongoing. $MnBi_2Te_4$, the most promising candidate to date, has the necessary topological band inversion, but is metallic in the bulk due to intersite defects, and in many reports has gapless surface states instead of the predicted surface band gap [1, 2]. Whether the surfaces are gapped or not, it is considered the first intrinsic magnetic topological insulator.

For this work, samples of $MnBi_2Te_4$ and the additional candidates $EuMn_2P_2$ and $Y_2Ru_2O_7$ were produced. Millimeter scale single crystals of $EuMn_2P_2$ and powders of $MnBi_2Te_4$ were used by collaborators for studies of their physical properties [3, 4]. Additionally, exploratory crystal growths of $MnBi_2Te_4$ and $Y_2Ru_2O_7$ were carried out. Most significantly, lists of potential axion insulator candidates were compiled by systematic database searches. DFT band structure calculations were used to narrow down these lists, followed by the synthesis of the most promising candidates. Many of the identified materials have still not been explored. It is hoped that both these candidates and the principles by which they were identified will be of use in future research. A true intrinsic axion insulator may be discovered tomorrow, or only in the distant future, but either way the search for one is sure to lead to interesting places.

Bibliography

[1] P. Swatek, Y. Wu, L.-L. Wang, K. Lee, B. Schrunk, J. Yan, and A. Kaminski, Phys. Rev. B **101**, 161109 (2020).

[2] Y.-J. Hao *et al.*, Phys. Rev. X **9**, 041038 (2019).

[3] V. Morano, V. Stewart, Y. Qiu, C. Brown, T. McQueen, and C. L. Broholm (2020), APS March Meeting.

[4] T. Berry *et al.* (2021), APS March Meeting.

Appendix I

Axion Insulator Candidates

Table I-I. Candidates identified in the database search for $\mathbb{Z}_2$ TI adjacent isotropic magnetoelectric materials. Materials were included if they had a non-d0/d10 transition metal on a Wyckoff position identified by Vanderbilt and Coh's study of appropriate structures (Phys. Rev. B 88, 121106(R)). For space group / Wyckoff position combinations with fewer hits in the ISCD, all candidates found are included in the table. For larger groups, examples from each structure type are included, but not all unique materials.

Space Group	**Wyckoff position**	**Compound**	**Elements in Wyckoff position**	**Structure type**
198	4a	$TlCo(CO)_4$	Tl, Co, C, O	$TlCo(CO)_4$
		$Tl(Fe(CO)_3(NO)$	Tl, Fe, N, O	$TlCo(CO)_4$
		PdF_2	Pd, F	ZrOS
		K_9Ni_2O7	K, Ni, O	$K_9Fe_2S_7$
		$K_9(FeS_3)(FeS_4)$	Fe, K, S	$K_9Fe_2S_7$
		$Cs_9Fe_2S_7$	Fe, Cs, Se	$K_9Fe_2S_7$
		$Rb_9(FeSe_3)(FeSe_4)$	Fe, Rb, Se	$K_9Fe_2S_7$
		$K_9(FeO_3)(FeO_4)$	Fe, K, O	$K_9Fe_2S_7$
		$K_9Co_2S_7$	Co, K, S	$K_9Fe_2S_7$
		$K_2Mn_2(BeF_4)_3$	Mn, K	Langbeinite-$K_2Mg_2(SO_4)_3$
		$(NH_4)_2Mn_2(SO_4)_3$	N, Mn	Langbeinite-$K_2Mg_2(SO_4)_3$
		$Rb_2Mn_2(SO_4)_3$	Rb, Mn	Langbeinite-$K_2Mg_2(SO_4)_3$
		$Rb_2Mn_2(MoO_4)_3$	Rb, Mn	Langbeinite-$K_2Mg_2(SO_4)_3$
		$KBaFe_2(PO_4)_3$	Fe, K, Ba	Langbeinite-$K_2Mg_2(SO_4)_3$
		$K_2SnFe(PO_4)_3$	Fe, Sn, K	Langbeinite-$K_2Mg_2(SO_4)_3$
		$K_2Ti_2(PO_4)_3$	Ti, K	Langbeinite-$K_2Mg_2(SO_4)_3$
		$K_4Ti_3Ni(PO_4)_6$	Ti, Ni, K	Langbeinite-$K_2Mg_2(SO_4)_3$
		$K_2Ni_2(SO_4)_3$	Ni, K	Langbeinite-$K_2Mg_2(SO_4)_3$

Space Group	Wyckoff position	Compound	Elements in Wyckoff position	Structure type
		$K_2Mn_2(SO_4)_3$	Mn, K	Langbeinite-$K_2Mg_2(SO_4)_3$
		$K_2(YZr)(PO_4)_3$	Y, Zr, K	Langbeinite-$K_2Mg_2(SO_4)_3$
		$K_2(YHf)(PO_4)_3$	Y, Hf, K	Langbeinite-$K_2Mg_2(SO_4)_3$
		$K_2Co_2(SO_4)_3$	Co, K	Langbeinite-$K_2Mg_2(SO_4)_3$
		$K_2(YTi)(PO_4)_3$	Y, Ti, K	Langbeinite-$K_2Mg_2(SO_4)_3$
		$K_2(SnFe)(PO_4)_3$	Sn, Fe, K	Langbeinite-$K_2Mg_2(SO_4)_3$
		$Rb_2(FeZr)(PO_4)_3$	Fe, Zr, Rb	Langbeinite-$K_2Mg_2(SO_4)_3$
		$Rb_2(TiY)(PO_4)_3$	Ti, Y, Rb	Langbeinite-$K_2Mg_2(SO_4)_3$
		$Na_2FeTi(PO_4)_3$	Fe, Ti, Na	Langbeinite-$K_2Mg_2(SO_4)_3$
		$K_2Fe_2(PO_4)_2(MoO_4)$	Fe, K	Langbeinite-$K_2Mg_2(SO_4)_3$
		$K_2Sc_2(PO_4)_2(MoO_4)$	Sc, K	Langbeinite-$K_2Mg_2(SO_4)_3$
		$Ba_3V_4(PO_4)_6$	V, Ba	$Ba_3V_4(PO_4)_6$
		$K_{1.75}Ti_2(PO_4)_3$	Ti, K	$Ba_3V_4(PO_4)_6$
		$Pb_{1.5}V_2(PO_4)_3$	Pb, V	$Ba_3V_4(PO_4)_6$
		$Ba_{1.5}Fe_2(PO_4)_3$	Fe, Ba	$Ba_3V_4(PO_4)_6$
		$Bi_3(ReO_8)$	Re, O	$CeZrO_4$
		IrSbS	Ir, Sb, S	NiSSb
		IrSbSe	Ir, Sb, Se	NiSSb
		IrBiSe	Ir, Bi, Se	NiSSb
		IrSbTe	Ir, Sb, Te	NiSSb
		CoAsS	Co, As, S	NiSSb
		IrPSe	Ir, P, Se	NiSSb
		CoSbS	Co, Sb, S	NiSSb
		RhBiS	Rh, Bi, S	NiSSb
		RhPSe	Rh, P, Se	NiSSb
		RhSbS	Rh, Sb, S	NiSSb
		RhSbSe	Rh, Sb, Se	NiSSb
		$K_2Mn_2(SO_4)_3$	Mn, K	$K_2Mn_2(SO_4)_3$
		$EuMgNiH_4$	Ni, Eu, Mg	Na_3AsS_3
		$CaMgNiH_4$	Ni, Ca, Mg, H	Na_3AsS_3
		$Na_3TiN(PO_3)_3$	Ti, Na, N	$Na_3AlN(PO_3)_3$
		$Na_3V(PO_3)_3N$	V, Na, N	$Na_3AlN(PO_3)_3$
		$Sr(MnO_4)_2(H_2O)_3$	Sr, Mn, O	
		$Cu_2O(SeO_3)$	Cu, O, Se	
		$(Co(NH_3)_6)Cl(CO_3)$	Co, Cl, C	
		$Na(Mn(HCOO)_3)$	Mn, Na	
199	12b	Mn_2O_3	Mn	Sm_2O_3(cI80)
		$FeMnO_3$	Fe, Mn	Sm_2O_3(cI80)
199	8a	Mn_2O_3	Mn	Sm_2O_3(cI80)
		$FeMnO_3$	Fe, Mn	Sm_2O_3(cI80)

Space Group	Wyckoff position	Compound	Elements in Wyckoff position	Structure type
		$Ba_3Fe_2O_5Cl_2$	Fe, Cl, O	$Ba_3Fe_2O_5Cl_2$
		$Ba_3Fe_2O_5Br_2$	Fe, Br, O	$Ba_3Fe_2O_5Cl_2$
		Bi_3ReO_8	Re, O	$ReBi_3O_8$
		$NaCo(HCOO)_3$	Co, Na	
204	12e	$ReSr_{0.4}O_3$	Re	$KSbO_3$
205	8c	$CsEr(Er_6CoI1_2)_2$	Co	
206	24d	$Cu_3(TeO_6)$	Cu	Bixbyite-Mn_2O_3
		$FeMnO_3$	Mn, Fe	Bixbyite-Mn_2O_3
		Mn_2O_3	Mn	Bixbyite-Mn_2O_3
		$YZrO_3$	Y, Zr	Bixbyite-Mn_2O_3
		$(TmY)O_3$	Tm, Y	Bixbyite-Mn_2O_3
		$Cu_2Ni(TeO_6)$	Cu, Ni	Bixbyite-Mn_2O_3
		Be_3Ru_2	Ru	Bixbyite-Mn_2O_3
		Fe_2O_3	Fe	Bixbyite-Mn_2O_3
		$YbCoO_3$	Yb, Co	Bixbyite-Mn_2O_3
		$GdYO_3$	Ge, Y	Bixbyite-Mn_2O_3
		$YSmO_3$	Y, Sm	Bixbyite-Mn_2O_3
		$ScFeO_3$	Sc, Fe	Bixbyite-Mn_2O_3
		V_2O_3	V	Bixbyite-Mn_2O_3
		$YPrO_3$	Y, Pr	Bixbyite-Mn_2O_3
		Cu_2FeSbO_6	Cu, Fe	Bixbyite-Mn_2O_3
		$YbYO_3$	Y, Yb	Bixbyite-Mn_2O_3
		$Ru(NH_3)_6(ClO_4)_3$	Ru, N	
206	16c	$YPrO_{3.43}$	Y, Pr, O	Bixbyite
212	12d	$LiFe_5O_8$	Fe	Spinel-$LiFe_5O_8$
		$Li_2MgMn_3O_8$	Mn	Spinel-$LiFe_5O_8$
		$LiMnTiO_4$	Ti, Mn, Li	Spinel-$LiFe_5O_8$
		$Ag_4Mn_3O_8$	Mn	
		$Mn_3Li_2ZnO_8$	Mn	
212	8c	$Ti_3CoLi_2O_8$	Co, Li, O	Spinel-$LiFe_5O_8$
		$Ge_3CoLi_2O_8$	Co, Li, O	Spinel-$LiFe_5O_8$
		$LiFe_5O_8$	Fe, O	Spinel-$LiFe_5O_8$
		$Ge_3NiLi_2O_8$	Ni, Li, O	Spinel-$LiFe_5O_8$
		$Li_2CoTi_3O_8$	Co, Li, O	Spinel-$LiFe_5O_8$
		$Fe_{21.34}O_{32}$	Fe	Fe_21+xO_{32}
		$LiMnTiO_4$	Mn, Ti, Li, O	
215	4e	$Cu_4In_9Se_{16}$	Cu, Se	$Cu_4In_9Se_{16}$
		$P_4O_6(Ni(CO)_3)_4$	Ni, P	
		$Cs_3(Mo_4O_4)(PO_4)_3$	Mo, O	
		$K_{10}(Mn_4Sn_4S_{17})$	Mn, Sn, S, K	
		$K_{10}(Co_4Sn_4S_{17})$	Co, Sn, S, K	
		$K_{10}(Fe_4Sn_4S_{17})$	Fe, Sn, S	
		$LiMgIrH_6$	Ir	
		$(Ru_4Dy_{16})I_{28}(Dy_4)$	Ru, Dy, I	
		$(Ru_4Ho_{16})I_{28}(Ho_4)$	Ru, Ho, I	
216	16e	$YBaFe_4O_7$	Fe	$YBaFe_4O_7$
		DyBaFe$_4$O7	Fe	YBaFe$_4$O7
		$Ga_{0.5}Mo_2S_4$	Mo, S	$GaMo_4S_8$(HT)
		$GaMo_4S_8$	Mo, S	$GaMo_4S_8$(HT)
		$AlMo_4S_8$	Mo, S	$GaMo_4S_8$(HT)
		$GaMo_4Se_4Te_4$	Mo, Se, Te	$GaMo_4S_8$(HT)

Space Group	Wyckoff position	Compound	Elements in Wyckoff position	Structure type
		GeV_4S_8	V, S	$GaMo_4S_8$(HT)
		$GaNb_4S_8$	Nb, S	$GaMo_4S_8$(HT)
		Co_3O_4	Co, O	Spinel-Al_2MgO_4, reduced symmetry
		$MnIn_2S_4$	Mn, In, S	Spinel-Al_2MgO_4, reduced symmetry
		$FeIn_2S_4$	Fe, S, In	Spinel-Al_2MgO_4, reduced symmetry
		Li_2VCl_4	V, Li, Cl	Spinel-Al_2MgO_4, reduced symmetry
		$Re_4S_4Te_4$	Re, S, Te	NbSeI
		$Nb_4Se_4I_4$	Nb, Se, I	NbSeI
		MoSBr	Mo, S, Br	NbSeI
		$Bi_4Mn_5Ni_2$	Mn, Ni	$Cu_4Mn_3Bi_4$
		$LiGaCr_4O_8$	Cr, O	$LiGaCr_4O_8$
		$LiInCr_4O_8$	Cr, O	$LiGaCr_4O_8$
		Ni_2YD_3	Ni, Y	Ni_2YHx-frame
		$YMgNi_4H_4$	Ni, H	$YMgNi_4H_4$
		Dy_2TiO_5	Ti, Dy	
		$K_4Pt_4S_{22}(H_2O)_4$	Pt, S	
217	8c	Ta_2O	Ta, O	
220	24d	$BiMnO_{2.81}$	Mn, O	
220	16c	$(OLi_2Ca_4)_3(ReN_4)_4$	Re, N	$Li6Ca1_2Mo_4N_{16}O_3$
		$Pb_3V(PO_4)_3$	V, Pb	eulytite
		Ti_4As_3	Ti	Th_3P_4
		Ti_4P_3	Ti	Th_3P_4
		$Ca_{12}(Fe_{10.33}Si_{3.67})O_{32}Cl_{5.45}$	Fe, Si, O	Wadalite
		$BiMnO_{2.81}$	Mn, Bi	
221	8g	$(Mn_4Na_4(Si1_2Al1_2O_{48}))(C_3H6)_4$	Mn	Zeolite-A-frame
221	6e	$(Fe_{0.8}Zr_{0.2})F_{3.2}$	Fe, Zr	$YbZrF_7$
225	48h	$Mn_7FeCl_3O_{10}$	Mn	$Mn7FeCl_3O_{10}$
225	32f	$Mn_{23}Sm_6H_{24}$	Mn	$Mn_{23}Th_6$-filled
		$Co_{16}Zr_6Si_7$	Co	$Mn_{23}Th_6$
		$Ag_8Ca_{19}N_7$	Ag	$K_{19}Pb_8O_4(OH)_3$
		Co_8NiS_8	Co	Co_9S_8
		Cu_5FeS_4	Cu	Cu_2FeS_2
		$Cu_{1.8}Se$	Cu	Cu_2-xSe
		$Cu_3(Fe(CN)_6)_2(H_2O)_2$	Cu	
		$Y_3(TaO_7)$	Y	
227	96h	$Hg_2Ag_{18}(H_{22}O_{33})(ClO_4)_4$	Ag	
227	48f	V_4Co_2N	V	Carbide(eta)-Fe_3W_3C
		Zr_4Pt_2N	Zr	Carbide(eta)-Fe_3W_3C
		Cr_3Ni_2Si	Cr	$NiTi_2$
		Mo_6Ni_6C	Mo	Mo_6Ni_6C
		$Ti_4Fe_2O_{0.4}$	Ti	V_3Zr_3O1-x
		$W_4Ni_2C_{0.67}$	W	V_3Zr_3O1-x
227	32e	Ni_6Nb_6O	Ni	Mo_6Ni6C
		Co_6Mo_6C	Co	Mo_6Ni6C
		Mo_3Mn_3C	Mn	Carbide(eta)-Fe_3W_3C
		Zn_3Ti_3N	Zn	Carbide(eta)-Fe_3W_3C

Space Group	**Wyckoff position**	**Compound**	**Elements in Wyckoff position**	**Structure type**
		TiC	Ti	$LiTiO_2$
228	96g	$K_2Fe_8Al(SO_4)_{12}$ $(H_2O)_{18}$	Fe	Voltaite
		$K_2Mg_5Fe_4(S\ O_4)1_2(H_2O)_{18}$	Fe, Mg	Voltaite
229	48i	$BaCuO_2$	Cu	$BaCuO_2$
		$Ba_{44}Cu_{45}Cl_4O_{87}$	Cu	$BaCuO_2$
		$Ba_{88}Cu_{88}Br_2O_{175}$	Cu	$BaCuO_2$
		$Al_2Ni_6Y_3H_9$	Ni	$Al_2Ni_6Y_3H_9$
		$Ba_{41}Cu_{44}O_{84}Cl_2$	Cu	
		$Sr_{39}Co_{12}N_{31}$	Co, N	
		$Ho_3Ni_6Al_2H_8$	Ni	
229	24g	$Ag_{3.5}SI$	Ag	Ag_3+xSI
229	12e	$Al_2Ni_6Y_3H_9$	Y	$Al_2Ni_6Y_3H_9$
		$Ni_{60}Yb_{11}C_6$	Ni, C	$Ni_{60}Yb_{11}C_6$
		$NiZr_6Cl_{15}$	Zr	$NiZr_6Cl_{15}$
230	48g	$Cs(FeSi_2O_6)$	Fe, Si	pollucite
		$Cs_4(CuSi_5O_{12})$	Cu, Si	pollucite
		$(Mg_{2.55}Ni_{0.45})Al_2(SiO_4)_3$	Mg, Ni	
		$Ca_3Mn_{2.26}O_{2.28}(SiO_4)_{2.43}$	Mn	

Figure I-1. Axion insulator candidates identified from later database and literature searches.

Criteria:
- small bandgap insulator
- heavy elements for SOC
- broken time-reversal symmetry (magnetic ions)
- analogues of non-magnetic topological insulators
- don't become metallic via defects

Candidates (from January 2020 or earlier):
- $EuMn_2Y_2$ (Y=P, As, Sb)
- $Eu_5In_2Sb_6$
- $Eu_3In_2P_4$
- $Eu_{14}AlSb_{11}$
- $Eu_{21}Mn_4Sb_{18}$
- $Eu_{16}Sb_{11}$
- Y_2Ru_2O7

Candidates from initial Topological Materials Database search
(even number of band inversions, need substitution of magnetic ions)
- $Ba_3As_2O_8$
- SrP_2
- $SrGa_2As_2$
- $BaGe_2$
- $BaSi_2$
- Ba_2Ge_4
- Ba_2Si_4
- $Ba_2Bi_2O_6$
- $Ba_3P_6Si_4$
- $BaAs_2Ge_2$
- BaCaPb
- La_2S_5Sn
- BrLuS
- Ba_2Sn
- Ba_3Si_4
- $BaPbO_3$
- Ba_2TeZnO_6
- Sr_3As_4
- SrZnSbF

Biographical sketch

Veronica Jane Stewart was born in Cleveland, Ohio to parents David Stewart and Carmen Sultana on December 27, 1991. Raised in Haddonfield, New Jersey, Veronica graduated from Haddonfield Memorial High School in May 2010. She attended Reed College in Portland, Oregon, where she majored in chemistry. At Reed, she completed undergraduate thesis research on vanadium oxide sol-gels for lithium ion batteries, working under Professor Margret Geselbracht, and served as a supervisor and senior reactor operator at the Reed Research Reactor. After graduating in May 2014, she worked in education for two years before beginning her graduate studies in the Chemistry department at Johns Hopkins University. She joined the research group of Professor Tyrel McQueen, and worked under his guidance and as part of the JHU Institute for Quantum Matter. Her dissertation research focused on the design, synthesis, and characterization of topological materials. Veronica earned her Master of Arts degree in May 2018, and her Doctor of Philosophy degree in August 2021.

Publications:

V.J. Stewart, R. Bhandia, F. Mahmood, P. Armitage, Y. Xu, N. Drichko, Y. Tian, M. Chen, and T. M. McQueen. "Hidden order in the breathing pyrochlore $Nb_4Se_4I_4$." In preparation.

V.J. Stewart, J.R. Chamorro, and T.M. McQueen. "Integer vs. half-integer spin on an approximate honeycomb lattice." arXiv:2103.16684 (2021).

M. Sinha, H.K. Vivanco, C. Wan, M.A. Siegler, V.J. Stewart, L.A. Pressley, T.

Berry, Z. Wang, I. Johnson, M. Chen, T.T. Tran, W.A. Phelan, and T.M. McQueen. "Columnar Disorder and Low-temperature Properties of the Intermetallic Kagome $MgCo_6Ge_6$." arXiv:2102.03522 (2021).

Simran S. Saund, Samantha L. Goldschmid, Karina Ng, Veronica Stewart, Maxime A. Siegler and V. Sara Thoi. "Exploring ligand non-innocence of coordinatively-versatile diamidodipyrrinato cobalt complexes." Chemical Communications, 55, 1825-1828 (2019).